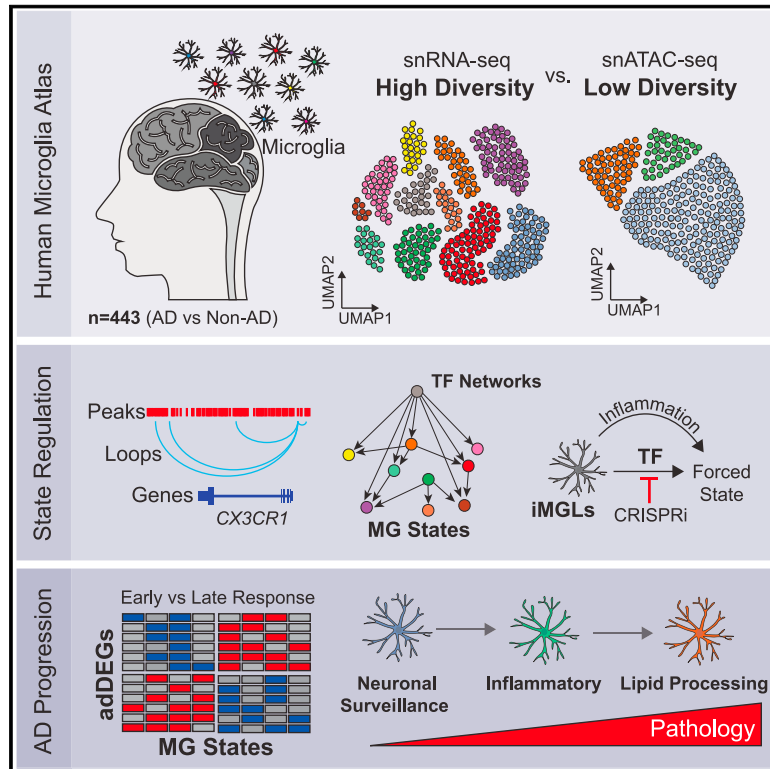


# Human microglial state dynamics in Alzheimer's disease progression

## Graphical abstract



## Highlights

- Single-nucleus transcriptomes and epigenomes of human microglia
- Microglia state-specific and disease-stage-specific profile in Alzheimer's disease
- Chromatin accessibility poorly captured microglia transcriptional state diversity
- Transcription factor networks regulate microglial states and their transitions

## Authors

Na Sun, Matheus B. Victor, Yongjin P. Park, ..., David A. Bennett, Li-Huei Tsai, Manolis Kellis

## Correspondence

lhtsai@mit.edu (L.-H.T.), manoli@mit.edu (M.K.)

## In brief

Microglia states showing Alzheimer's disease (AD)-risk-gene expression and AD-progression-associated expression differences were identified from the microglial transcriptome and epigenomes from the 443 human subjects spanning brain regions and diverse clinical and pathological states. Computational framework and functional studies using iPSC-derived microglia defined the diversity of microglial states across disease, the disease-stage changes of gene expression, and the regulatory network that governs microglial state transitions during the progression of AD.



Article

# Human microglial state dynamics in Alzheimer's disease progression

Na Sun,<sup>1,2,9</sup> Matheus B. Victor,<sup>3,4,9</sup> Yongjin P. Park,<sup>1,2,5,6</sup> Xushen Xiong,<sup>1,2</sup> Aine Ni Scannail,<sup>3,4</sup> Noelle Leary,<sup>3,4</sup> Shaniah Prosper,<sup>3,4</sup> Soujanya Viswanathan,<sup>3,4</sup> Xochitl Luna,<sup>3,4</sup> Carles A. Boix,<sup>1,2</sup> Benjamin T. James,<sup>1,2</sup> Yosuke Tanigawa,<sup>1,2</sup> Kyriaki Galani,<sup>1,2</sup> Hansruedi Mathys,<sup>3,4,7</sup> Xueqiao Jiang,<sup>3,4</sup> Ayesha P. Ng,<sup>3,4</sup> David A. Bennett,<sup>8</sup> Li-Huei Tsai,<sup>2,3,4,\*</sup> and Manolis Kellis<sup>1,2,10,\*</sup>

<sup>1</sup>MIT Computer Science and Artificial Intelligence Laboratory, Cambridge, MA, USA

<sup>2</sup>Broad Institute of MIT and Harvard, Cambridge, MA, USA

<sup>3</sup>Picower Institute for Learning and Memory, Massachusetts Institute of Technology, Cambridge, MA, USA

<sup>4</sup>Department of Brain and Cognitive Sciences, Massachusetts Institute of Technology, Cambridge, MA, USA

<sup>5</sup>Department of Pathology and Laboratory Medicine, Department of Statistics, University of British Columbia, Vancouver, BC, Canada

<sup>6</sup>Department of Molecular Oncology, BC Cancer, Vancouver, BC, Canada

<sup>7</sup>Department of Neurobiology, University of Pittsburgh School of Medicine, Pittsburgh, PA 15261, USA

<sup>8</sup>Rush Alzheimer's Disease Center, Rush University Medical Center, Chicago, IL, USA

<sup>9</sup>These authors contributed equally

<sup>10</sup>Lead contact

\*Correspondence: [lhtsai@mit.edu](mailto:lhtsai@mit.edu) (L.-H.T.), [manoli@mit.edu](mailto:manoli@mit.edu) (M.K.)

<https://doi.org/10.1016/j.cell.2023.08.037>

## SUMMARY

Altered microglial states affect neuroinflammation, neurodegeneration, and disease but remain poorly understood. Here, we report 194,000 single-nucleus microglial transcriptomes and epigenomes across 443 human subjects and diverse Alzheimer's disease (AD) pathological phenotypes. We annotate 12 microglial transcriptional states, including AD-dysregulated homeostatic, inflammatory, and lipid-processing states. We identify 1,542 AD-differentially-expressed genes, including both microglia-state-specific and disease-stage-specific alterations. By integrating epigenomic, transcriptomic, and motif information, we infer upstream regulators of microglial cell states, gene-regulatory networks, enhancer-gene links, and transcription-factor-driven microglial state transitions. We demonstrate that ectopic expression of our predicted homeostatic-state activators induces homeostatic features in human iPSC-derived microglia-like cells, while inhibiting activators of inflammation can block inflammatory progression. Lastly, we pinpoint the expression of AD-risk genes in microglial states and differential expression of AD-risk genes and their regulators during AD progression. Overall, we provide insights underlying microglial states, including state-specific and AD-stage-specific microglial alterations at unprecedented resolution.

## INTRODUCTION

Microglia accomplish their diverse roles in the brain by adopting a variety of phenotypic states that are thought to regulate their functional repertoire.<sup>1</sup> Several studies have sought to characterize the diversity of microglial states across development, aging, and mouse models of Alzheimer's disease (AD).<sup>2–7</sup> However, findings from mouse models of AD have been difficult to link to humans, as disease-associated microglia (DAM) states can differ substantially between mouse models and enriched microglial signatures in brains of AD patients.<sup>8</sup> Single-cell approaches to profile human microglia isolated from postmortem patient brains have been employed to elucidate cellular states associated with AD.<sup>9–13</sup> However, due to the relatively low abundance of microglia in the brain

and the shallow depth of reads afforded by single-cell sequencing, the contributions of microglia and its cellular states to AD is still not fully understood.

Here, we analyzed 152,459 microglial transcriptomes across 443 individuals, identifying 12 transcriptional states and their relevance to AD. By integrating gene signatures with snATAC-seq, we unveiled key regulatory networks poised to regulate distinct microglial states. Using stem-cell-derived microglia-like cells, we tested transcription factors' (TFs) ability to regulate microglial states. We determined AD-stage-specific expression changes, linked AD-risk genes with microglial states, and outlined potential regulatory pathways in AD progression. Our data provide the resolution to define the cellular state and disease-stage-specific contributions of microglia to AD.



## RESULTS

## Characterization of microglia transcriptional states

To characterize microglia states, we analyzed the transcriptome of 152,459 single microglia nuclei from aged postmortem brain samples of 217 individuals with AD (138 early and 79 late) and 226 control individuals (Table S1, page 1) across 6 brain regions, consisting of prefrontal cortex (PFC), hippocampus, mid-temporal cortex, angular gyrus, entorhinal cortex, and thalamus, from the Religious Orders Study and Rush Memory and Aging Project (ROSMAP) study.<sup>14</sup> We first collected 174,420 immune cells by *in silico* sorting from brain single-nucleus RNA-seq (snRNA-seq)<sup>15</sup> datasets using known marker genes (STAR Methods),<sup>11,16,17</sup> which formed into 16 clusters, including 12 clusters of microglia (clusters 0–8 and 10–12, marked by *CSF1R*, *CD74*, and *C3*), one cluster of brain-associated macrophages (BAMs; cluster 9, marked by *MRC1*, *CD163*, and *LYVE1*), one cluster of T cells (cluster 13, marked by *CD3E* and *CD3G*), and two clusters of potential doublets with other brain cell types (clusters 14 and 15) (Figures S1A and S1B). We kept the 12 microglia clusters for in-depth analysis.

We defined these 12 clusters as distinct microglial states based on their molecular signatures and functions (Figures 1A, 1B, and S1C–S1G; Table S1, pages 2–3). We annotated homeostatic microglia (MG0) with high expression of well-known homeostatic markers *P2RY12* and *CX3CR1*, and neuronal surveillance microglia (MG1) with high expression of neurotransmitter receptors (Figure S1F).<sup>18</sup> We found that MG3 showed strongest enrichment to ribosome biogenesis (Figure S1G). We annotated MG4 as a lipid-processing state based on the enrichment of lipid homeostasis and regulation of cholesterol efflux. We annotated MG5 as a phagocytic state due to the significant enrichment of phagocytosis and receptor-mediated endocytosis terms. Of note, MG5 enrichment to phagocytic genes was relatively lower compared to the BAMs (Figure S1C). We annotated MG6 as a stress-related state based on the significant enrichment in response to unfolded protein, MG7 as a glycolytic state because of the enrichment in glycolytic process, MG11 as an antiviral state based on the strong enrichment of viral process and defense response to virus, and MG12 as a cycling state due to the enrichment in DNA replication. We also found three inflammatory states (MG2, MG8, and MG10) showing high expression of several cytokines and cytokine receptors (*CCL3*, *IL1B*, *IL15*, *IL4R*, *IL17R*, and *IL10RA*) and strong functional enrichment in immune responses, including cytokine-mediated signaling pathway and regulation of inflammatory response. We further annotated MG2 as inflammatory I (*CPEB4/TMEM163/IL4R*), MG8 as inflammatory II (*LRRK2/SPON1/FOXP1*), and MG10 as inflammatory III (*IL1B/CCL3/RELB*). We next compared these 12 microglial states with a previously published dataset (Olah et al.)<sup>12</sup> and found that MG3 (ribosome biogenesis), MG6 (stress-related), MG10 (inflammatory III), MG11 (antiviral), and MG12 (cycling) states show strong and significant alignment across studies, while MG0 (homeostatic) state shows weak but significant alignment (Figures S1H and S1I; STAR Methods). In addition, comparison with mouse microglial transcriptional states yielded several well-aligned and conserved states across species<sup>4</sup> (Figure S1J). We found that all 12 microglial states were robustly detected from each of six brain regions profiled (Figures S2A

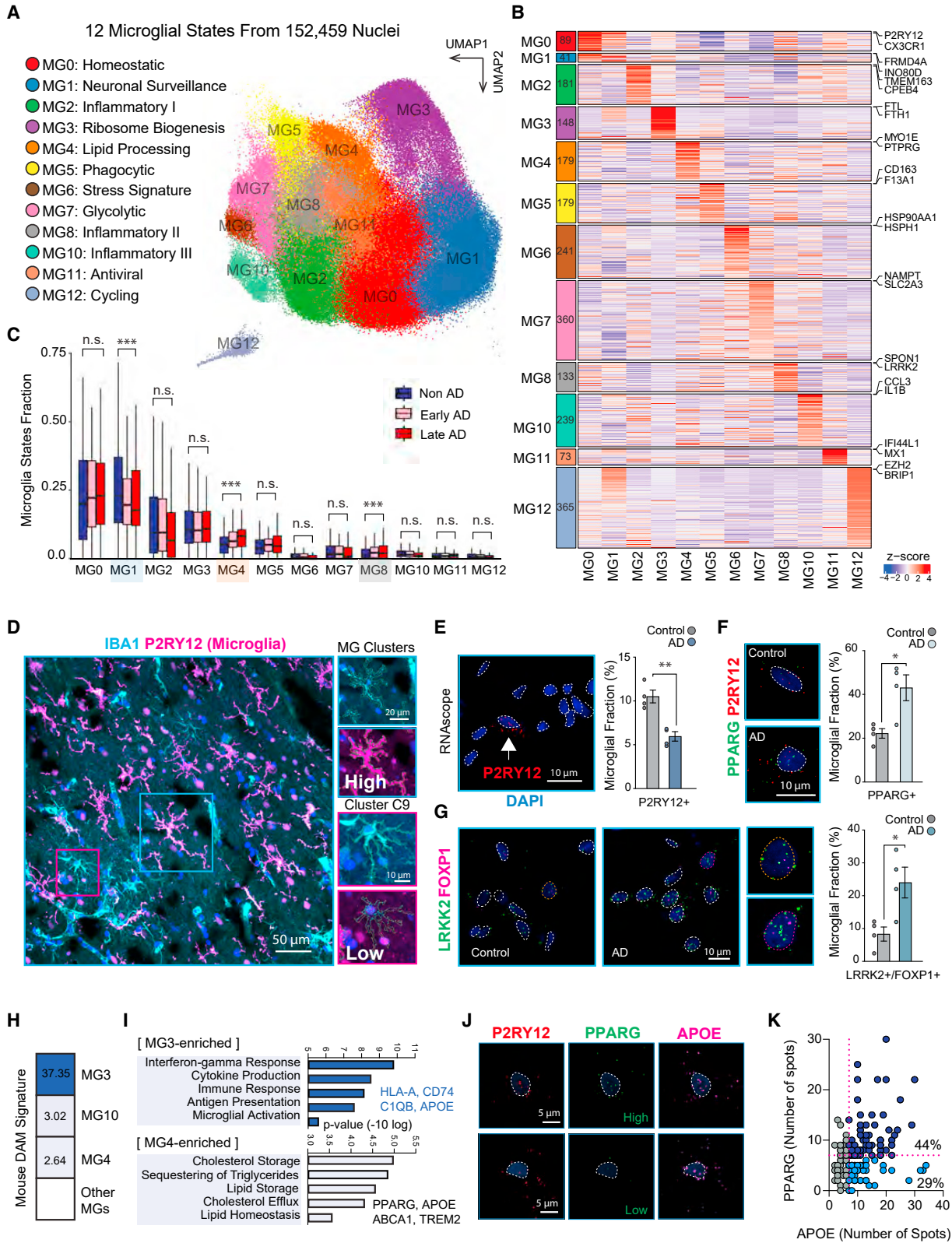
and S2B). However, the microglial states showed significant proportional differences across these regions (Figures S2B and S2C).

To evaluate whether the relative proportions of these microglia states change in AD, we tested the statistical significance of cell fractional differences between control, early, and late AD individuals in the prefrontal cortex, which covered 423 individuals. We found that lipid-processing MG4 and inflammatory MG8 showed significantly increased fractions in AD, while neuronal surveillance MG1 showed a significantly decreased fraction in AD (Figures 1C and S2D; STAR Methods). We also performed correlation analysis between the microglial state proportions and multiple pathological variables in PFC to explore the association of those states with specific AD-relevant pathology and confounding factors (Figure S2E; STAR Methods). We found that lipid-processing MG4 microglia showed the most significantly positive correlation with tangles, amyloid, Braak score, and cognitive decline. We found that inflammatory MG8 was more positively correlated with plaques, whereas phagocytic MG5 microglia were more positively correlated with tangles. We also observed that none of the microglial states were dominated by individuals and other covariates including batch, age, sex, or postmortem interval (PMI) (Figures S2F and S2K). However, we found that the proportions of several microglial states were significantly different with age (MG5 and MG4), PMI (MG1 and MG4), and sex (MG3) (Figure S2K), suggesting the importance of controlling these covariates when we evaluate the proportional changes between phenotypic groups.

We next sought to experimentally validate the enrichment of key transcriptional states in the AD human brain through immunohistochemistry and RNAscope *in situ* hybridization. Using the pan-macrophage marker IBA1 as a counterstain to label brain-resident macrophages, we performed immunohistochemistry for P2RY12 across 8 AD subjects, which revealed high levels of P2RY12 immunoreactivity (Figures 1D and S5). We only observed a small population of IBA1-positive, P2RY12-negative cells within the brain parenchyma, perhaps reflecting CNS-infiltrating macrophages (Figure 1D). We reasoned that P2RY12 was therefore a compelling microglia-specific marker for *in situ* hybridization analysis. We performed RNAscope for P2RY12 in 4 AD and 4 non-AD individuals and found AD subjects had relatively lower fractions of P2RY12-expressing nuclei (Figure 1E).

Since MG4 state showed the relatively higher expression levels of *PPARG* in snRNA-seq data, we probed for *PPARG* through RNAscope in AD and non-AD brain tissues. We found a significant increase in the fraction of *PPARG*<sup>+</sup>*P2RY12*<sup>+</sup> cells in AD subjects relative to controls (Figure 1F). Additionally, we also observed enrichment of *FOXP1*<sup>+</sup>*LRRK2*<sup>+</sup> microglia in these subjects, an expression pattern that marks MG8 inflammatory states (Figure 1G). Collectively, these findings through *in situ* hybridization corroborate our snRNA cell fraction analysis and points to lipid-processing and inflammatory states as disease-associated microglial states.

We performed enrichment analysis to capture the expression of DAM genes across our dataset<sup>5</sup> (Figures S1D and S1E). Interestingly, we observed the strongest enrichment of DAM signature genes in MG3, a microglial state that is proportionally unchanged in AD (Figure 1H). Of note, MG3 DAM enrichment is mostly driven by overlap in ribosome protein genes. In addition,



(legend on next page)

we observed significant but relatively lower enrichments of mouse DAM signatures across multiple MG states, including lipid-processing MG4 and inflammatory MG10. Due to the higher prevalence of MG4 microglial fractions in brains with AD, we compared the transcriptional programs enriched for MG3 and MG4. Gene ontology (GO) analysis for genes enriched in ribosome biogenesis MG3 state over all other microglial states revealed a suite of inflammatory genes enriched for cytokine production and microglial activation pathways (e.g., *HLA-A*, *CD74*, *C1QB*, and *APOE*). For the lipid-processing MG4 state, this analysis uncovered an enrichment of cholesterol and lipid homeostasis genes (e.g., *PPARG*, *APOE*, *ABCA1*, and *TREM2*) (Figure 1I). High expression of *APOE* by microglia has been deemed a state marker for both DAM and a broader but similar activated microglia mouse signature known as microglia neurodegenerative phenotype (MGnD).<sup>19</sup> To determine if higher levels of *APOE* expression could be distinguished into discrete populations, we performed RNAscope with probes targeting *APOE*, *PPARG*, and the microglial marker *P2RY12* (Figure 1J). We reasoned that levels of *PPARG* expression could segment high *APOE* expressing microglia into distinct populations that differentiated ribosome biogenesis MG3 from lipid-processing MG4. We discovered that while the vast majority of *PPARG*<sup>+</sup> microglia expressed high levels of *APOE* (88% of all *PPARG*<sup>+</sup> nuclei were co-detected with greater than 7 *APOE* dots), a significant fraction of *APOE*<sup>+</sup> microglia lacked significant levels of *PPARG* detection (27.6% of all *APOE*<sup>+</sup> nuclei were co-detected with less than 7 *PPARG* dots) (Figure 1K). Altogether, this indicates that DAM-like signatures in the human AD brain do not encompass a single state, but rather can be distinguished across many substates.

### Distinct inflammatory states in the aged human brain

Cell proportional analysis also revealed the enrichment of inflammatory MG8 state in AD subjects (Figure 1C). The presence of distinct inflammatory states is intriguing as it could reflect alternative transcriptional programs that are activated by distinct pro-inflammatory stimuli (Figure 2A). Nevertheless, functional categorization of pathways significantly enriched by inflammatory clusters pointed to a pattern of decreasing inflammatory status

(MG10 > MG2 > MG8), suggesting that these clusters may instead represent states during the progression of inflammation (Figure 2B).

To determine if these clusters represent distinct populations within the human brain, we immunostained fixed prefrontal cortex brain sections with the macrophage marker IBA1 and used 3D rendering by Imaris to build cellular traces that spatially delineated microglia cell bodies within these sections (Figures 2C and S3). Next, we multiplexed IBA1 staining with additional antibodies against top markers for each cluster (namely, IL1B for MG10, LRRK2 for MG8, and CPEB4 for MG2) (Figure S4A). While IBA1 was highly expressed in all cells, we found instances when the highest expression for each cluster marker was largely in non-overlapping microglia (Figures S4B and S4C).

To investigate how co-expression of multiple inflammatory state markers can distinguish discrete inflammatory programs in the human brain, we turned to a multiplexing platform through RNAscope technology, which allows for many probes to be co-detected through iterative rounds of imaging (STAR Methods). We simultaneously profiled the expression of 9 targets in 4 AD subjects to dissect the relationship of MG8, a weakly inflammatory state that is enriched in AD to other inflammatory states. We further resected prefrontal cortices into a 2mm disc with a biopsy punch so that we could image the entire sample and capture defined tissue borders to aid registration (Figure 2D). Using probes against *P2RY12*, *CX3CR1*, and *IBA1*, we assigned microglia nuclei identity and subsequently assessed the co-detected levels of MG8 markers *LRRK2* and *FOXP1*, MG2 markers *CPEB4* and *TMEM163*, and MG10 markers *CCL3* and *RELB* (Figure 2E). For cells that expressed more than one inflammatory marker, we found that inflammatory programs were largely overlapping, with MG2 signatures (*CPEB4* and *TMEM163*) bleeding into MG8 and MG10 states in 23% of the inflammatory microglia (Figure 2F). The expression of MG8 and MG10 markers were correlated as demonstrated by the dendrogram depicted from the hierarchical clustering from quantification across all cells (Figures 2F and S4D). In fact, we were able to detect expression of MG8 and MG10 markers in a small fraction of non-overlapping microglial populations, while non-overlapping MG2 states were rarely detected (Figures 2F and 2G). While it is challenging to extrapolate from these results given the semi-quantitative nature

### Figure 1. Microglial transcriptional states in aged human brains

(A) UMAP of 152,459 microglia nuclei with annotated microglial states in snRNA-seq data.

(B) Heatmap to show 2,228 highly expressed genes in 12 microglial states. The left block with matched colors shows the number of genes in each state. The right shows the representative genes. Z scores across microglia states are used for the plot.

(C) Cell fraction distribution in AD pathological groups. Propeller analysis was used to determine the statistical significance highlighted with \*\*\*. The box starts in the first quartile (25%) and ends in the third (75%). The line inside the box represents the median.

(D) Immunostaining of human postmortem brain tissue for the pan-macrophage marker IBA1 in cyan and the microglial homeostatic marker *P2RY12* in magenta.

(E) RNAscope *in situ* hybridization of postmortem prefrontal cortex tissue probed for the microglial marker *P2RY12* (red) and counterstained with the nuclei marker DAPI. Error bar represents the SEM.

(F) Microglial fraction of *P2RY12*<sup>+</sup> with co-detected MG4 marker, *PPARG*. Error bar represents the SEM.

(G) Microglial fraction of *P2RY12*<sup>+</sup> with co-detected MG2 markers, *LRRK2* and *FOXP1*. Error bar represents the SEM.

(E–G) Quantification shown from 8 subjects, averages from microglial fractions of total DAPI nuclei shown for 4 AD and 4 controls. Student's t test, \*\*p value < 0.01. n = 91 to 149 cells per group.

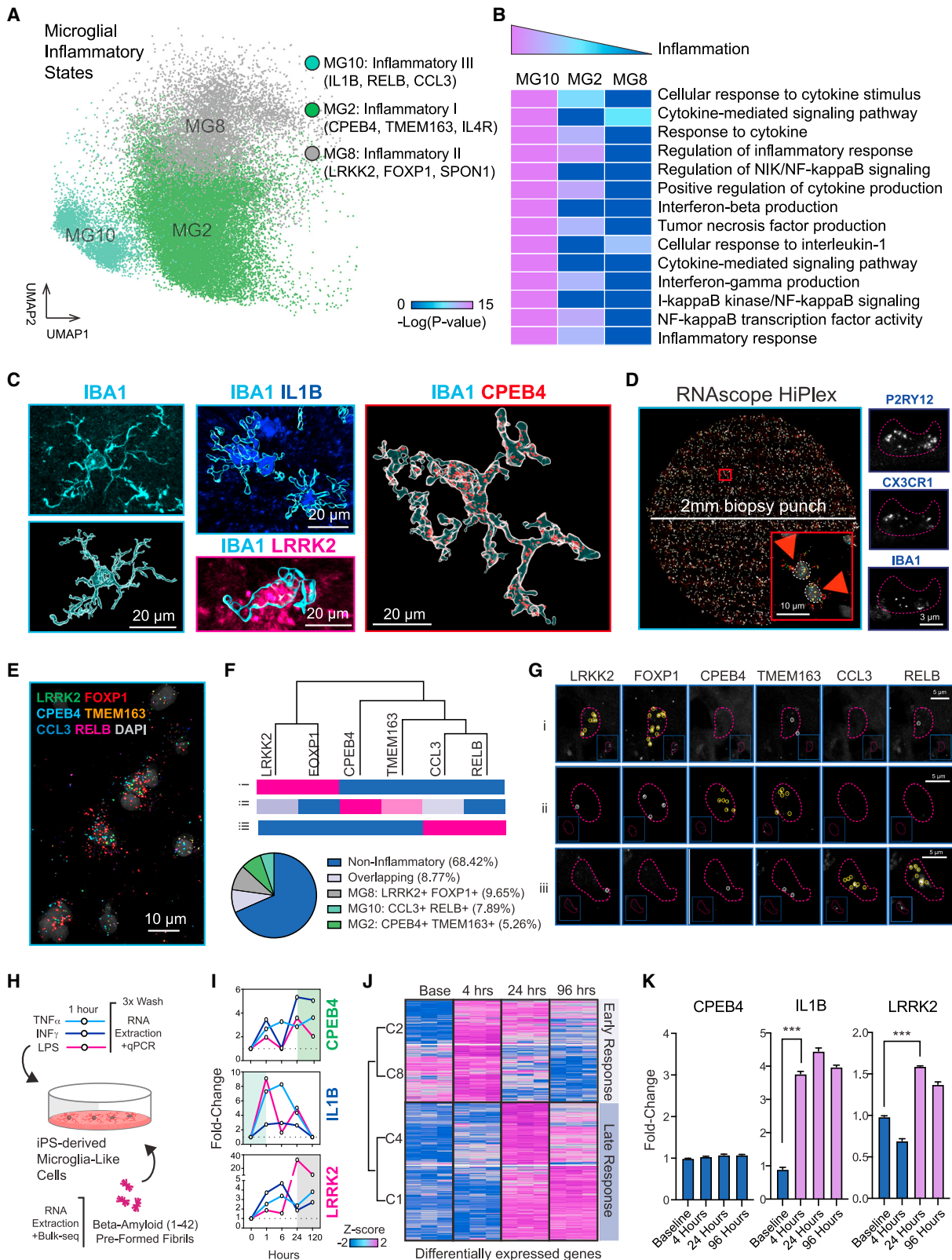
(H) Enrichment analysis of mouse DAM signature across human microglial states.

(I) Enriched GO terms of highly expressed genes in MG3 vs. all states (upper panel), and MG4 vs. all states (lower panel).

(J) Co-detection analysis of *PPARG* and *APOE* in *P2RY12*<sup>+</sup> microglia from 4 AD subjects with RNAscope.

(K) *APOE* and *PPARG* detection greater than 7 dots reveals discrete *APOE*<sup>+</sup> populations. n = 152 *P2RY12*<sup>+</sup> cells.

See also Figures S1–S3 and Table S1, pages 1–4.



(legend on next page)

of RNAscope technology, the overlapping programs may be indicative of dynamic transitions in a continuum of inflammation.

We next investigated the transcriptional kinetics of these markers in relation to inflammation. To do so, we derived microglia-like cells (iMGLs) from induced pluripotent stem cells (iPSCs) following established protocols<sup>20</sup> and performed a pulse-and-chase experiment by briefly exposing these cells to distinct pro-inflammatory stimuli, such as tissue necrosis factor- $\alpha$  (TNF- $\alpha$ ), interferon- $\gamma$  (IFN- $\gamma$ ), bacterial lipopolysaccharide (LPS), or pre-formed amyloid beta (1–42) fibrils. We then assessed the expression of inflammatory MG2, MG8, and MG10 markers over the course of 96–120 h (Figure 2H; Table S1, page 5). We profiled the expression of *IL1B* and 6 additional markers of MG10 (including *CCL3* and *RELB*) and observed that presentation of pro-inflammatory stimuli evoked a largely acute response that was completely resolved by 120 h (Figures S4E and S4F). We found that markers for MG2 (*CPEB4*, *LIMK2*, and *FAM129A*) and MG8 (*LRRK2*, *GPR155*, and *CYP27A1*) showed sustained activation that was not resolved by the same time frame (Figures 2G, S4E, S4G, and S4H). To understand if a similar temporal response could be evoked with a more physiological pro-inflammatory stimulant, we treated iMGLs with pre-formed amyloid beta fibrils and performed a similar pulse-and-chase experiment at 4 h, 24 h, and 96 h post amyloid seeding (Figure 2J). We found a rich transcriptional response that was enriched for inflammatory pathways and clustered by early (upon 4 h) and late response (upon 24 h) (Table S1, page 6). Interestingly, amyloid beta fibrils did not evoke *CPEB4* transcription activation (MG2 state marker) but recapitulated the early onset of *IL1B* and the delayed activation of *LRRK2* (Figure 2K). To understand if the temporal kinetics of inflammatory programs across these states are captured globally during disease progression, we analyzed the contribution of inflammatory states to transcriptional changes for early and late AD subjects. Indeed, MG10 shows greater transcriptional changes in early disease stages while MG2 and MG8 are more robustly changed in late stages (Figures S4E–S4H). Collectively, this data suggests that our microglia profiling might be capturing cells along a spectrum of inflammatory responses with amyloid-dependent and -independent responses and not likely bonafide discrete populations.

### Prediction of upstream transcription factors of microglial states

To investigate the upstream regulators that drive distinct microglial states, we leveraged the chromatin accessibility data measured by single-nucleus ATAC-seq (snATAC-seq) using human postmortem brain tissues from a subset of individuals in the same cohort (100 individuals; Table S1, page 7).<sup>21</sup> We obtained 41,832 nuclei of microglia with good quality and captured three epigenomic states, including one homeostatic state (HOM) and two activated states (ACT1 and ACT2; Figures 3A and S5A–S5C; STAR Methods). We found that *P2RY12*, the homeostatic marker, showed relatively low accessible signals in activated states although ubiquitous accessibility in all microglia (Figures S5B and S5C). We also observed that *CCL3* showed significantly higher accessibility in ACT1, suggesting that the microglia in this epigenomic state could be related to immune response. We also found that *SPP1* showed high accessibility in ACT2, consistent with its functions to mediate cell activation and cytokine production.<sup>22</sup>

We noticed that microglia show higher heterogeneity at the transcriptional level than the chromatin accessibility level (Figures 1A and 3A). To evaluate whether this stems from technical bias or an unbalanced number of microglia in these two modalities, we analyzed 4,244 microglia nuclei using 10x multiome from human postmortem brains of 19 individuals. We identified nine transcriptomic and two epigenomic clusters using individual modality (Figure S8D), validating our previous observation. We also found that the nine transcriptomic clusters can recapitulate the microglial states we identified in the larger cohort (Figure S5E).

We next called 179,534 accessible peaks and identified 16,800 epigenomic-state-specific peaks (Figures S5F and S5G; STAR Methods). We annotated these peaks by the number of associated genes and their distance to TSS and predicted their functions (Figures S5H and S5I; STAR Methods). We found that homeostatic peaks were enriched near genes acting in regulation of calcineurin-NFAT signaling and lipoprotein particle clearance. Peaks in the activated states were significantly enriched in genes related to cellular response to interleukin, regulations of establishment and maintenance of the blood-brain barrier (BBB), and cytotoxic T cell differentiation, consistent with previous findings that suggested that activated microglia impair

### Figure 2. Microglial inflammatory states capture an inflammatory continuum

(A) UMAP of three inflammatory states of microglia.

(B) Enrichment of inflammation-related biological processes in three inflammatory states, represented by the  $-\log_{10}$  (p value) in heatmap.

(C) Multiplexed immunostaining of top inflammatory state markers. IBA1 labeled for CNS resident macrophages and derived 3D rendering of cell morphologies, ILB1 for MG10, *LRRK2* for MG8, and *CPEB4* for MG2 microglia.

(D) Maximum projection of tile scan from a 2 mm biopsy punch of prefrontal cortex tissue after alignment of 4 iterative rounds of RNAscope with inflammatory-state and microglial-specific probes. Inset shows 2 microglia nuclei marked by red arrows and representative image of detection of microglial-specific probes (right panel).

(E) Higher magnification of composite image with inflammatory-state probe detection.

(F) Dendrogram and representative cells for inflammatory state probe detection of heatmap in Figure S4D (upper panel). Cell fraction analysis of 291 microglia for 4 AD subjects. Number of RNAscope dots Z scored across all cells (lower panel).

(G) Images from representative microglia nuclei with signatures of discrete inflammatory states.

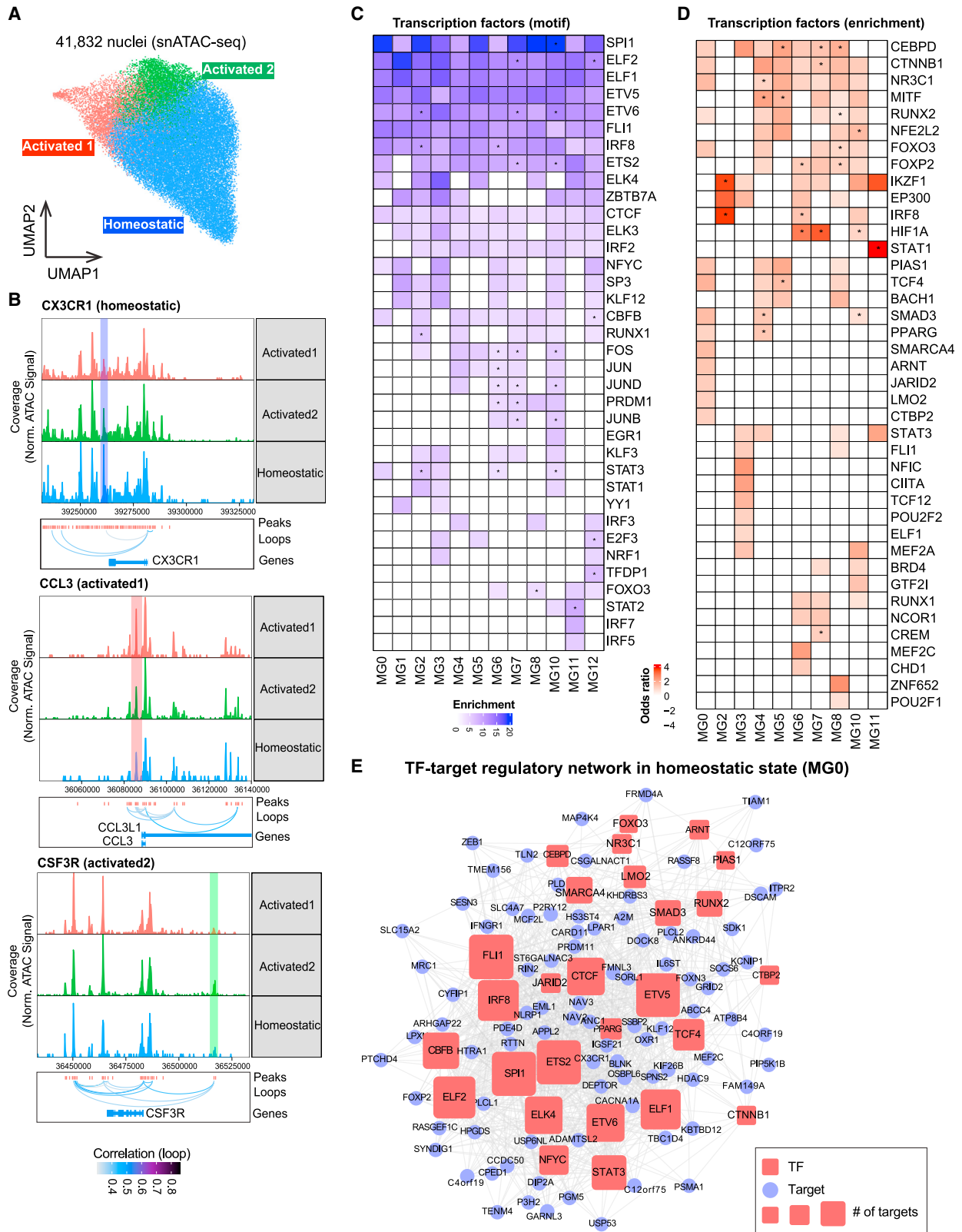
(H–J) Transcriptional kinetics of inflammatory state markers in iPSC-derived microglia-like cells (iMGLs).

(I) Treatment with TNF $\alpha$  (40 ng/mL), IFN $\gamma$  (30 ng/mL), or LPS (10 ng/mL) for 1 h and profiled by qPCR.

(J) Treatment with pre-formed amyloid beta (1–42) fibrils and profiled by RNA-seq; heatmap of early and late response up regulated genes.

(K) Levels of *CPEB4*, *IL1B*, and *LRRK2* expression in response to amyloid treatment. n = 3 biological replicates per group. ANOVA with post-hoc Tukey test. \*\*\*p value < 0.001. Error bar represents the SEM.

See also Figures S3 and S4 and Table S1, pages 4–6.



(legend on next page)



BBB function by producing inflammatory proteins to induce hyperpermeability of BBB in brain diseases.<sup>23</sup>

To investigate the regulatory machinery of these microglial states, we predicted TFs through motif enrichment in the peaks of these epigenetically defined states (Figure S5J). We found that although several TFs (including SPI1, IRF8, and STAT1) showed ubiquitous enrichment in all three states, the enrichment for these factors were considerably stronger in activated states, perhaps reflecting the dynamic balance of microglial TFs that act in both cell fate maintenance and the activation of inflammatory programs. By contrast, several TFs (including ARID5B and ID2) showed specific enrichment in the activated states, suggesting their regulatory potential in certain conditions. We also observed that the peaks from the two activated states were associated with very similar functions and shared many TFs even though the peaks themselves were distinct (Figures S5G–S5J).

To further refine these gene-regulatory interactions, we linked distal peaks to promoters using the co-accessibility patterns of promoters and distal accessible peaks (STAR Methods). We found 122,658 peak-to-promoter links, implicating 17,109 genes and 46,498 peaks (Table S1, page 8). For example, we found that a peak with strong signal near *CX3CR1* in the homeostatic state linked with its promoter, and *CCL3* and *CSF3R* each had peak-to-gene links in a distinct activated state (Figure 3B).

With this co-accessibility, we identified 36 TFs that may modulate microglial states through motif analysis on the distal peaks of microglial state markers (Figure 3C, STAR Methods). To complement this method, we inferred 40 TFs whose known targets were enriched in microglial state makers<sup>24</sup> (Figure 3D, STAR Methods). Notably, 7 TFs were identified in both methods, including FOXO3 (MG8), IRF8 (MG2, MG6, and MG10), STAT3 (MG3), and RUNX1 (MG7). We also observed that 15 TFs (including SPI1 and CTCF) showed consistent enrichment across all microglial states, suggesting their functions in the maintenance of microglial cell identity and genomic architecture.<sup>25,26</sup> Conversely, three TFs exhibited microglial-state-specific enrichment: TFDP1 in MG12 (cycling), aligned with its cell cycle regulation function,<sup>27</sup> and IRF7 in MG11 (antiviral), reflecting its role in type 1 interferons production for antiviral immunity.<sup>28</sup>

Several TFs, like *FOXO3* in inflammatory MG8, were prominently expressed in microglial states, regulating marker genes (Figures 3C and 3D), aligning with its function in microglial inflammatory activation.<sup>29</sup> Similarly, *HIF1A* was highly expressed and significantly regulated the marker genes in MG7 (glycolytic), MG6 (stress), and MG10 (inflammatory), reflecting its functions in glycolytic metabolism, response to inflammation and stress of microglia.<sup>30–32</sup> We also conducted single-cell TF activity anal-

ysis via DoRothEA,<sup>33</sup> revealing significant motif/gene-enrichment (Figure S5K).

To further investigate the regulatory mechanisms of TFs, we constructed a TF-target regulatory network (Figure 3E, STAR Methods) for HOM MG0. We found that the homeostatic markers were usually regulated by multiple TFs, suggesting that the TFs may be acting cooperatively or that transcriptional regulation may be redundant to maintain the robustness of the system. To test whether the TFs collaboratively control gene expression, we evaluated the significance of the shared targets between every pair of TFs (STAR Methods). We found that 13 TFs (including several ETS TF family members, SPI1 and CTCF) significantly shared their targets within the co-regulatory module (Figure S5L). We also observed that the other 14 TFs showed specificity or formed small modules with few TFs, suggesting that these TFs may control the gene expression of a subset of marker genes with specialized functions.

### Ectopic expression of master regulators of homeostatic state in human microglia-like cells

Microglia maintained *in vitro* adopt increased activated states relative to their *in vivo* counterparts.<sup>34</sup> We postulated that the non-homeostatic nature of iMGLs could be used as a testbed to determine if ectopic expression of master homeostatic TFs is sufficient to drive features of homeostasis in these cells. We began by performing snRNA-seq on iMGLs to determine how *in vitro* iMGL states compared to *in vivo* MG states. In addition, we also treated iMGLs with LPS to understand the extent to which these cells can show inflammatory activation states that mirror inflammatory MG2, MG8, and MG10. From this experiment we were able to capture the transcriptome of 18,914 iMGL nuclei that formed 10 clusters, and that was largely segregated by treatment condition (i.e., baseline versus LPS enriched) (Figures 4A and S6A). Computing correlation scores across iMGL and MG states revealed a high degree of similarity between MG12 (a cycling state) and C9, a cluster with enrichment of cell cycle genes representing proliferating microglia (Figures 4B and S6A). In addition, we also observed similarities between inflammatory clusters: MG2 and MG10 showed strong similarities to LPS-enriched clusters (C0, C8, C3, and C6), while MG8 showed some correspondence to iMGLs at baseline (C1 and C4). As predicted, the microglial homeostatic MG0 state was not represented in iMGLs (Figure 4C). Since purinergic signaling via P2RY12 provides a window into the cellular state of microglia (i.e., P2RY12 expression is repressed by activated microglia), we previously leveraged functional ATP uncaging assays to functionally assess homeostatic microglia states in

### Figure 3. TFs regulate microglial states

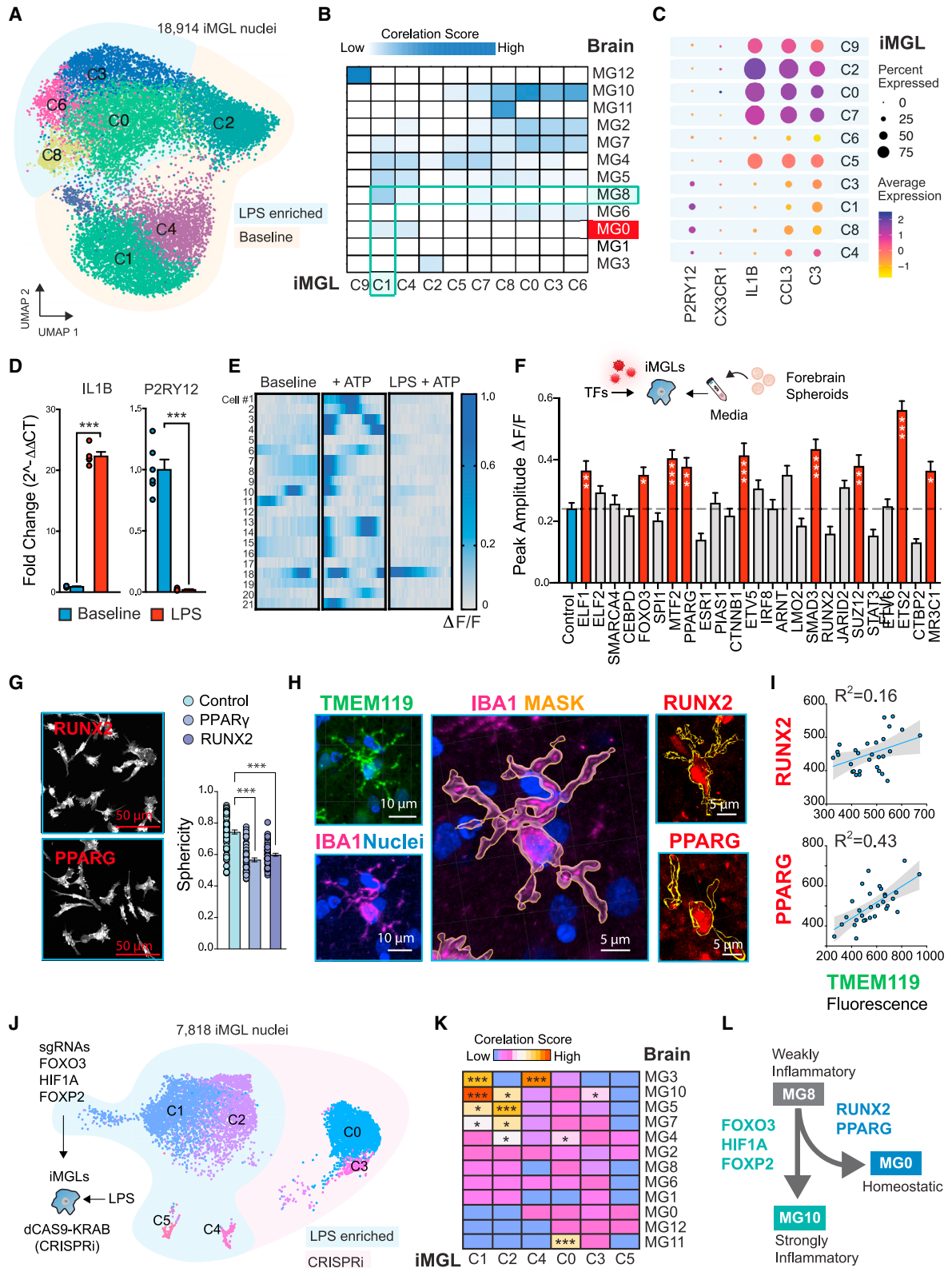
(A) UMAP of 41,832 microglia nuclei with annotated epigenetic states in snATAC-seq data.

(B) Examples of co-accessible links between gene promoters and distal peaks to represent the epigenetic state-specific peaks.

(C) Motif enrichment in the microglial transcriptional state marker genes associated accessible peaks. The  $-\log_{10}$  (p value) represents the enrichment. Stars show the TFs that were highly expressed in the corresponding microglial state.

(D) Heatmap to show the TF enrichment of marker genes in each microglial transcriptional state. Odds ratio represents the enrichment. Stars show the TFs that were highly expressed in the corresponding microglial state.

(E) TF-target regulatory network in MG0 (HOM). The TFs are combined from gene-set-enrichment-based and motif-based analyses shown in (C–D). The pink squared nodes represent the TFs. The light blue circle nodes represent the targets. The size of nodes represents the number of targets. See also Figure S5 and Table S1, pages 7–8.



(legend on next page)

iMGLs bearing sporadic AD-risk variants.<sup>35</sup> We envisioned that we could use this assay as a functional readout of homeostasis. We began by examining the impact of LPS treatment on P2RY12 levels and determined that LPS dramatically reduces its expression (Figure 4D). Purinergic receptors are potent sensors of ATP, and the binding of ATP to P2RY12 robustly induces downstream intracellular calcium release. As such, we conducted calcium imaging in monocultures of iMGLs at baseline and upon exposure of ATP, with or without LPS pre-treatment (Video S1 and Figure S6B). As predicted, we observed that iMGLs pre-treated with LPS showed blunted responses to extracellular ATP compared with baseline conditions (Figure 4F).

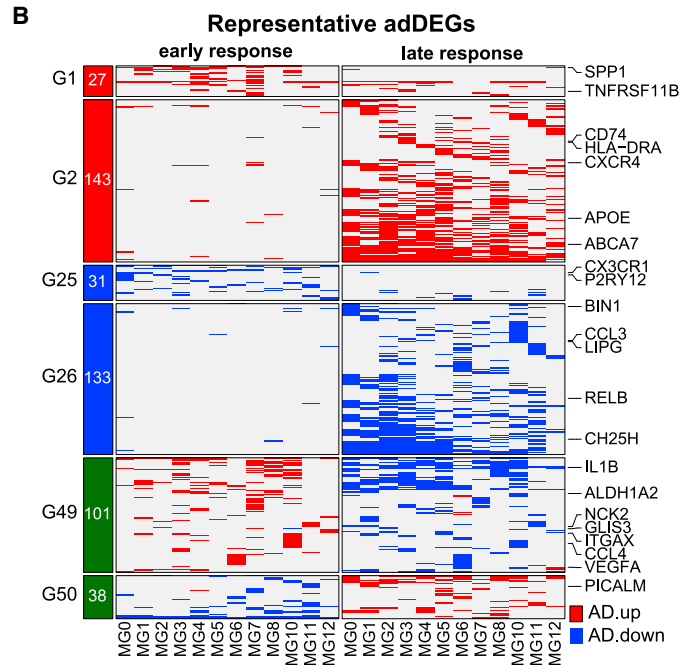
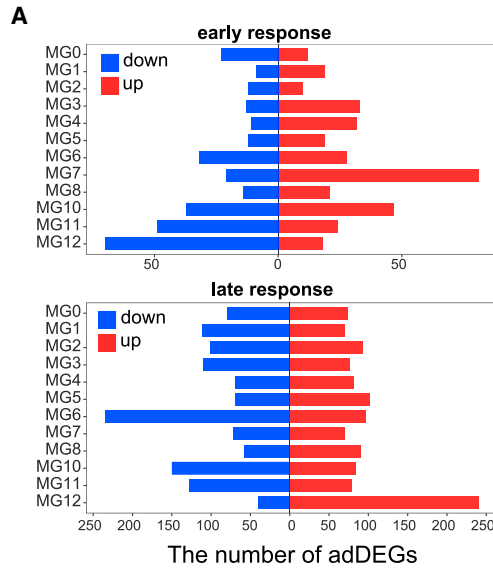
We selected 25 TFs (Figure 3E) to perform an overexpression screen in iMGLs and assay for increased sensibility to extracellular ATP (i.e., greater homeostatic states) (Table S1, page 9). After 8 days of lentiviral transduction, we observed that 58% of cells were successfully infected based on the expression of an mCherry reporter cassette (Figure S6C). We opted to expose the iMGLs to neuronal conditioned media (CM) isolated from forebrain spheroid cultures as we have previously determined that this manipulation induced calcium transients in iMGLs via P2RY12, similarly to ATP uncaging.<sup>35</sup> Controls were infected with lentivirus carrying an empty cassette (Figure S6D). We found that ectopic expression of 9 TFs induced significantly higher rates of calcium transients in iMGLs (Figure 4F). Greater calcium dynamics may not necessarily be indicative of homeostasis. To define if TF overexpression was indeed inducing homeostatic features, we next assessed iMGLs through additional approaches. First, we reasoned that microglia morphology could be informative in assessing its cellular state.<sup>36</sup> In a dish, iPSC-derived microglia do not resemble the morphology of their homeostatic *in vivo* counterparts but yet undergo significant morphological changes upon further activation by adopting a more spherical ameboid-like morphology. Secondly, we could determine the relationship between TF expression and homeostatic markers in the human brain. Through these orthogonal ap-

proaches, we found that overexpression of *RUNX2* and *PPARG* (2 of the hits from our calcium imaging) reduced the adoption of ameboid shape in iMGLs compared to controls (Figures 4G and S6D). In addition, these two TFs were significantly correlated with higher expression of *TMEM119* in IBA1-positive cells within the human brain (Figures 4H and 4I). Co-staining for *TMEM119* and P2RY12 confirmed overlapping microglial populations, as *TMEM119* is a well-established homeostatic marker<sup>37</sup> (Figure S6D). Through this analysis, we also determined that expression of *SMAD3*, *IRF8*, and *ELF1* were not significantly correlated to microglial homeostasis *in vivo* although these were also hits from our calcium imaging screen (Figures 4I and S6F–S6H).

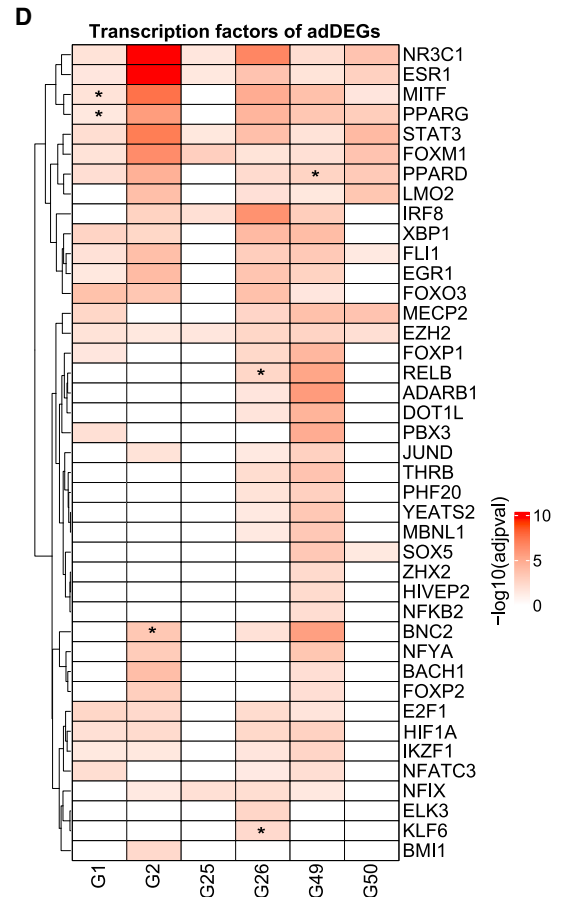
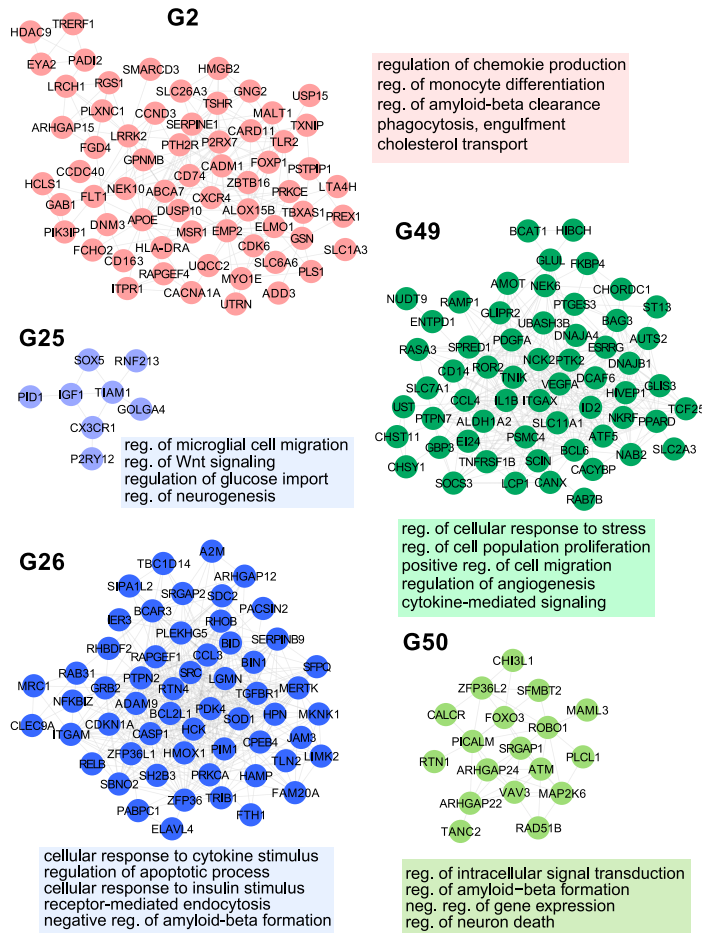
Next, we tested if we could prevent microglial state dynamics by perturbing master regulators of inflammatory state transitions based on our TF activity analysis. We reasoned that LPS could induce state changes that resembled the progression of weak inflammatory MG8 to strong inflammatory MG10 states (i.e., C1 to C0 in iMGLs) (Figure 4A). We began by differentiating iMGLs from a dCAS9-KRAB CRISPRi iPSC line and delivering a total of 3 pairs of *in vitro*-transcribed small guide RNAs (sgRNAs) targeting TFs predicted by our model to drive inflammatory progression from MG8 into MG10 (*FOXO3*, *HIF1A*, and *FOXP2*). 4 h after sgRNA delivery, control (transfected iMGLs, but no sgRNAs) or CRISPRi (transfected iMGLs with MG10 TF cocktail) cells were treated with lipopolysaccharide (LPS) (10 ng/ml) for an additional 12 h and harvested for snRNA-seq (Figure 4J). We found that blocking MG10 TF regulators in the presence of LPS induced new clusters (C0 and C3) and was sufficient to prevent IL1B induction (MG10 state marker) without concomitant gain of homeostatic markers (Figure S6I). Interestingly, this manipulation weakened the execution of the MG10 inflammatory signature, as well as the enrichment of LPS-induced MG3 (ribosome biogenesis), MG5 (phagocytic), and MG7 (glycolytic) signatures, while gaining the enrichment for MG11 (antiviral) signature (Figure 4K). By modeling microglial state dynamics with iMGLs, we functionally assess the TF network activity prediction governing

#### Figure 4. TF-driven regulation of microglial state dynamics in iMGLs

- (A) UMAP of 18,914 iPSC-derived microglia (iMGL) nuclei labeled by clusters. LPS-enriched clusters are shaded in light blue. UMAP with all clusters can be found in Figure S6.
- (B) Enrichment of iMGL marker genes of each cluster in microglial transcriptional states from human postmortem snRNA-seq data.
- (C) Dot plot to show the expression of marker genes in iMGLs clusters. The size represents the percentage of cells with expression. The color represents the scaled average expression level.
- (D) qPCR analysis of IL1B and P2RY12 expression in iMGLs following 12 h of 10 ng/mL of LPS treatment. Student's t-test, \*\*\*p value < 0.001. n = the mean of 6 biological replicates per group. Error bar represents the SEM.
- (E) Raster plots for calcium transients in monocultures of iMGLs at baseline or upon ATP uncaging with 405 nm stimulation. Peak amplitude change in fluorescent intensity ( $\Delta F/F$ ) is displayed from low (gray) to high (dark blue) in 15 s bins over 33 frames. n = 21 cells.
- (F) TF overexpression screen 8 days post viral infection exposed to neuronal spheroid CM to evoke calcium transients. ANOVA with post-hoc Tukey test. \*\*\*p value < 0.001; \*\*p value < 0.01; \*p value < 0.05. n = 80 to 199 cells per group. Red-filled bars represent statistically significant changes in contrast to control while gray-filled bars represent non-significant differences. Error bar represents the SEM.
- (G) Actin-stained iMGLs from *RUNX2* and *PPARG* overexpression and morphology quantification. Image of control sample (iMGLs infected with empty-mCherry lentivirus) is in Figure S6H. ANOVA with post-hoc Tukey test. \*\*\*p value < 0.001. n = 55 to 76 cells per group. Error bar represents the SEM.
- (H) Immunostaining of human brain tissue for homeostatic marker *TMEM119* and pan-macrophage marker IBA1. 3D rendering of IBA1 signal was performed on IMARIS and used to generate a mask delineating cell body, shown in yellow. Immunostaining for homeostatic TFs in IBA1-positive cells across the human brain.
- (I) Regression analysis correlating levels of *PPARG* and *RUNX2* in IBA1-positive cells with the homeostatic marker *TMEM119*. The shaded gray area represents the 95% confidence interval.
- (J–K) UMAP from CRISPRi iMGLs treated with LPS-carrying sgRNAs targeting *FOXO3*, *HIF1A*, and *FOXP2*.
- (K) Enrichment of LPS-treated iMGLs genes for each cluster in microglial transcriptional states from human postmortem snRNA-seq data.
- (L) Diagram of microglial state transition dynamics.
- See also Figures S3 and S6 and Table S1, page 9.



**C** **GO biological processes of adDEGs**



(legend on next page)

microglial state transitionings derived from our postmortem data analysis and provide a roadmap for TF-driven inflammatory state progressions (Figure 4L) (Figure S6J; STAR Methods).

### Transcriptional changes of microglial states in AD

To investigate the transcriptional changes of microglial states in AD progression, we detected AD-related differentially expressed genes (adDEGs) between non-AD and early-AD individuals (refers to DEGs in early response) and early-AD and late-AD individuals (refers to DEGs in late response) in each microglial state using three methods (single-cell-based method: MAST<sup>38</sup> and MAST with random effect (MAST.RE),<sup>39</sup> pseudo-bulk-based method edgeR<sup>40</sup>; STAR Methods). We found that the DEGs identified by three methods were significantly overlapped by pairwise comparison (Figures S7A and S7B), so we defined 1,542 DEGs across 48 comparisons in total, which passed the thresholds in at least two methods. We also evaluated the adDEGs biologically by comparing them with previous work<sup>9</sup> and found 31 of 48 comparisons show significant enrichment with early, late, or end-stage DEGs identified in Gerrits et al.<sup>9</sup> (Figure S7C; STAR Methods).

We next classified 1,542 adDEGs into three major categories and 51 groups based on their effect size and state specificity (Figures 5A and S8; STAR Methods; Table S1, pages 10–11). In particular, we found that 473 DEGs in 6 groups showed AD-stage-specific changes in at least two microglial states (Figure 5B), including two groups with up-regulation in AD progression (G1 and G2), two groups with down regulation in early AD and late AD (G25 and G26), one group with up regulation in early AD and down regulation in late AD (G49), and one group with down regulation in early AD and up regulation in late AD (G50). These stage-specific changes of gene expression in AD progression suggest nonlinear and dynamic functions of microglia during the course of AD progression.

We next performed Gene Ontology enrichment analysis per group and built a gene-gene network by function sharing (Figures 5C and S9A; STAR Methods; Table S1, pages 12). We found that DEGs in G25, including the homeostatic genes *P2RY12* and *CX3CR1*, were down regulated in diverse microglial states in early response to AD but not significantly changed in late response (Figure 5B). These DEGs were significantly enriched in regulations of microglial cell migration, Wnt signaling, and neurogenesis, suggesting that the impairment of the microglial HOM may be an early event in AD progression. We also found that DEGs in G2, including *APOE*, *MSR1*, and *CD74*, were up regulated in late stage but not in early stage and significantly enriched in regulation of chemokine production and amyloid-beta clear-

ance and cholesterol transport, suggesting that regulatory functions related to lipid accumulation of microglia may be a secondary effect in AD progression.

The DEGs in G26 (including AD-risk gene *BIN1* and proinflammatory cytokine *CCL3*), were widely down regulated in multiple states of late stage of AD progression and significantly enriched in cellular response to cytokine and insulin stimulus, receptor-mediated endocytosis, and regulation of amyloid-beta formation. We also found that DEGs in G49, including *IL1B*, *CCL4*, and *VEGFA*, were up regulated in early AD and down regulated in late AD and significantly enriched in regulations of cell proliferation, migration and angiogenesis, and cytokine-mediated signaling pathway, consistent with the recent findings on the effects of microglial cytokines in neurodegenerative disease.<sup>41,42</sup> Additionally, the DEGs in G50, including AD-risk genes *PICALM*, were down regulated in early stage but up regulated in late stage and significantly enriched in regulations of intracellular signal transduction and amyloid-beta formation and neuron death.

We next inferred the upstream regulators of these DEGs to investigate the transcriptional regulatory mechanisms (STAR Methods). We identified 66 TFs in total, 41 of which showed significant enrichment in 6 groups of earlier identified DEGs that showed AD-stage-specific changes in at least two microglial states (Figures 5D and S9B). Notably, we found that 6 of these TFs also regulated the groups that they were part of, suggesting the importance of these coordinating TFs in the transcriptional regulatory circuits. For example, we observed that RELB, a subunit of NF- $\kappa$ B, showed significant enrichment of regulation of DEGs in G26, which are enriched in cytokine-mediated signaling (Figure 5C), consistent with the crucial role of RELB in neuroinflammation.<sup>43</sup>

### Association of microglial transcriptional states with AD genetics

We next sought to gain insight into the association of microglial states with AD genetics. We tested if microglial states can explain the heritability signal from genome-wide association studies (GWASs) summary statistics<sup>44–46</sup> using MAGMA<sup>47</sup> and found inflammatory MG8 and MG2 show the most significant enrichment, and MG0 (homeostatic), MG4 (lipid-processing), and MG11 (antiviral) also show significant enrichment (Figure 6A, STAR Methods). Remarkably, MG4 and MG8 were increased proportionally in AD individuals, and even though the homeostatic MG0 state showed no significant change in cell proportion (Figure 1C), the homeostatic genes were significantly down regulated in AD (Figure 5B). This consistency between simultaneous inflammation and downregulation of homeostatic processes highlights the importance of the homeostatic MG0,

#### Figure 5. Transcriptional changes of microglial states in AD

- (A) Bar plot showing the number of down-regulated and up-regulated DEGs for each microglial state in early response and late response.  
 (B) Transcriptional changes of 473 DEGs in eight groups during AD progression. Red in heatmap represents up regulated in AD progression, i.e., up regulated in early AD compared with non-AD and up regulated in late AD compared with early AD; and blue represents down regulation in AD progression. The numbers in the left block show the number of DEGs per group. The right shows the representative DEGs including known microglia markers, cytokines and their receptors, and top AD-risk genes (see more in Figure 6). The heatmap with all DEGs is in Figure S8.  
 (C) Gene-gene occurrence network per group of genes in Figure 5B. The edge represents that the two genes are involved in the same Gene Ontology terms. The representative enriched GO terms are shown along with the network.  
 (D) Heatmap to show the TF enrichment of DEGs in each group. Odds ratio represents the enrichment. Stars show the TFs that were also differentially expressed and belong to the corresponding group. See also Figures S7–S9 and Table S1, pages 10–11.

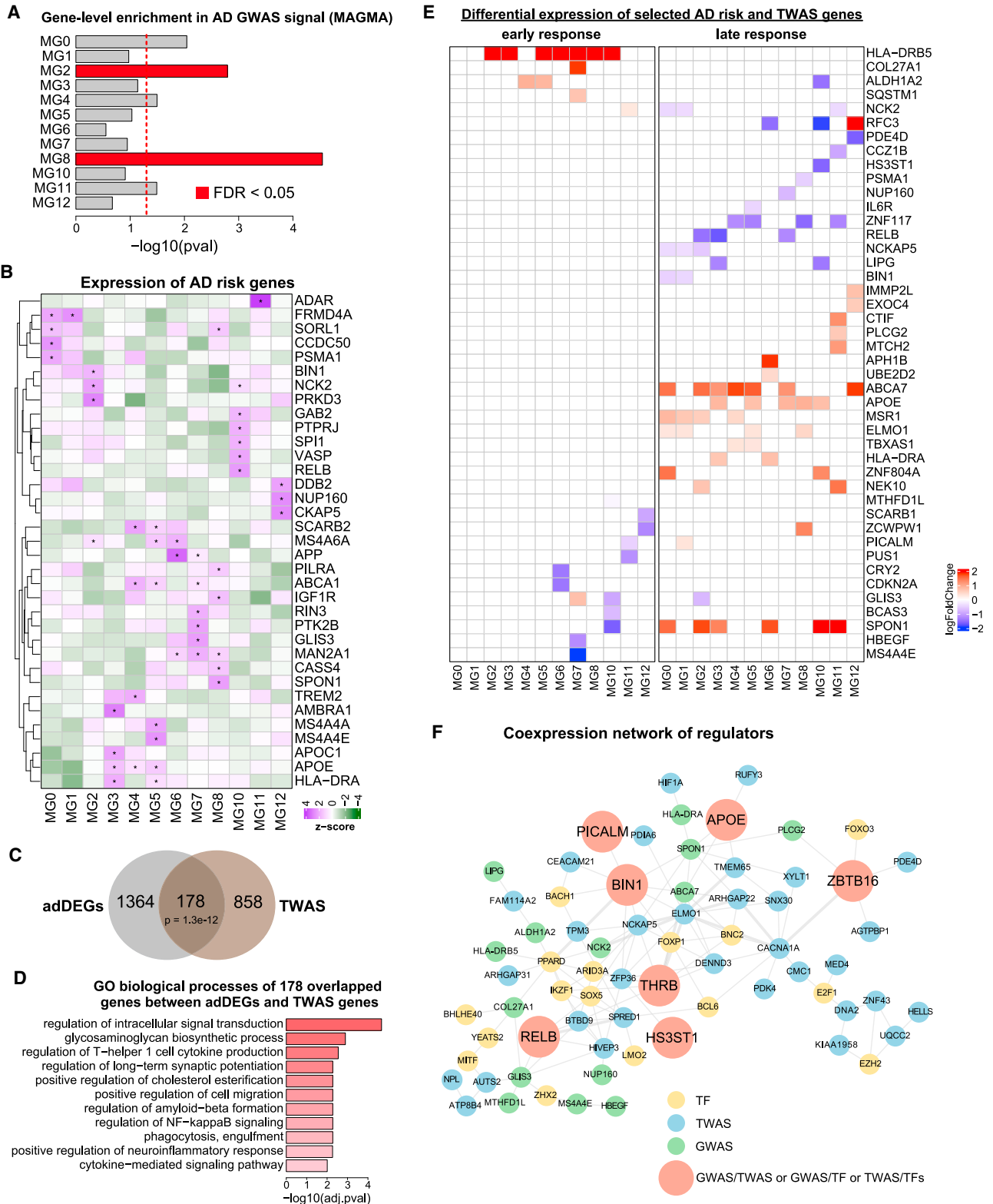


**Figure 6. Association of microglial transcriptional states with AD genetics**

(A) Gene-level enrichment in GWAS signals to associate microglial states with AD genetics using MAGMA. The  $-\log_{10}(p \text{ value})$  is shown in the barplot. The red dashed line shows the  $p \text{ value} < 0.05$  as a cutoff. The red bars show  $FDR < 0.05$  as a cutoff.

(legend continued on next page)

lipid-processing MG4, and inflammatory MG8 states in AD progression. Additionally, we found that distinct microglial states show significant association in lupus, ulcerative colitis, and triglyceride GWAS signals and weak association in multiple brain disorders (Figure S10A).

In addition to the overall enrichment of microglial states in AD GWAS signals, we also found differences in microglial state-specific expression patterns of the top AD-risk genes (GWAS Catalog,<sup>48</sup> those that are associated with AD variants with p value <10e-8, Figure 6B, and p value <10e-5, Figure S10B). We found that 35 AD-risk genes (with p value <10e-8) were highly expressed in at least one microglial state (Figure 6B). For example, *TREM2*, encoding a lipid receptor, was highly expressed in lipid-processing MG4, consistent with its function on microglial cholesterol metabolism in AD pathology.<sup>49</sup>

To investigate if the 1,542 adDEGs are associated with genetic variants, we identified single-cell expression QTLs (eQTLs) in microglia followed by transcriptome wide association study (TWAS) to dissect the associations between genetically regulated gene expression and AD (STAR Methods). We identified 1,036 TWAS genes in microglia (Table S1, page 13) and found that 178 of them were also differentially expressed in AD progression (Figure 6C; Fisher's exact test, p value = 1.3e-12), suggesting that the differential expression of these genes may be directly regulated by genetic factors. Gene Ontology enrichment analysis revealed that these 178 genes were significantly enriched in regulation of intracellular signal transduction, cell migration, immune response, and amyloid-beta formation (Figure 6D).

Although the TWAS data associated a group of DEGs directly with AD genetics, AD-risk genes uncovered by TWAS could also be differentially expressed due to indirect regulation. To this end, we gauged the differential expression of the top AD-risk and TWAS genes in early response and late response for each microglial state, as we previously did for DEGs in Figure 5B, and identified 44 genes (AD risk, TWAS, or both) showing differential expression in single or multiple states (Figure 6F). We found that 17 genes showed differential expression in the early stage while 34 genes showed differential expression in the late stage across multiple states. This suggests that the genetic effect on gene expression in AD may be time sensitive, underscoring the potential significance of stage-specific therapeutics. Interestingly, we observed that only three genes (*APOE*, *BIN1*, and *PICALM*) were both AD-risk and TWAS genes, suggesting their potential crucial functions in AD progression.

Lastly, to investigate the potential regulatory relationships between regulators, we built a co-expression network for potential regulators, including differential AD-risk genes (GWAS), TWAS

genes, and upstream TFs of DEGs, by measuring the co-expression between two genes (correlation test p value <0.01) in each microglia stage in early and late responses and aggregating the co-expression across all comparisons together (Figure 6F; STAR Methods). We found that seven regulators (*APOE*, *BIN1*, *RELB*, *PICALM*, *THRB*, *ZBTB16*, and *HS3ST1*) belonged to two categories (GWAS/TWAS, GWAS/TF, or TWAS/TF). Of note is that *BIN1* (GWAS/TWAS) and *RELB* (GWAS/TF) were highly correlated and simultaneously differentially expressed across multiple microglia states (Figures 6E and 6F), consistent with their functions as key regulators in inflammatory response.<sup>50,51</sup> This co-expression network analysis provides insight to dissect the genetic regulatory pathways and possible cooperative mechanisms in microglial response to AD progression, potentially guiding cell-state-specific and disease-specific AD therapeutics.

## DISCUSSION

Our findings establish that the rich diversity of microglial transcriptional states captured by snRNA-seq profiling is not fully represented by epigenome states defined through snATAC-seq. This conflict between transcriptional programs and chromatin architecture suggests that microglia may retain a relatively permissive chromatin landscape that is crucial to allow dynamic state transitions in response to microenvironment changes. We propose that state transitions can be mediated via the transcriptional activity of master regulator TFs and define a framework by which the activity of these factors may govern microglial cellular states.

Although we identified a large microglial fraction within the human brain that is characterized by signatures of DAM states in MG3 ribosome biogenesis, we did not identify enrichment of these cells in AD subjects as previously demonstrated in AD mouse models.<sup>5</sup> Notably, unlike the mouse brain, DAM signatures are lowly enriched across all microglial states in our dataset (with the only exception being the HOM MG0). Species-specific differences may account for such divergent observations in disease-state signatures, while the relatively greater diversity of microglial states observed in the human brain could reflect specialized microglial functions in humans pertaining to lipid mobilization and inflammation.

Our data supports the concept that inflammation and lipid metabolism are tightly linked processes, and critically involved in the contribution of microglia to AD pathogenesis.<sup>52</sup> According to our state- and stage-specific differential analysis, inflammatory processes precede lipid regulation in microglia during disease progression. Through TF regulatory networks, we have identified that the lipid-processing MG4 state is closely linked

(B) Expression patterns of top AD-risk genes (GWAS p value < 10e-8) in 12 microglial states. The stars highlight the genes with specifically high expression in the corresponding state.

(C) Venn diagram showing the significant overlap between DEGs and TWAS genes, evaluated by Fisher's exact test.

(D) The representative enriched Gene Ontology biological process of 178 overlapping genes between DEGs and TWAS genes. The -log<sub>10</sub> (p value) is shown in the barplot.

(E) Transcriptional changes of 44 AD-risk genes or TWAS genes in the early and late stages of AD in each microglial state. The log<sub>2</sub>FoldChange calculated by edgeR shows the up/down regulation in AD progression. The red represents the up regulation and the blue represents the down regulation in AD progression.

(F) Co-expression network of regulators. The regulators include AD-risk genes, TWAS genes, and TFs, denoted by nodes. The size of nodes represents the number of categories that one node belongs to. The edge represents the co-expression in at least one comparison (early or late) in each state, weighted by the times of co-expression occurrence. See also Figure S10 and Table S1, pages 12–13.

to MG8 inflammatory state. Although we did not empirically determine the relationship between these two clusters, it's plausible that MG4–MG8 represents an intersection of microglial immunometabolism that is critical to the pathophysiology and progression of AD.

Collectively, our study provides the high resolution required to define the association of microglial cellular states with clinical and pathological variables, disease stages, and AD genetics. Through differential gene expression analysis, our data defines the transcriptional changes associated with microglial states that occur in a disease-stage-specific manner, providing a road-map for the development of therapies aimed at curbing neuroinflammation with disease-stage specificity.

### Limitations of the study

Although many studies have characterized the transcriptional profile of microglia, it is important to note that methodological differences may impact the conservation of disease signatures across studies. These differences include the source of tissue, isolation method, and the microglia enrichment strategy. Additional factors such as the low number of nuclei recovered per subject or the sparsity of single-cell data may also affect the data, particularly the DEGs analysis. Lastly, experiments employing cellular reprogramming technologies in this study would be strengthened with the addition of orthogonal experimental approaches.

### STAR★METHODS

Detailed methods are provided in the online version of this paper and include the following:

- **KEY RESOURCES TABLE**
- **RESOURCE AVAILABILITY**
  - Lead contact
  - Materials availability
  - Data and code availability
- **EXPERIMENTAL MODEL AND SUBJECT DETAILS**
  - Human postmortem brain samples from ROSMAP
  - Culture of iPSC lines
- **METHOD DETAILS**
  - Nuclei isolation from frozen postmortem brain tissue, snRNA-seq and snATAC-seq
  - snRNA-seq data processing
  - snATAC-seq data processing
  - *In silico* sorting to enrich immune cells and cell type annotation in snRNA-seq data
  - Cell proportional analysis
  - Microglia epigenetic state annotation
  - Peak calling and differential peak analysis
  - Co-accessibility analysis
  - Identification of differentially expressed genes in AD progression
  - Comparison with public datasets
  - Prediction of upstream transcription factors
  - Immunohistochemistry staining
  - RNAscope and HiPlex
  - Microglia induction protocol

- CRISPRi in iMGLs for MG10 transcription factor repression
- Nuclei isolation from iMGLs for snRNA-Seq
- Calcium imaging
- Transcriptional time point analysis following inflammatory stimulation
- Homeostatic transcription factor overexpression: Plasmid cloning, lentivirus production and homeostatic assessment
- Gene Ontology enrichment analysis
- Gene-level enrichment in GWAS signal by MAGMA
- Expression and changes of AD-risk genes
- Microglia sc-eQTLs analysis
- TWAS analysis
- Co-expression network analysis

### ● QUANTIFICATION AND STATISTICAL ANALYSIS

### SUPPLEMENTAL INFORMATION

Supplemental information can be found online at <https://doi.org/10.1016/j.cell.2023.08.037>.

### ACKNOWLEDGMENTS

We thank the study participants and staff of the Rush Alzheimer's Disease Center. This Tsai lab research was made possible through the generous support of the Robert A. and Renee E. Belfer Family Foundation, the JPB Foundation, Eduardo Eurnekian, Joseph P. DiSabato and Nancy E. Sakamoto, Donald A. and Glenda G. Mattes, Lester A. Gimpelson, Paul Slavik, David Emmes, and Thomas Stocky and Avni Shah. This work was also supported in part by NIH grants AG054012, AG058002, AG062377, NS110453, NS115064, AG062335, NS127187, and AG074003 (M.K. and L.-H.T.); AG067151, AG081017, NS129032, AG077227, and MH109978 (M.K.); 1RF1AG054321 (L.-H.T.); P30AG10161, P30AG72975, R01AG15819, R01AG17917, U01AG46152, U01AG61356, and R01AG57473 (D.A.B.); and grants from the Cure Alzheimer's Fund CIRCUITS consortium (M.K. and L.-H.T.). M.B.V. is supported by the Howard Hughes Medical Institute Hanna H. Gray Postdoctoral Fellowship. We thank Amy Grayson and Patricia Purcell for scientific suggestions.

### AUTHOR CONTRIBUTIONS

N.S., M.B.V., L.-H.T., and M.K. conceived and designed the study; M.K. and L.-H.T. supervised the study; N.S. developed the computational framework and conducted data analysis with assistance from Y.P.P., X.X., C.A.B., B.T.J., and Y.T.; M.B.V., S.V., N.L., X.L., A.N.S., and S.P. performed experiments and analyzed results; K.G., H.M., X.J., and A.P.N. performed snRNA-seq and snATAC-seq profiling; N.S., M.B.V., N.L., and A.N.S. wrote methods; D.A.B. provided postmortem samples and scientific input; and N.S., M.B.V., L.-H.T. and M.K. wrote and revised the manuscript with comments from all authors.

### DECLARATION OF INTERESTS

L.-H.T. is a member of the Scientific Advisory Board of Cognito Therapeutics, 4M Therapeutics, Cell Signaling Technology, and Souvien Therapeutics, which has no association to this study.

Received: September 22, 2022

Revised: March 21, 2023

Accepted: August 29, 2023

Published: September 28, 2023



REFERENCES

- Butovsky, O., and Weiner, H.L. (2018). Microglial signatures and their role in health and disease. *Nat. Rev. Neurosci.* *19*, 622–635.
- Ellwanger, D.C., Wang, S., Brioschi, S., Shao, Z., Green, L., Case, R., Yoo, D., Weishuhn, D., Rathanaswami, P., Bradley, J., et al. (2021). Prior activation state shapes the microglia response to antihuman TREM2 in a mouse model of Alzheimer's disease. *Proc. Natl. Acad. Sci. USA* *118*, e2017742118. <https://doi.org/10.1073/pnas.2017742118>.
- Friedman, B.A., Srinivasan, K., Ayalon, G., Meilandt, W.J., Lin, H., Huntley, M.A., Cao, Y., Lee, S.-H., Haddick, P.C.G., Ngu, H., et al. (2018). Diverse Brain Myeloid Expression Profiles Reveal Distinct Microglial Activation States and Aspects of Alzheimer's Disease Not Evident in Mouse Models. *Cell Rep.* *22*, 832–847.
- Hammond, T.R., Dufort, C., Dissing-Olesen, L., Giera, S., Young, A., Wysocki, A., Walker, A.J., Gergits, F., Segel, M., Nemesh, J., et al. (2019). Single-Cell RNA Sequencing of Microglia throughout the Mouse Lifespan and in the Injured Brain Reveals Complex Cell-State Changes. *Immunity* *50*, 253–271.e6.
- Keren-Shaul, H., Spinrad, A., Weiner, A., Matcovitch-Natan, O., Dvir-Szternfeld, R., Ulland, T.K., David, E., Baruch, K., Lara-Astaiso, D., Toth, B., et al. (2017). A Unique Microglia Type Associated with Restricting Development of Alzheimer's Disease. *Cell* *169*, 1276–1290.e17.
- Mathys, H., Adaiakkan, C., Gao, F., Young, J.Z., Manet, E., Hemberg, M., De Jager, P.L., Ransohoff, R.M., Regev, A., and Tsai, L.-H. (2017). Temporal Tracking of Microglia Activation in Neurodegeneration at Single-Cell Resolution. *Cell Rep.* *21*, 366–380.
- Sala Frigerio, C., Wolfs, L., Fattorelli, N., Thrupp, N., Voytyuk, I., Schmidt, I., Mancuso, R., Chen, W.-T., Woodbury, M.E., Srivastava, G., et al. (2019). The Major Risk Factors for Alzheimer's Disease: Age, Sex, and Genes Modulate the Microglia Response to A $\beta$  Plaques. *Cell Rep.* *27*, 1293–1306.e6.
- Srinivasan, K., Friedman, B.A., Etcheberria, A., Huntley, M.A., van der Brug, M.P., Foreman, O., Paw, J.S., Modrusan, Z., Beach, T.G., Serrano, G.E., and Hansen, D.V. (2020). Alzheimer's Patient Microglia Exhibit Enhanced Aging and Unique Transcriptional Activation. *Cell Rep.* *31*, 107843.
- Gerrits, E., Brouwer, N., Kooistra, S.M., Woodbury, M.E., Vermeiren, Y., Lambourne, M., Mulder, J., Kummer, M., Möller, T., Biber, K., et al. (2021). Distinct amyloid- $\beta$  and tau-associated microglia profiles in Alzheimer's disease. *Acta Neuropathol.* *141*, 681–696.
- Grubman, A., Choo, X.Y., Chew, G., Ouyang, J.F., Sun, G., Croft, N.P., Rossello, F.J., Simmons, R., Buckberry, S., Landin, D.V., et al. (2021). Transcriptional signature in microglia associated with A $\beta$  plaque phagocytosis. *Nat. Commun.* *12*, 3015.
- Mathys, H., Davila-Velderrain, J., Peng, Z., Gao, F., Mohammadi, S., Young, J.Z., Menon, M., He, L., Abdurrob, F., Jiang, X., et al. (2019). Single-cell transcriptomic analysis of Alzheimer's disease. *Nature* *570*, 332–337.
- Olah, M., Menon, V., Habib, N., Taga, M.F., Ma, Y., Yung, C.J., Cimpean, M., Khairallah, A., Coronas-Samano, G., Sankowski, R., et al. (2020). Single cell RNA sequencing of human microglia uncovers a subset associated with Alzheimer's disease. *Nat. Commun.* *11*, 6129.
- Sankowski, R., Böttcher, C., Masuda, T., Geirsdotir, L., Sagar, Sindram, E., Sindram, E., Seredenina, T., Muhs, A., Scheiwe, C., Shah, M.J., et al. (2019). Mapping microglia states in the human brain through the integration of high-dimensional techniques. *Nat. Neurosci.* *22*, 2098–2110.
- Bennett, D.A., Buchman, A.S., Boyle, P.A., Barnes, L.L., Wilson, R.S., and Schneider, J.A. (2018). Religious Orders Study and Rush Memory and Aging Project. *J. Alzheimers Dis.* *64*, S161–S189.
- Mathys, H., Peng, Z., Boix, C., Victor, M.B., Leary, N., Abdelhady, G., Jiang, X., Ng, A.P., Ghafari, K., and Babu, S. (2023). Single-cell atlas reveals correlates of high cognitive function, dementia, and resilience to Alzheimer's disease pathology. *Cell* *186*. <https://doi.org/10.1016/j.cell.2023.08.039>.
- Garcia, F.J., Sun, N., Lee, H., Godlewski, B., Mathys, H., Galani, K., Zhou, B., Jiang, X., Ng, A.P., Mantero, J., et al. (2022). Single-cell dissection of the human brain vasculature. *Nature* *603*, 893–899.
- Sun, N., Akay, L.A., Murdock, M.H., Park, Y., Galiana-Melendez, F., Bubnys, A., Galani, K., Mathys, H., Jiang, X., Ng, A.P., et al. (2023). Single-nucleus multiregion transcriptomic analysis of brain vasculature in Alzheimer's disease. *Nat. Neurosci.* *26*, 970–982.
- Liu, H., Leak, R.K., and Hu, X. (2016). Neurotransmitter receptors on microglia. *Stroke Vasc. Neurol.* *1*, 52–58.
- Krasemann, S., Madore, C., Cialic, R., Baufeld, C., Calcagno, N., El Fattimy, R., Beckers, L., O'Loughlin, E., Xu, Y., Fanek, Z., et al. (2017). The TREM2-APOE Pathway Drives the Transcriptional Phenotype of Dysfunctional Microglia in Neurodegenerative Diseases. *Immunity* *47*, 566–581.e9.
- McQuade, A., Coburn, M., Tu, C.H., Hasselmann, J., Davtyan, H., and Blurton-Jones, M. (2018). Development and validation of a simplified method to generate human microglia from pluripotent stem cells. *Mol. Neurodegener.* *13*, 67.
- Xiong, X., James, B.T., Boix, C.A., Park, Y.P., Galani, K., Victor, M.B., Sun, N., Hou, L., Dileep, V., Ho, L.-L., et al. (2023). Epigenomic dissection of Alzheimer's disease pinpoints causal genetic variants and reveals epigenome erosion. *Cell* *186*. <https://doi.org/10.1016/j.cell.2023.08.040>.
- Wang, K.X., and Denhardt, D.T. (2008). Osteopontin: role in immune regulation and stress responses. *Cytokine Growth Factor Rev.* *19*, 333–345.
- da Fonseca, A.C.C., Matias, D., Garcia, C., Amaral, R., Geraldo, L.H., Freitas, C., and Lima, F.R.S. (2014). The impact of microglial activation on blood-brain barrier in brain diseases. *Front. Cell. Neurosci.* *8*, 362.
- Chen, E.Y., Tan, C.M., Kou, Y., Duan, Q., Wang, Z., Meirelles, G.V., Clark, N.R., and Ma'ayan, A. (2013). Enrichr: interactive and collaborative HTML5 gene list enrichment analysis tool. *BMC Bioinf.* *14*, 128.
- Smith, A.M., Gibbons, H.M., Oldfield, R.L., Bergin, P.M., Mee, E.W., Faull, R.L.M., and Dragunow, M. (2013). The transcription factor PU.1 is critical for viability and function of human brain microglia. *Glia* *67*, 929–942.
- Kim, S., Yu, N.-K., and Kaang, B.-K. (2015). CTCF as a multifunctional protein in genome regulation and gene expression. *Exp. Mol. Med.* *47*, e166.
- Helin, K., Wu, C.L., Fattaey, A.R., Lees, J.A., Dynlacht, B.D., Ngwu, C., and Harlow, E. (1993). Heterodimerization of the transcription factors E2F-1 and DP-1 leads to cooperative trans-activation. *Genes Dev.* *7*, 1850–1861.
- Chen, H.-W., King, K., Tu, J., Sanchez, M., Luster, A.D., and Shresta, S. (2013). The roles of IRF-3 and IRF-7 in innate antiviral immunity against dengue virus. *J. Immunol.* *191*, 4194–4201.
- Shang, Y.C., Chong, Z.Z., Hou, J., and Maiese, K. (2009). The forkhead transcription factor FOXO3a controls microglial inflammatory activation and eventual apoptotic injury through caspase 3. *Curr. Neurovasc. Res.* *6*, 20–31.
- March-Diaz, R., Lara-Ureña, N., Romero-Molina, C., Heras-Garvin, A., Ortega-de San Luis, C., Alvarez-Vergara, M.I., Sanchez-Garcia, M.A., Sanchez-Mejias, E., Davila, J.C., Rosales-Nieves, A.E., et al. (2021). Hypoxia compromises the mitochondrial metabolism of Alzheimer's disease microglia via HIF1. *Nat. Aging* *1*, 385–399.
- Lum, J.J., Bui, T., Gruber, M., Gordan, J.D., DeBerardinis, R.J., Covello, K.L., Simon, M.C., and Thompson, C.B. (2007). The transcription factor HIF-1 $\alpha$  plays a critical role in the growth factor-dependent regulation of both aerobic and anaerobic glycolysis. *Genes Dev.* *21*, 1037–1049.
- Li, H.-S., Zhou, Y.-N., Li, L., Li, S.-F., Long, D., Chen, X.-L., Zhang, J.-B., Feng, L., and Li, Y.-P. (2019). HIF-1 $\alpha$  protects against oxidative stress by directly targeting mitochondria. *Redox Biol.* *25*, 101109.

33. Garcia-Alonso, L., Holland, C.H., Ibrahim, M.M., Turei, D., and Saez-Rodríguez, J. (2019). Benchmark and integration of resources for the estimation of human transcription factor activities. *Genome Res.* *29*, 1363–1375.
34. Timmerman, R., Burm, S.M., and Bajramovic, J.J. (2018). An Overview of Methods to Study Microglia. *Front. Cell. Neurosci.* *12*, 242.
35. Victor, M.B., Leary, N., Luna, X., Meharena, H.S., Scannail, A.N., Bozzelli, P.L., Samaan, G., Murdock, M.H., von Maydell, D., Effenberger, A.H., et al. (2022). Lipid accumulation induced by APOE4 impairs microglial surveillance of neuronal-network activity. *Cell Stem Cell* *29*, 1197–1212.e8.
36. Colombo, G., Cubero, R.J.A., Kanari, L., Venturino, A., Schulz, R., Scolamiero, M., Agerberg, J., Mathys, H., Tsai, L.-H., Chachóski, W., et al. (2022). A tool for mapping microglial morphology, morphOMiCs, reveals brain-region and sex-dependent phenotypes. *Nat. Neurosci.* *25*, 1379–1393.
37. Butovsky, O., Jedrychowski, M.P., Moore, C.S., Cialic, R., Lanser, A.J., Gabriely, G., Koeglsperger, T., Dake, B., Wu, P.M., Doykan, C.E., et al. (2014). Identification of a unique TGF- $\beta$ -dependent molecular and functional signature in microglia. *Nat. Neurosci.* *17*, 131–143.
38. Finak, G., McDavid, A., Yajima, M., Deng, J., Gersuk, V., Shalek, A.K., Slichter, C.K., Miller, H.W., McElrath, M.J., Pric, M., et al. (2015). MAST: a flexible statistical framework for assessing transcriptional changes and characterizing heterogeneity in single-cell RNA sequencing data. *Genome Biol.* *16*, 278.
39. Zimmerman, K.D., Espeland, M.A., and Langefeld, C.D. (2021). A practical solution to pseudoreplication bias in single-cell studies. *Nat. Commun.* *12*, 738.
40. Robinson, M.D., McCarthy, D.J., and Smyth, G.K. (2010). edgeR: a Bioconductor package for differential expression analysis of digital gene expression data. *Bioinformatics* *26*, 139–140.
41. Ji, Y., Wang, X., Kalicki, C., Menta, B.W., Baumgardner, M., Koppel, S.J., Weidling, I.W., Perez-Ortiz, J., Wilkins, H.M., and Swerdlow, R.H. (2019). Effects of Microglial Cytokines on Alzheimer's Disease-Related Phenomena. *J. Alzheimers Dis.* *67*, 1021–1034.
42. Wang, W.-Y., Tan, M.-S., Yu, J.-T., and Tan, L. (2015). Role of pro-inflammatory cytokines released from microglia in Alzheimer's disease. *Ann. Transl. Med.* *3*, 136.
43. Mockenhaupt, K., Gonsiewski, A., and Kordula, T. (2021). RelB and Neuroinflammation. *Cells* *10*, 1609. <https://doi.org/10.3390/cells10071609>.
44. Jansen, I.E., Savage, J.E., Watanabe, K., Bryois, J., Williams, D.M., Steinberg, S., Sealock, J., Karlsson, I.K., Hägg, S., Athanasiu, L., et al. (2019). Genome-wide meta-analysis identifies new loci and functional pathways influencing Alzheimer's disease risk. *Nat. Genet.* *51*, 404–413.
45. Kunkle, B.W., Grenier-Boley, B., Sims, R., Bis, J.C., Damotte, V., Naj, A.C., Boland, A., Vronskaya, M., van der Lee, S.J., Amlie-Wolf, A., et al. (2019). Genetic meta-analysis of diagnosed Alzheimer's disease identifies new risk loci and implicates A $\beta$ , tau, immunity and lipid processing. *Nat. Genet.* *51*, 414–430.
46. Kang, S., Gim, J., Lee, J., Gunasekaran, T.I., Choi, K.Y., Lee, J.J., Seo, E.H., Ko, P.-W., Chung, J.Y., Choi, S.-M., et al. (2021). Potential Novel Genes for Late-Onset Alzheimer's Disease in East-Asian Descent Identified by APOE-Stratified Genome-Wide Association Study. *J. Alzheimers Dis.* *82*, 1451–1460.
47. Skene, N.G., Bryois, J., Bakken, T.E., Breen, G., Crowley, J.J., Gaspar, H.A., Giusti-Rodríguez, P., Hodge, R.D., Miller, J.A., Muñoz-Manchado, A.B., et al. (2018). Genetic identification of brain cell types underlying schizophrenia. *Nat. Genet.* *50*, 825–833.
48. Buniello, A., MacArthur, J.A.L., Cerezo, M., Harris, L.W., Hayhurst, J., Malangone, C., McMahon, A., Morales, J., Mountjoy, E., Sollis, E., et al. (2019). The NHGRI-EBI GWAS Catalog of published genome-wide association studies, targeted arrays and summary statistics 2019. *Nucleic Acids Res.* *47*, D1005–D1012.
49. Nugent, A.A., Lin, K., van Lengerich, B., Lianoglou, S., Przybyla, L., Davis, S.S., Llapashtica, C., Wang, J., Kim, D.J., Xia, D., et al. (2020). TREM2 Regulates Microglial Cholesterol Metabolism upon Chronic Phagocytic Challenge. *Neuron* *105*, 837–854.e9.
50. Sudwarts, A., Ramesha, S., Gao, T., Ponnusamy, M., Wang, S., Hansen, M., Kozlova, A., Bitarafan, S., Kumar, P., Beaulieu-Abdelahad, D., et al. (2022). BIN1 is a key regulator of proinflammatory and neurodegeneration-related activation in microglia. *Mol. Neurodegener.* *17*, 33.
51. Yang, M.-G., Sun, L., Han, J., Zheng, C., Liang, H., Zhu, J., and Jin, T. (2019). Biological characteristics of transcription factor RelB in different immune cell types: implications for the treatment of multiple sclerosis. *Mol. Brain* *12*, 115.
52. Bernier, L.-P., York, E.M., and MacVicar, B.A. (2020). Immunometabolism in the Brain: How Metabolism Shapes Microglial Function. *Trends Neurosci.* *43*, 854–869.
53. Horlbeck, M.A., Gilbert, L.A., Villalta, J.E., Adamson, B., Pak, R.A., Chen, Y., Fields, A.P., Park, C.Y., Corn, J.E., Kampmann, M., and Weissman, J.S. (2016). Compact and highly active next-generation libraries for CRISPR-mediated gene repression and activation. *Elife* *5*, e19760. <https://doi.org/10.7554/eLife.19760>.
54. Hao, Y., Hao, S., Andersen-Nissen, E., Mauck, W.M., 3rd, Zheng, S., Butler, A., Lee, M.J., Wilk, A.J., Darby, C., Zager, M., et al. (2021). Integrated analysis of multimodal single-cell data. *Cell* *184*, 3573–3587.e29.
55. Phipson, B., Sim, C.B., Porrello, E.R., Hewitt, A.W., Powell, J., and Oshlack, A. (2022). propeller: testing for differences in cell type proportions in single cell data. *Bioinformatics* *38*, 4720–4726.
56. McGinnis, C.S., Murrow, L.M., and Gartner, Z.J. (2019). DoubletFinder: Doublet Detection in Single-Cell RNA Sequencing Data Using Artificial Nearest Neighbors. *Cell Syst.* *8*, 329–337.e4.
57. Granja, J.M., Corces, M.R., Pierce, S.E., Bagdatli, S.T., Choudhry, H., Chang, H.Y., and Greenleaf, W.J. (2021). ArchR is a scalable software package for integrative single-cell chromatin accessibility analysis. *Nat. Genet.* *53*, 403–411.
58. Zhang, Y., Liu, T., Meyer, C.A., Eeckhoutte, J., Johnson, D.S., Bernstein, B.E., Nussbaum, C., Myers, R.M., Brown, M., Li, W., and Liu, X.S. (2008). Model-based analysis of ChIP-Seq (MACS). *Genome Biol.* *9*, R137.
59. Heinz, S., Benner, C., Spann, N., Bertolino, E., Lin, Y.C., Laslo, P., Cheng, J.X., Murre, C., Singh, H., and Glass, C.K. (2010). Simple combinations of lineage-determining transcription factors prime cis-regulatory elements required for macrophage and B cell identities. *Mol. Cell* *38*, 576–589.
60. Kuleshov, M.V., Jones, M.R., Rouillard, A.D., Fernandez, N.F., Duan, Q., Wang, Z., Koplev, S., Jenkins, S.L., Jagodnik, K.M., Lachmann, A., et al. (2016). Enrichr: a comprehensive gene set enrichment analysis web server 2016 update. *Nucleic Acids Res.* *44*, W90–W97.
61. Gu, Z., Eils, R., and Schlesner, M. (2016). Complex heatmaps reveal patterns and correlations in multidimensional genomic data. *Bioinformatics* *32*, 2847–2849.
62. Gu, Z. (2022). Complex heatmap visualization. *Imeta* *7*, e43. <https://doi.org/10.1002/imt2.43>.
63. Bennett, D.A., Wilson, R.S., Schneider, J.A., Evans, D.A., Beckett, L.A., Aggarwal, N.T., Barnes, L.L., Fox, J.H., and Bach, J. (2002). Natural history of mild cognitive impairment in older persons. *Neurology* *59*, 198–205.
64. Bennett, D.A., Wilson, R.S., Schneider, J.A., Evans, D.A., Aggarwal, N.T., Arnold, S.E., Cochran, E.J., Berry-Kravis, E., and Bienias, J.L. (2003). Apolipoprotein E epsilon4 allele, AD pathology, and the clinical expression of Alzheimer's disease. *Neurology* *60*, 246–252.
65. Bennett, D.A., Schneider, J.A., Arvanitakis, Z., Kelly, J.F., Aggarwal, N.T., Shah, R.C., and Wilson, R.S. (2006). Neuropathology of older persons without cognitive impairment from two community-based studies. *Neurology* *66*, 1837–1844.
66. Bennett, D.A., Schneider, J.A., Wilson, R.S., Bienias, J.L., and Arnold, S.E. (2004). Neurofibrillary tangles mediate the association of amyloid

- load with clinical Alzheimer disease and level of cognitive function. *Arch. Neurol.* **67**, 378–384.
67. Bennett, D.A., Schneider, J.A., Aggarwal, N.T., Arvanitakis, Z., Shah, R.C., Kelly, J.F., Fox, J.H., Cochran, E.J., Arends, D., Treinkman, A.D., and Wilson, R.S. (2006). Decision rules guiding the clinical diagnosis of Alzheimer's disease in two community-based cohort studies compared to standard practice in a clinic-based cohort study. *Neuroepidemiology* **27**, 169–176.
  68. Zheng, G.X.Y., Terry, J.M., Belgrader, P., Ryvkin, P., Bent, Z.W., Wilson, R., Ziraldo, S.B., Wheeler, T.D., McDermott, G.P., Zhu, J., et al. (2017). Massively parallel digital transcriptional profiling of single cells. *Nat. Commun.* **8**, 14049.
  69. Korsunsky, I., Millard, N., Fan, J., Slowikowski, K., Zhang, F., Wei, K., Baiglaenko, Y., Brenner, M., Loh, P.-R., and Raychaudhuri, S. (2019). Fast, sensitive and accurate integration of single-cell data with Harmony. *Nat. Methods* **16**, 1289–1296.
  70. Satpathy, A.T., Granja, J.M., Yost, K.E., Qi, Y., Meschi, F., McDermott, G.P., Olsen, B.N., Mumbach, M.R., Pierce, S.E., Corces, M.R., et al. (2019). Massively parallel single-cell chromatin landscapes of human immune cell development and intratumoral T cell exhaustion. *Nat. Biotechnol.* **37**, 925–936.
  71. Zhang, X., Lan, Y., Xu, J., Quan, F., Zhao, E., Deng, C., Luo, T., Xu, L., Liao, G., Yan, M., et al. (2019). CellMarker: a manually curated resource of cell markers in human and mouse. *Nucleic Acids Res.* **47**, D721–D728.
  72. Wang, D., Liu, S., Warrell, J., Won, H., Shi, X., Navarro, F.C.P., Clarke, D., Gu, M., Emani, P., Yang, Y.T., et al. (2018). Comprehensive functional genomic resource and integrative model for the human brain. *Science* **362**, eaat8464. <https://doi.org/10.1126/science.aat8464>.
  73. McLean, C.Y., Bristor, D., Hiller, M., Clarke, S.L., Schaar, B.T., Lowe, C.B., Wenger, A.M., and Bejerano, G. (2010). GREAT improves functional interpretation of cis-regulatory regions. *Nat. Biotechnol.* **28**, 495–501.
  74. Xie, Z., Bailey, A., Kuleshov, M.V., Clarke, D.J.B., Evangelista, J.E., Jenkins, S.L., Lachmann, A., Wojciechowicz, M.L., Kropiwnicki, E., Jagodnik, K.M., et al. (2021). Gene Set Knowledge Discovery with Enrichr. *Curr. Protoc.* **1**, e90.
  75. Victor, M.B., Richner, M., Hermanstynne, T.O., Ransdell, J.L., Sobieski, C., Deng, P.-Y., Klyachko, V.A., Nerbonne, J.M., and Yoo, A.S. (2014). Generation of human striatal neurons by microRNA-dependent direct conversion of fibroblasts. *Neuron* **84**, 311–323.
  76. Ashburner, M., Ball, C.A., Blake, J.A., Botstein, D., Butler, H., Cherry, J.M., Davis, A.P., Dolinski, K., Dwight, S.S., Eppig, J.T., et al. (2000). Gene Ontology: tool for the unification of biology. *Nat. Genet.* **25**, 25–29.
  77. The Gene Ontology Consortium (2019). The Gene Ontology Resource: 20 years and still GOing strong. *Nucleic Acids Res.* **47**, D330–D338.
  78. Finucane, H.K., Bulik-Sullivan, B., Gusev, A., Trynka, G., Reshef, Y., Loh, P.-R., Anttila, V., Xu, H., Zang, C., Farh, K., et al. (2015). Partitioning heritability by functional annotation using genome-wide association summary statistics. *Nat. Genet.* **47**, 1228–1235.
  79. Bentham, J., Morris, D.L., Graham, D.S.C., Pinder, C.L., Tomblason, P., Behrens, T.W., Martín, J., Fairfax, B.P., Knight, J.C., Chen, L., et al. (2015). Genetic association analyses implicate aberrant regulation of innate and adaptive immunity genes in the pathogenesis of systemic lupus erythematosus. *Nat. Genet.* **47**, 1457–1464.
  80. Jostins, L., Ripke, S., Weersma, R.K., Duerr, R.H., McGovern, D.P., Hui, K.Y., Lee, J.C., Schumm, L.P., Sharma, Y., Anderson, C.A., et al. (2012). Host-microbe interactions have shaped the genetic architecture of inflammatory bowel disease. *Nature* **491**, 119–124.
  81. Speliotes, E.K., Willer, C.J., Berndt, S.I., Monda, K.L., Thorleifsson, G., Jackson, A.U., Lango Allen, H., Lindgren, C.M., Luan, J., 'an, Mägi, R., et al. (2010). Association analyses of 249,796 individuals reveal 18 new loci associated with body mass index. *Nat. Genet.* **42**, 937–948.
  82. Teslovich, T.M., Musunuru, K., Smith, A.V., Edmondson, A.C., Stylianou, I.M., Koseki, M., Pirruccello, J.P., Ripatti, S., Chasman, D.I., Willer, C.J., et al. (2010). Biological, clinical and population relevance of 95 loci for blood lipids. *Nature* **466**, 707–713.
  83. Okada, Y., Wu, D., Trynka, G., Raj, T., Terao, C., Ikari, K., Kochi, Y., Ohmura, K., Suzuki, A., Yoshida, S., et al. (2014). Genetics of rheumatoid arthritis contributes to biology and drug discovery. *Nature* **506**, 376–381.
  84. Okbay, A., Baselmans, B.M.L., De Neve, J.-E., Turley, P., Nivard, M.G., Fontana, M.A., Meddens, S.F.W., Linnér, R.K., Rietveld, C.A., Derringer, J., et al. (2016). Genetic variants associated with subjective well-being, depressive symptoms, and neuroticism identified through genome-wide analyses. *Nat. Genet.* **48**, 624–633.
  85. Thorgeirsson, T.E., Gudbjartsson, D.F., Surakka, I., Vink, J.M., Amin, N., Geller, F., Sulem, P., Rafnar, T., Esko, T., Walter, S., et al. (2010). Sequence variants at CHRN3-CHRNA6 and CYP2A6 affect smoking behavior. *Nat. Genet.* **42**, 448–453.
  86. Schizophrenia Working Group of the Psychiatric Genomics Consortium (2014). Biological insights from 108 schizophrenia-associated genetic loci. *Nature* **511**, 421–427.
  87. International Multiple Sclerosis Genetics Consortium; Wellcome Trust Case Control Consortium 2, Sawcer, S., Hellenthal, G., Pirinen, M., Spencer, C.C.A., Patsopoulos, N.A., Moutsianas, L., Dilthey, A., Su, Z., et al. (2011). Genetic risk and a primary role for cell-mediated immune mechanisms in multiple sclerosis. *Nature* **476**, 214–219.
  88. Morris, A.P., Voight, B.F., Teslovich, T.M., Ferreira, T., Segre, A.V., Steinthorsdottir, V., Strawbridge, R.J., Khan, H., Grallert, H., Mahajan, A., et al. (2012). Large-scale association analysis provides insights into the genetic architecture and pathophysiology of type 2 diabetes. *Nat. Genet.* **44**, 981–990.
  89. Park, Y.P., and Kellis, M. (2021). CoCoA-diff: counterfactual inference for single-cell gene expression analysis. *Genome Biol.* **22**, 228.
  90. Barber, R.F., and Candès, E.J. (2015). Controlling the false discovery rate via knockoffs. *aos* **43**, 2055–2085.
  91. Wang, Y., Liu, X., Liu, L., and Niu, H. (2019). The Blessings of Multiple Causes. *Polymers* **11**, 1574–1596.
  92. Zhu, Z., Fan, Y., Kong, Y., Lv, J., and Sun, F. (2021). DeepLINK: Deep learning inference using knockoffs with applications to genomics. *Proc. Natl. Acad. Sci. USA* **118**, e2104683118. <https://doi.org/10.1073/pnas.2104683118>.
  93. Jiang, T., Li, Y., and Motsinger-Reif, A.A. (2021). Knockoff boosted tree for model-free variable selection. *Bioinformatics* **37**, 976–983.
  94. Candès, E., Fan, Y., Janson, L., and Lv, J. (2018). Panning for gold: model-X knockoffs for high dimensional controlled variable selection. *Journal of the Royal Society*.
  95. Gusev, A., Ko, A., Shi, H., Bhatia, G., Chung, W., Penninx, B.W.J.H., Jansen, R., de Geus, E.J.C., Boomsma, D.I., Wright, F.A., et al. (2016). Integrative approaches for large-scale transcriptome-wide association studies. *Nat. Genet.* **48**, 245–252.
  96. Gamazon, E.R., Wheeler, H.E., Shah, K.P., Mozaffari, S.V., Aquino-Michaels, K., Carroll, R.J., Eyler, A.E., Denny, J.C., GTEx Consortium, and Nicolae, D.L., et al. (2015). A gene-based association method for mapping traits using reference transcriptome data. *Nat. Genet.* **47**, 1091–1098.
  97. Berisa, T., and Pickrell, J.K. (2016). Approximately independent linkage disequilibrium blocks in human populations. *Bioinformatics* **32**, 283–285.
  98. Wang, G., Sarkar, A., Carbonetto, P., and Stephens, M. (2020). A simple new approach to variable selection in regression, with application to genetic fine-mapping. Preprint at bioRxiv. <https://doi.org/10.1101/501114>.
  99. Park, Y., Sarkar, A.K., He, L., Davila-Velderrain, J., De Jager, P.L., and Kellis, M. (2017). A Bayesian approach to mediation analysis predicts 206 causal target genes in Alzheimer's disease. Preprint at bioRxiv. <https://doi.org/10.1101/219428>.
  100. Shannon, P., Markiel, A., Ozier, O., Baliga, N.S., Wang, J.T., Ramage, D., Amin, N., Schwikowski, B., and Ideker, T. (2003). Cytoscape: a software environment for integrated models of biomolecular interaction networks. *Genome Res.* **13**, 2498–2504.

## STAR★METHODS

### KEY RESOURCES TABLE

REAGENT or RESOURCE	SOURCE	IDENTIFIER
<b>Antibodies</b>		
Guinea Pig Anti-IBA1	Synaptic Systems	Cat#822501; RRID:AB_2924932
Mouse Anti-IL1B	SantaCruz	Cat#sc-32294; RRID:AB_627790
Goat Anti-LRRK2	R&D Systems	Cat#AF6674; RRID:AB_10892534
Rabbit Anti-CPEB4	Abcam	Cat#ab224162
Mouse Anti-TMEM119	NovusBio	Cat#NBP2-76985
Rabbit Anti-RUNX2	Cell Signaling	Cat#12556S; RRID:AB_2732805
Rabbit Anti-IRF8	Cell Signaling	Cat# 83413S
Rabbit Anti-ELF1	Santa Cruz	Cat#sc133096; RRID:AB_2262155
Rabbit Anti-PPARG	Cell Signaling	Cat#2435S; RRID:AB_2166051
Rabbit Anti-SMAD3	Cell Signaling	Cat#9523S; RRID:AB_2193182
Rabbit Anti-P2RY12	Atlas Antibodies	Cat# HPA014518; RRID:AB_2669027
Alexa Fluor 505 (Donkey anti-Goat)	Thermo Fisher Scientific	Cat# A-48259
Alexa Fluor 488 (Donkey anti-Mouse)	Thermo Fisher Scientific	Cat# A-21202
Alexa Fluor 555 (Donkey anti-Rabbit)	Thermo Fisher Scientific	Cat# A-31572
Alexa Fluor 555 (Donkey anti-Mouse)	Thermo Fisher Scientific	Cat# A-31570
Alexa Fluor 647 (Donkey Anti-Guinea Pig)	Jackson Immuno Laboratories, Inc.	706-605-148
DAPI	Thermo Fisher Scientific	Cat# D1306
<b>Biological samples</b>		
See <a href="#">Table S1</a> for a list of brain samples.		N/A
<b>Chemicals, peptides, and recombinant proteins</b>		
Nuclei Isolation Reagents	Mathys et al. <sup>11</sup>	N/A
Matrigel	Corning	Cat # 354277
mTeSR1 media	STEMCELL Technologies	Cat# 05872
True black	Biotium	Cat#23007
Fluoromount-G	Southern Biotech	Cat#0100-01
Hoechst 33342	Sigma-Aldrich	Cat#94403
ReLeSR	STEMCELL Technologies	Cat#05872
ROCK inhibitor	BioVision	Cat#2342-25
DMEM/F12	Thermo Fisher Scientific	Cat#11330-057
Neurobasal media	Gibco	Cat#21103049
IL-34	PeprTech	Cat#200-34
m-CSF	PeprTech	Cat#300-25
CRISPRMAX	Invitrogen	Cat#CMAX00003
RNase Inhibitor (0.2 U/ $\mu$ L)	Thermo Fisher Scientific	AM2696
LPS (10 ng/mL)	Sigma	L-2654
DMNPE-Caged ATP	Fisher Scientific	Cat#1049
FLUO4-AM	Invitrogen	Cat# F14201
TNF $\alpha$	PeprTech	300-01A
INF $\gamma$	PeprTech	300-02
EcoDry Premix	Takara	Cat#639549
SsoFast EvaGreen Supermix	Bio-Rad	Cat#1725202
Pre-formed amyloid beta (1–42) fibrils	rPeptide	Cat#AF-1002-1

(Continued on next page)

**Continued**

REAGENT or RESOURCE	SOURCE	IDENTIFIER
ActinGreen 488 Readyprobes (Invitrogen #R37110)	Invitrogen	Cat#R37110
Chromium Single-Cell 3' Reagent Kits v3	10x Genomics	<a href="https://www.10xgenomics.com">https://www.10xgenomics.com</a>
STEMdiff Hematopoietic Kit	STEMCELL Technologies	Cat#05310
sgRNA Synthesis Kit	Thermo Fisher Scientific	Cat#A29377
Nuclei EZ Prep	Sigma-Aldrich	Cat#NUC101
Chromium Next GEM Single Cell 3' Reagent Kit v3.1	10x Genomics, Pleasanton, CA)	Cat#PN-1000268
RNeasy Plus Mini Kit	Qiagen	Cat#74134
<b>Critical commercial assays</b>		
RNAscope HiPlex Probe - Hs-FOXP1-T2	Advanced Cell Diagnostics	407231-T2
RNAscope HiPlex Probe - Hs-LRRK2-T1	Advanced Cell Diagnostics	421531-T1
RNAscope HiPlex Probe - Hs-RELB-T9	Advanced Cell Diagnostics	1236361-T9
RNAscope HiPlex Probe - Hs-CCL3-T8	Advanced Cell Diagnostics	455331-T8
RNAscope HiPlex Probe - Hs-TMEM163-T10	Advanced Cell Diagnostics	1200321-T10
RNAscope HiPlex Probe - Hs-CPEB4-T4	Advanced Cell Diagnostics	1063961-T4
RNAscope HiPlex Probe - Hs-P2RY12-T5	Advanced Cell Diagnostics	450391-T5
RNAscope HiPlex Probe - Hs-AIF1-T12	Advanced Cell Diagnostics	433121-T12
RNAscope HiPlex Probe - Hs-CX3CR1-T6	Advanced Cell Diagnostics	411251-T6
RNAscope HiPlex Probe - Hs-PPARG-O1-T4	Advanced Cell Diagnostics	864421-T4
RNAscope HiPlex Probe - Hs-APOE-T8	Advanced Cell Diagnostics	433091-T8
HiPlex12 Reagents Kit (488, 550; 650) Hs V2	Advanced Cell Diagnostics	324445
<b>Deposited data</b>		
Count Matrices and Metadata	This paper	<a href="http://compbio.mit.edu/microglia_states/">http://compbio.mit.edu/microglia_states/</a>
iMGLs bulk RNA-seq and snRNA-seq	This paper	GEO database: GSE227223
<b>Experimental models: Cell lines</b>		
HEK-293T cell line	ATCC	Cat#CRL-3216
CRISPRi iPSC line(dCas9-KRAB)	Allen Institute for Cell Science	Cat#AICS-0090 cL.391
<b>Oligonucleotides</b>		
FOXP0_1 guide RNA: GGAGGGGAAAGGAAGCGCC	Horlbeck et al. <sup>53</sup>	N/A
FOXP0_2 guide RNA: GTGGCGGCGCGAGCTGAC	Horlbeck et al. <sup>53</sup>	N/A
HIF1A_1 guide RNA: GCTGGCCGAAGCGACGAAGA	Horlbeck et al. <sup>53</sup>	N/A
HIF1A_2 guide RNA: GCCTCCTGTCCCCTCAGACG	Horlbeck et al. <sup>53</sup>	N/A
FOXP2_1 guide RNA: GAAGCCGGGAGACCAGACAC	Horlbeck et al. <sup>53</sup>	N/A
FOXP2_2 guide RNA: GAATCAGCATTTAATCACTA	Horlbeck et al. <sup>53</sup>	N/A
CCL3 qPCR FWD: AGTTCTCTGCATCACTTGCTG REV: CGGCTTCGCTTGGTTAGGAA	<a href="https://pga.mgh.harvard.edu/primerbank/">https://pga.mgh.harvard.edu/primerbank/</a>	N/A
PLEK qPCR FWD: AAGAAGGGGAGCGTGTCAAT REV: TCAGCGGATCATTCTTTGG	<a href="https://pga.mgh.harvard.edu/primerbank/">https://pga.mgh.harvard.edu/primerbank/</a>	N/A
NFKBIZ qPCR FWD: AGAGCCCCCTTTCAAGGTGT REV:TCCATCAGACAACGAATCGGG	<a href="https://pga.mgh.harvard.edu/primerbank/">https://pga.mgh.harvard.edu/primerbank/</a>	N/A

(Continued on next page)

**Continued**

REAGENT or RESOURCE	SOURCE	IDENTIFIER
RELB qPCR FWD:CAGCCTCGTGGGAAAGAC REV:GCCCAGGTTGTTAAACTGTGC	<a href="https://pga.mgh.harvard.edu/primerbank/">https://pga.mgh.harvard.edu/primerbank/</a>	N/A
NFKB1 qPCR FWD: AACAGAGAGGATTCGTTCCG REV:TTTGACCTGAGGGTAAGACTTCT	<a href="https://pga.mgh.harvard.edu/primerbank/">https://pga.mgh.harvard.edu/primerbank/</a>	N/A
TNFAIP3 qPCR FWD: TCCTCAGGCTTTGTATTGAGC REV:TGTGTATCGGTGCATGGTTTAA	<a href="https://pga.mgh.harvard.edu/primerbank/">https://pga.mgh.harvard.edu/primerbank/</a>	N/A
FAM129A qPCR FWD: GAAGAGGTTTAGTGCCCTCCT REV:CCTTCTCCTGTCGGAAGAATTG	<a href="https://pga.mgh.harvard.edu/primerbank/">https://pga.mgh.harvard.edu/primerbank/</a>	N/A
LIMK2 qPCR FWD: GGATTCCCTCACCAACTGGTA REV:AGCCACCATAAAAGGCCCTG	<a href="https://pga.mgh.harvard.edu/primerbank/">https://pga.mgh.harvard.edu/primerbank/</a>	N/A
CPEB4 qPCR FWD: ACATCTAGCGCATCGTCTCTT REV:ACAACAGAGCACCGTTATTAGC	<a href="https://pga.mgh.harvard.edu/primerbank/">https://pga.mgh.harvard.edu/primerbank/</a>	N/A
LRRK2 qPCR FWD: GAGCACGCCTCCAAGTTATTT REV:ACTGGCATTATGAACTGTTAGCA	<a href="https://pga.mgh.harvard.edu/primerbank/">https://pga.mgh.harvard.edu/primerbank/</a>	N/A
GPR155 qPCR FWD: TTGCCTACAGCAGTAACGCAT REV:GGAAGTGCAAATCTGGAGACA	<a href="https://pga.mgh.harvard.edu/primerbank/">https://pga.mgh.harvard.edu/primerbank/</a>	N/A
CYP27A1 qPCR FWD: CGGCAACGGAGCTTAGAGG REV:GGCATAGCCTTGAACGAACAG	<a href="https://pga.mgh.harvard.edu/primerbank/">https://pga.mgh.harvard.edu/primerbank/</a>	N/A
IL-1B qPCR FWD: ATGATGGCTTATTACAGTGGCAA REV:GTCGGAGATTTCGTAGCTGGA	<a href="https://pga.mgh.harvard.edu/primerbank/">https://pga.mgh.harvard.edu/primerbank/</a>	N/A
P2RY12 qPCR FWD: CACTGCTCTACTGTCTGT REV:AGTGGTCTCTGTTCCAGTTTG	<a href="https://pga.mgh.harvard.edu/primerbank/">https://pga.mgh.harvard.edu/primerbank/</a>	N/A
<b>Recombinant DNA</b>		
pLX304 SMAD3	DNASU	HsCD00440766-SMAD3
pLX304 SMARCA4	DNASU	HsCD00861075-SMARCA4
pLX304 STAT3	DNASU	HsCD00443857-STAT3
pDONR221 SUZ12	DNASU	HsCD00832948-SUZ12
pLX304 TCF4	DNASU	HsCD00438170-TCF4
pLX304 ELF1	DNASU	HsCD00445051-ELF1
pLX304 ELF2	DNASU	HsCD00438947-ELF2
pLX304 ETV5	DNASU	HsCD00435257-ETV5
pLX304 ETV6	DNASU	HsCD00445584-ETV6
pLX304 FLI1	DNASU	HsCD00438298-FLI1
pLX304 IRF8	DNASU	HsCD00440187-IRF8
pLX304 SPI1	DNASU	HsCD00936456-SPI1
pLX304 ETS2	DNASU	HsCD00434239-ETS2
pLX304 CEBPD	DNASU	HsCD00852417-CEBPD
pLX304 CTBP2	DNASU	HsCD00435806-CTBP2
pLX304 CTNNB1	DNASU	HsCD00852530-CTNNB1
pLX304 ESR1	DNASU	HsCD00443651-ESR1
pLX304 FOXO3	DNASU	HsCD00446377-FOXO3

(Continued on next page)

**Continued**

REAGENT or RESOURCE	SOURCE	IDENTIFIER
pDONR221 JARID2	DNASU	HsCD00829788-JARID2
pLX304 LMO2	DNASU	HsCD00438767-LMO2
pLX304 MTF2	DNASU	HsCD00435376-MTF2
pLX304 NR3C1	DNASU	HsCD00445225-NR3C1
pLX304 PIAS1	DNASU	HsCD00443565-PIAS1
pLX304 PPARG	DNASU	HsCD00441631-PPARG
pDONR221 RUNX2	DNASU	HsCD00829534-RUNX2
pLX304 ARNT	DNASU	HsCD00442555-ARNT
pLX304	DNASU	EvNO00877063
pLV-mcherry	Addgene	Addgene #36084

**Software and algorithms**

CellRanger software v3.0.1	10x Genomics	<a href="https://www.10xgenomics.com/">https://www.10xgenomics.com/</a>
Seurat R package v.4.0.3	Hao et al. <sup>54</sup>	<a href="https://satijalab.org/seurat/">https://satijalab.org/seurat/</a>
propeller	Phipson et al. <sup>55</sup>	<a href="https://github.com/Oshlack/speckle">https://github.com/Oshlack/speckle</a>
DoubletFinder v2.0	McGinnis et al. <sup>56</sup>	<a href="https://github.com/chris-mcginnis-ucsf/DoubletFinder">https://github.com/chris-mcginnis-ucsf/DoubletFinder</a>
cellranger-atac software (v1.1.0)	10x Genomics	<a href="https://www.10xgenomics.com/">https://www.10xgenomics.com/</a>
ArchR (v1.0.1)	Granja et al. <sup>57</sup>	<a href="https://www.archproject.com/">https://www.archproject.com/</a>
MACS2	Zhang et al. <sup>58</sup>	<a href="https://github.com/macs3-project/MACS">https://github.com/macs3-project/MACS</a>
Homer	Heinz et al. <sup>59</sup>	<a href="http://homer.ucsd.edu/homer/motif/">http://homer.ucsd.edu/homer/motif/</a>
EnrichR Appyter	Kuleshov et al. <sup>60</sup>	<a href="https://maayanlab.cloud/Enrichr">https://maayanlab.cloud/Enrichr</a>
ComplexHeatmap	Gu et al. <sup>61,62</sup>	<a href="https://bioconductor.org/packages/release/bioc/html/ComplexHeatmap.html">https://bioconductor.org/packages/release/bioc/html/ComplexHeatmap.html</a>
IMARIS	Oxford Instruments	<a href="https://imaris.oxinst.com">https://imaris.oxinst.com</a>
Morpheus	Broad Institute	<a href="https://software.broadinstitute.org/morpheus/">https://software.broadinstitute.org/morpheus/</a>
Photoshop	Adobe Photoshop 2021	<a href="https://www.adobe.com">https://www.adobe.com</a>
QuPath (v0.4.3)	QuPath	<a href="https://qupath.github.io">https://qupath.github.io</a>
ImageJ	NIH	<a href="https://imagej.nih.gov/ij/">https://imagej.nih.gov/ij/</a>
GraphPad Prism	GraphPad Software	<a href="https://www.graphpad.com/">https://www.graphpad.com/</a>
MAGMA.Celltype	Skene et al. <sup>47</sup>	<a href="https://github.com/neurogenomics/MAGMA_Celltyping">https://github.com/neurogenomics/MAGMA_Celltyping</a>
R knockoff package	<a href="https://web.stanford.edu/group/candes/knockoffs/index.html">https://web.stanford.edu/group/candes/knockoffs/index.html</a>	<a href="https://cran.r-project.org/web/packages/knockoff/index.html">https://cran.r-project.org/web/packages/knockoff/index.html</a>
Cytoscape (v3.9.1)	The Cytoscape Consortium	<a href="https://cytoscape.org/">https://cytoscape.org/</a>

**Other**

Superfrost Plus Slides	Fisherbrand	Cat#12-550-15
40µm cell strainer	Corning	Cat#431750
Confocal microscope	Zeiss	Cat#LSM 900
Punch Kit 2.00 mm	UniCore	Cat# WHAWB100029
Cryostat	Leica	Cat#CM3050s
Automated Cell Counter	Invitrogen	Countess II
AggreWell 800	STEMCELL technologies	Cat#34815
Real-Time PCR	Bio-Rad	CFX96 Touch Real-Time PCR Detection System

**RESOURCE AVAILABILITY**

**Lead contact**

Further information and requests for resources and reagents should be directed to and will be fulfilled by the lead contact, Manolis Kellis ([manoli@mit.edu](mailto:manoli@mit.edu)).

### Materials availability

This study did not generate new unique reagents.

### Data and code availability

- Count matrices, metadata and supplementary data in this study from the ROSMAP cohort are at [http://compbio.mit.edu/microglia\\_states/](http://compbio.mit.edu/microglia_states/). ROSMAP data can be requested at this database: <https://www.synapse.org/#!Synapse:syn52293417>. Raw data and processed data for all iMGLs bulk RNA-seq and snRNA-seq in this study are publicly available in GEO database: GSE227223.
- The codes used in this study are available at <http://compbio.mit.edu/scMicroglia/>, <https://github.com/nasunmit/scMicroglia> and Zenodo: 829790, <https://doi.org/10.5281/zenodo.8297901>.
- Any additional information required to reanalyze the data reported in this paper is available from the [lead contact](#) upon request.

## EXPERIMENTAL MODEL AND SUBJECT DETAILS

### Human postmortem brain samples from ROSMAP

In this study we obtained human postmortem brain tissues from the Religious Orders Study and Rush Memory and Aging Project (ROSMAP, each approved by an Institutional Review Board of Rush University Medical Center). All participants signed an informed consent, an Anatomic Gift Act for organ donation, and a repository consent to allow the data to be shared.<sup>14</sup> We used seven pathological phenotypes for each individual to separate all individuals in this cohort into three groups which we defined as no AD pathology, low AD pathology and high AD pathology by performing a k-means clustering method on the quantitative matrix after Z score normalization. These include pathological phenotypes, e.g., a global AD pathology, molecularly specific amyloid- $\beta$  and tangles, and global cognition proximate to death. Thus, case status was based on both AD pathology and cognition pathology, and other variables were allowed to freely associate, as previously reported.<sup>63–67</sup> We acknowledge that this empirical approach to casesness does not conform to standard diagnostic criteria.

We performed snRNA-seq in the prefrontal cortex for 423 individuals, and four other regions for a subset of 48 individuals, including mid-temporal cortex, angular gyrus, entorhinal cortex, thalamus, and hippocampus for a subset of 65 individuals and an additional 21 individuals (Table S1, page 1). We performed snATAC-seq in the prefrontal cortex for a subset of 92 individuals, and five other regions for a subset of 48 individuals, including mid-temporal cortex, angular gyrus, entorhinal cortex, thalamus, and hippocampus (Table S1, page 7).

### Culture of iPSC lines

AICS-0090-391 iPSCs, acquired via the Allen Institute for Cell Science <https://www.allencell.org>, were maintained on Matrigel-coated plates (Corning; Cat # 354277) with 5% CO<sub>2</sub> at 37°C in feeder-free conditions in mTeSR1 media (STEMCELL Technologies; Cat #85850). iPSCs were passaged when 60–80% confluent using ReLeSR (STEMCELL Technologies; Cat# 05872) and reseeded 1:6 onto Matrigel-coated plates.

## METHOD DETAILS

### Nuclei isolation from frozen postmortem brain tissue, snRNA-seq and snATAC-seq

We isolated nuclei from frozen postmortem brain tissue as previously described (Mathys et al., Nature 2019)<sup>11</sup> with some modifications. Briefly, we homogenized the brain tissue in 700  $\mu$ L Homogenization buffer and filtered the homogenate through a 40  $\mu$ m cell strainer (Corning, NY), added 450  $\mu$ L Working solution and loaded it as a 25% OptiPrep solution on top of a 30%/40% OptiPrep density gradient (750  $\mu$ L 30% OptiPrep solution, 300  $\mu$ L 40% OptiPrep solution). We separated the nuclei by centrifugation using a fixed rotor, tabletop centrifuge (5 min, 1000g, 4°C). We collected the nuclei pellet at the 30%/40% interphase, transferred it on a new tube, washed it twice with 1 mL ice-cold PBS containing 0.04% BSA (centrifuged 3 min, 300g, 4°C) and finally resuspended it in 100  $\mu$ L PBS containing 0.04% BSA. After counting, we diluted the nuclei to a concentration of 1000 nuclei per  $\mu$ L. We used the isolated nuclei for the droplet-based 10x scRNA-seq assay, targeting 5000 nuclei per brain region and individual, and prepared libraries using the Chromium Single-Cell 3' Reagent Kits v3 (10x Genomics, Pleasanton, CA) according to the manufacturer's protocol. We sequenced pooled libraries using the NovaSeq 6000 S2 sequencing kits (100 cycles, Illumina). For the snATAC profiling, we spun down the remaining nuclei, resuspended them in 1x Diluted Nuclei buffer and adjusted their concentration to 2500 nuclei per  $\mu$ L. We proceeded with library construction targeting 5000 nuclei per brain region and individual using the Chromium Single-Cell ATAC Reagent Kit v1 (10x Genomics, Pleasanton, CA) following the manufacturer's protocol. We sequenced the pooled libraries using the NovaSeq 6000 S2 sequencing kits (100 cycles, Illumina).

### snRNA-seq data processing

We mapped the raw reads to human reference genome version GRCh38 and quantified unique molecular identifiers (UMIs) counts for each gene in each cell using CellRanger software v3.0.1 (10x Genomics).<sup>68</sup> We pre-processed this count matrix (gene-cell) using the Seurat R package v.4.0.3<sup>54</sup>. We kept the cells with more than 500 UMIs and less than 5% mitochondrial genes, and genes with expression at least in 50 cells for further analysis. We normalized the counts by the total UMI counts for each cell, multiplied by



10,000, and then log-transformed. We used the top 2000 highly variable genes for principal component analysis (PCA) and the top 30 principal components (PCs) as inputs to perform UMAP. We used Harmony for batch correction.<sup>69</sup> We used the resolution as 0.5 to identify clusters. We used DoubletFinder to estimate the potential doublets formed by two or more cells based on the by default parameters.<sup>56</sup> The cells with high doublet scores (0.2 as cutoff) were removed for further analysis. After generating clusters, one cluster showing high expression of markers of two or more cell types was also treated as doublets and removed for further analysis.

### snATAC-seq data processing

We processed snATAC-seq data using the same computational pipeline as Xiong et al.<sup>21</sup> accompanied manuscript. Specifically, we firstly generated raw data of FASTQ for each sample by demultiplexing the reads with cellranger-atac software (v1.1.0),<sup>70</sup> and then mapped the reads to human reference genome version GRCh38 using “cellranger-atac count” to obtain the fragment file for each sample. We processed the snATAC-seq data using ArchR (v1.0.1).<sup>57</sup> We removed the potential doublets using the “filterDoublets” function in ArchR. We kept the cells with TSS enrichment more than 6 and the number of fragments between 1000 and 100,000 for further analysis. We performed Iterative LSI dimension reduction and clustering using the matrix of 500 bp tile-based, with parameters “iterations = 4, resolution = 0.2, varFeat = 50000”. The UMAP was used to visualize cell embedding for all cells. We generated the gene score matrix using ArchR, and annotated the cell type for each cluster based on the gene score of well-known markers in the brain.<sup>11</sup> We integrated the clusters that were annotated as microglia/immune cells for further analysis.

### In silico sorting to enrich immune cells and cell type annotation in snRNA-seq data

For the full datasets with all cell types (2.8 million cells), we first annotated the cell type for each cluster based on three widely-used canonical markers of major cell types in the brain (including excitatory and inhibitory neurons, astrocytes, oligodendrocytes, OPCs, microglia and vascular cells)<sup>11</sup> and a list of markers for immune cells.<sup>11,71</sup> We also tested the enrichment of a large set of markers<sup>72</sup> in highly expressed genes for each cluster to confirm the annotation based on several marker genes. We next calculated the cell type scores (i.e., astrocyte, oligodendrocyte, microglia, etc) for each cell, which were represented by the average expression of a group of markers for each cell type.<sup>72</sup> The cells were then selected as microglia/immune cells for further integrative analysis if and only if (1) the clusters that the cells belong to were annotated as microglia/immune cells; and (2) the cells had the highest score for microglia/immune cells, and (3) the score for microglia/immune cells was 2-fold higher than the second highest score. For the selected microglia/immune cells, we followed the same pipeline to perform dimensional reduction and clustering with the same parameters as full datasets. We used the Wilcoxon rank-sum test in Seurat with customized parameters (min.pct = 0.25, logfc.threshold = 0.25) to identify highly expressed genes for each cluster compared to all cells from other clusters.

### Cell proportional analysis

We performed propeller<sup>55</sup> analysis to evaluate the statistical significance for compositional differences between phenotypic groups of interest (AD groups, age, and sex group) with the consideration of the confounding variables in the model. We used *speckle* package in R and adjusted p value <0.05 as cutoff for significance.

### Microglia epigenetic state annotation

For the cells that were annotated as microglia in snATAC-seq data, we re-performed Iterative LSI dimension reduction and clustering using the parameters “iterations = 4, resolution = 0.5, varFeat = 50000” to identify the subtypes of microglia, which were defined as epigenomic states in further analysis. We removed the clusters with less than 1,000 cells and identified the marker genes based on the gene scores (aggregation of snATAC signals around promoter regions). We used these marker genes to annotate the three epigenetic states as one HOM due to lack of activated genes, and two activated states with high gene scores of activation genes.

### Peak calling and differential peak analysis

We used MACS2 to call chromatin accessible peaks based on the pipeline in ArchR,<sup>57,58</sup> generated peak matrix (peak X cell matrix) and identified marker peaks for each epigenomic in account for difference in data quality among the cell groups by considering TSS enrichment and the number of unique fragments per cell. We used a Wilcoxon test in ArchR to evaluate if the peak was differential between epigenomic states of microglia (cutoff: p.value <0.01 and log2FoldChange >0.5). We performed GREAT analysis to annotate the differential peaks in each state<sup>73</sup> with the setup as basalPlusExt and 100kb for both upstream and downstream genomic regions. We used Homer to perform motif analysis by expanding the peaks to 2000bp with the default parameters.<sup>59</sup>

### Co-accessibility analysis

We identified the co-accessibility between proximal and distal peaks, as the proxy of peak-to-gene links to look for the correlations between peak accessibility and gene expression. The parameters we used included corCutOff = 0.3, FDR = 1e-4, upstream = 50000, and downstream = 50000. The pairs of peaks and genes were used for further analysis to associate distal accessible peaks with microglial transactional state signature genes and the differential expression genes in AD.

### Identification of differentially expressed genes in AD progression

We applied three methods (two single-cell based methods, regular MAST and MAST with random effect, and a single-cell based method edgeR) to detect the differentially expressed genes for each microglia transcriptional state between control and low AD pathology individuals, and low AD pathology and high AD pathology individuals. We controlled the covariates for all three methods, including number of expressed genes, percentage of mitochondrial genes, percentage of ribosomal genes, age, sex, PMI, race, batch, brain region, and other dementia related pathology and diagnosis (Lewy body dementia and Parkinson's disease). The genes with  $FDR \leq 0.05$  and absolute coefficient  $\geq 0.1$  for MAST and MAST with random effect or absolute  $\log_2$  FoldChange  $\geq 0.58$  (corresponding to fold change  $\geq 1.5$ ) for edgeR were selected for pairwise comparison between these three methods. We then tested if the DEGs identified by each two methods were significantly overlapped (measured by Fisher's exact test with all expressed genes as background and adjusted p value  $< 0.05$  as cutoff) and the percentage of overlapping (measured by Jaccard score). We found the DEGs were highly consistent between three methods. We then kept DEGs which were detected as DEGs in at least two methods for further analysis. We classified these DEGs into three categories based on the cell-state-specificity and effect direction to AD progression, which could be further classified into 51 gene groups as shown in [Figure S8](#).

### Comparison with public datasets

We downloaded the marker genes of microglial subtypes described in Olah et al.<sup>12</sup> and compared them with the marker genes of microglial states in this study by computing the Jaccard score pairwise and testing the significance of overlapping with Fisher's exact test. The Jaccard score and significance were visualized by heatmap shown in [Figure S1](#). We also downloaded the marker genes of microglial subtypes in mouse data provided by Hammond et al.<sup>4</sup> and performed a similar analysis to compare human and mouse microglia subtypes. We evaluated the adDEGs by comparing with DEGs identified by Gerrits et al.<sup>9</sup> We used Jaccard score to represent the percentage of overlapping genes and Fisher's exact test to measure the statistical significance ( $FDR \leq 0.05$ ).

### Prediction of upstream transcription factors

For enrichment-based analysis, we predicted the upstream TFs of genes (marker genes or DEGs) using Enrichr in R based on three libraries including TRANSFAC and JASPAR, ChEA, and ENCODE TF ChIP-seq data.<sup>24,60,74</sup> We used adjusted p value  $< 0.05$  as a cutoff to select the significant TFs. For motif-based analysis, we linked the microglial state marker genes to distal peaks using the peak-to-gene links represented by co-accessible peaks and then performed motif analysis by expanding the peaks to 2000bp with the default parameters in Homer.<sup>59</sup> We kept the TFs with detected expression (average expression  $> 1$  after  $\log_2$  transformation) in microglia for further analysis. We also applied DoRothEA to predict differentially activated TFs in each microglial state based on the activity score of TFs.<sup>33</sup> Fold change  $> 1.5$  and p value  $< 0.01$  were used as cutoffs to select highly activated TFs for each microglial state in DoRothEA analysis. To compare the TFs identified by enrichment/motif based method and DoRothEA, we calculated the Jaccard score to represent the percentage of overlapping and performed Fisher's exact test to evaluate the statistical significance ( $FDR < 0.05$  as a cutoff and all expressed TFs as background).

These upstream TFs may or may not be highly and specifically expressed by the microglial states that they regulate. To evaluate the upstream TFs were highly expressed in which microglial state, we checked the upstream TFs for each state and counted which of those TFs had high expression in all states. We then normalized that number by the total number of TFs that are marker genes in each state. We next defined a score by normalizing the sum of the values obtained in the previous step as one, represented as the potential of state-state transition. We performed a permutation test to evaluate whether the score is statistically significant for each pair of states with transition potential. Specifically, we randomly selected the same number of TFs as the enriched TFs for each state from the full database, performed the same analysis as above, and compared the score with the real score to obtain p values (permutation times: 1000). The result was visualized by the heatmap ([Figure S6J](#)), showing the score by color and significance by star. A model of transitions between MG8, MG10 and MG0 is shown in [Figure 4L](#).

### Immunohistochemistry staining

Fixed human brain tissue (prefrontal cortex) was sectioned using a vibratome at 40  $\mu\text{m}$ . The sections were blocked for 1 h at room temperature (RT) in blocking buffer (PBS containing 5% bovine serum albumin, 1% normal donkey serum and 0.3% Triton X-100). The sections were incubated for 48 h at 4°C with the primary antibodies in blocking buffer. A list of all primary antibodies can be found in [Table S1](#), page 4. Following primary antibody incubation, the sections were washed three times for 5 min each at RT in PBS and then incubated with secondary antibodies (dilution 1:1000) for 2 h at RT. The slices were once again washed three times at RT in PBS and incubated in TrueBlack (Biotium; Cat#23007) for 90 s. After a final round of washes, the slices were mounted on Superfrost Plus Slides (Fisherbrand; Cat#12-550-15) in Fluoromount-G (SouthernBiotech; Cat#0100-01). Primary antibodies were visualized with Alexa Fluor 405, Alexa Fluor 488, Alexa Fluor 555, and Alexa Fluor 647 antibodies (Molecular Probes), and cell nuclei visualized with Hoechst 33342 (Sigma-Aldrich; Cat#94403) using a confocal microscope (LSM 900; Zeiss) with a 20 $\times$  or 63 $\times$  objective. For experiments quantifying fluorescent intensity, images were analyzed with Imaris imaging software (Oxford Instruments) for 3D reconstruction of IBA1 surfaces. Mean intensity values for each channel within IBA surfaces were quantified. For inflammatory state marker expression in multiplexed immunostaining experiments, values for each marker were visualized by creating expression gradients for each channel and superimposed onto IBA-positive surfaces using Imaris visualization tools, as presented in [Figure S5B](#). For

quantification, this data was z-scored across cells and plotted as a heatmap clustered by hierarchical clustering with Morpheus (<https://software.broadinstitute.org/morpheus/>).

### RNAscope and HiPlex

Tissue blocks from the prefrontal cortex were cored into a 2mm disc with a disposable biopsy punch (UniCore Punch Kit 2.00 mm) and frozen in OCT for cryosectioning at 12µm thickness on the cryostat (Leica CM3050S). Sections were directly mounted on Superfrost Plus Slides (Fisherbrand; Cat#12-550-15) and allowed to dry at –20 celsius for 1 to 2 h. Tissue was then processed following the recommended protocol by ACD Biotechne RNAscope assays. To quench autofluorescence, we applied TrueBlack (Biotium; Cat#23007) for 90 s after the final step (DAPI application) of the RNAscope assay procedure, and gently rinsed with PBS prior to coverslipping and imaging. For HiPlex multiplexing, we reapplied DAPI and TrueBlack at the end of every round. 12x12 tile scans with 12z steps were acquired with a confocal microscope (LSM 900; Zeiss) with 63x oil immersion objective. Maximum projection images were manually aligned on Photoshop (Adobe Photoshop 2021) with DAPI nuclei stain and tissue boundaries serving as guides for registration. Microglia were then identified based on probe detection for *P2RY12*, *IBA1* and *CX3CR1* probes were weakly detected and were used as confirmation probes. After manually assigning nuclei as microglia (greater than *P2RY12* dots with co-detection of *IBA1* and *CX3CR1*), images containing microglia were further processed with QuPath (v0.4.3) for probe quantification. Manual curation of images were performed to ensure accurate probe detection by an investigator blind to the sample group. The distribution of dot numbers varied greatly by probes. For example, while *CPEB4* probe detected 0–30+ dots per nuclei, *RELB* probe detected 0–9+ dots. To infer expression enrichment, the number of dots were Z-scored per probe across all samples.

### Microglia induction protocol

Embryoid bodies (EBs) were generated following an adapted iPSC seeding strategy (Marton et al., 2019) with a previously established protocol (Sloan et al., 2018). 60–80% confluent iPSCs were incubated in ReLeSR (STEMCELL Technologies; Cat# 05872) for 1 min at RT, followed by a 3-min dry incubation at 37°C. iPSC colonies were then scraped in mTeSR1 media (STEMCELL Technologies; Cat # 85850) and dissociated into a single-cell suspension through pipetting. After centrifugation at 300g for 5 min, the cell pellet was resuspended in 2 mL of mTeSR1 media supplemented with ROCK inhibitor (1:1000) (BioVision; Cat# 2342-5) and counted with a Countess II automated cell counter. 5 x 10<sup>6</sup> cells were then plated into each well of an AggreWell plate (STEMCELL Technologies; Cat# 34815) for EB induction. After 48 h, 15–30 EBs were moved onto each well of Matrigel-coated plates (Corning; Cat # 354277). Using the STEMdiff Hematopoietic Kit (STEMCELL Technologies; Cat#05310), EBs were differentiated into hematopoietic progenitor cells (HPCs). After collection and centrifugation at 300g for 5 min, nonadherent HPCs were resuspended in 1 mL of microglia differentiation media (MDM) (1:1 DMEM/F12 (Thermo Fisher Scientific; Cat#11330-057); Neurobasal media (Gibco; Cat# 21103049) supplemented with IL-34 (PeproTech; Cat#200-34) and *m*-CSF (PeproTech; Cat#300-25) as described (McQuade et al., 2018). Cells were plated at 200,000 cells per well in 6-well tissue culture plates and maintained in MDM with 5% CO<sub>2</sub> at 37°C for at least two weeks before experiments.

### CRISPRi in iMGLs for MG10 transcription factor repression

dCAS9-KRAB-BFP (CRISPRi) iPS line was acquired from Allen Institute for Cell Science ([allencell.org](http://allencell.org)). Duplicate sgRNAs per target were synthesized following the protocol from Precision sgRNA Synthesis Kit (ThermoFisher #A29377) from guide RNA sequences for FOXO3, HIF1A and FOXP3 taken from libraries derived by (Horlbeck et al., 2016 eLife). HIF1A\_1: GCTGGCCGAAGCGACGAAGA HIF1A\_2: GCCTCCTGTCCCCTCAGACG; FOXP2\_1: GAAGCCGGGAGACCAGACAC FOXP2\_2: GAATCAGCATTTAATCACTA; FOXO3\_1: GGAGGGGAAAGGGAAGCGCC FOXO3\_2: GTGGCGCGCGCAGCTGAC. iMGLs were differentiated from CRISPRi iPSCs following the microglial induction protocol above and a cocktail with mixed sgRNAs delivered to iMGLs via lipofectamine CRISPRMAX (Invitrogen #CMA00003). Following 4 h post sgRNA transfection, cells were exposed to 10 ng/ml of LPS overnight. Control iMGLs were mock transfected (no sgRNAs in lipofectamine) but also exposed to LPS. Cells were processed for snRNA-seq following our nuclei isolation protocol detailed below.

### Nuclei isolation from iMGLs for snRNA-Seq

Nuclei from iMGLs were isolated using the Nuclei Isolation Kit: Nuclei EZ Prep (Cat#NUC101, Sigma-Aldrich) per manufacturer's instructions. In brief, microglia were washed with cold PBS and lysed in Nuclei EZ Lysis Buffer with RNase Inhibitor (0.2 U/ul) in well by scraping. Lysate was collected, briefly vortexed and incubated on ice for 5 min. Nuclei were collected by centrifuging at 500 x g for 5 min at 4°C. Following a subsequent wash in lysis buffer, nuclei were resuspended in 200 µL Nuclei EZ storage buffer and counted. Fresh nuclei were diluted to a concentration of 800–1200 cells/ul, and approximately 17,400 cells per channel for an estimated recovery of 10,000 cells per channel. SnRNA-seq libraries were generated from fresh nuclei with the Chromium Next GEM Single Cell 3' Reagent Kit v3.1 (10X Genomics) in accordance with the manufacturer's instructions.

### Calcium imaging

Microglia were plated in 48-well tissue-culture treated plates and cultured for 5 days. For ATP uncaging experiments in the presence of an inflammatory stimulus, cells were incubated overnight with LPS (10 ng/mL). The day of imaging, microglia were pre-incubated with 1 mM DMNPE- Caged ATP (Cat# 1049; Fisher Scientific) and 1 mM Fluo-4 a.m. (Cat#F14201; Thermo Fisher Scientific) at 37°C for 30–45 min. In experiments where iMGLs were exposed to spheroid CM, iMGLs were half-fed with CM for 2 h before recording

session. Live-cell imaging was performed using Zeiss LSM900 at 37°C and 5% CO<sub>2</sub>. All images were acquired at 488 nm. Uncaging of ATP was done at 405 nm for 30 s post-baseline acquisition, followed immediately by post-stimulation image acquisition. Images were first stabilized to account for drift in the x-y direction; we used the ImageJ plugin “Linear Stack Alignment with SIFT”. Calcium traces from motion-corrected time series were manually segmented on ImageJ into individual cells based on threshold intensity, variance, and upper and lower limits for cell size. Image segmentation results were separately inspected for quality control. Fluorescence signal time series (DF/F: change in fluorescence divided by baseline fluorescence) were calculated for each segment. The baseline fluorescence for each cell was determined as the minimum fluorescence signal in the baseline recording epoch. Data was plotted from individual cells in one experiment, although the experiments were repeated at least three times. Heatmaps were generated using GraphPad Prism (GraphPad Software)

### Transcriptional time point analysis following inflammatory stimulation

In order to evaluate the temporal transcriptional response of targeted DEGs within the MG2, MG8, and MG10 inflammatory clusters, microglia were plated onto 12-well tissue-culture treated plates and cultured for 5 days. Microglia were stimulated with TNF $\alpha$  (40 ng/mL), INF $\gamma$  (30 ng/mL), or LPS (10 ng/mL) for 1 h, washed 3 times with D-PBS, and left to incubate in culture media. A subset (n = 3 per condition) of untreated microglia were collected for baseline measurements. At each timepoint (1h, 6h, 24h, 120h), microglia were pelleted for RNA extraction and subsequent analysis by Real-Time PCR (qPCR). RNA extraction of iMGLs was achieved with RNeasy Plus Mini Kit (Cat#74134; Qiagen) and reverse transcription was performed with RNA to cDNA EcoDry Premix (Cat#639549; Takara) according to the manufacturer’s instructions. Gene expression was analyzed with Real-Time PCR (CFX96; Bio-Rad) and SsoFast EvaGreen Supermix (Cat#1725202; Bio-Rad). Expression data was normalized to housekeeping gene GAPDH using the  $2^{-\Delta\Delta C_t}$  relative quantification method. A list of qPCR primers used in this study can be found. For assessment of amyloid-induced transcriptional changes, iMGLs seeded onto 6-well tissue-culture treated plates were exposed to 2 $\mu$ g of pre-formed amyloid beta (1–42) fibrils (rPeptide #AF-1002-1) per well. Baseline controls were untreated but harvested at the same time point as 4 h after amyloid seeding. 3 wells per time point were harvested, pelleted and flash-frozen. After all time points were collected, pellets were processed for RNA extraction following RNeasy Plus Mini Kit (Cat#74134; Qiagen) and processed for Bulk RNA-seq at the MIT BioMicro Center.

### Homeostatic transcription factor overexpression: Plasmid cloning, lentivirus production and homeostatic assessment

To screen the overexpression of TFs from MG0, lentivirus constructs were purchased from the DNASU Plasmid Repository (Tempe, AZ). Majority of the 25 TFs (22 of them) utilized were obtained in the lentiviral vector, pLX304. The remaining 3 TFs (SUZ12, JARID2, RUNX2) were obtained in pDONR221 format and subsequently subcloned into pLX304 for lentiviral production and overexpression experiments. An empty pLX304 plasmid was used as a control. A list of all the vectors used in this study can be found in [Table S1](#), page 8. The empty and TF-containing plasmids were then transfected into HEK-293T cell line (Cat#CRL-3216; ATCC) with lentiviral packaging and envelope vectors to generate lentivirus following the previously published protocol.<sup>75</sup> Lentiviral supernatant was collected 48 h after transfection and centrifuged for 2 h by ultracentrifugation at 25,000 RPM at 4°C. Pellets were resuspended in DPBS and frozen at –80°C until used. For overexpression experiments, lentivirus was top-loaded and allowed to incubate overnight in microglia that had been re-plated onto multi-well plates and cultured for 8 days. Calcium imaging was performed as described above but cells were pre-incubated with CM from forebrain organoid cultures for 2 h, a procedure established to yield strong calcium transients in iMGLs in a neuronal-activity dependent manner from our previous study.<sup>35</sup> For microglial morphology analysis, cells were fixed and permeabilized following standard lab protocols after 10 days of TF overexpression and stained with ActinGreen 488 Readyprobes (Invitrogen #R37110). Imaging was performed with LSM 900 confocal microscope and 3D reconstruction of cell surfaces were achieved through Imapris imaging analyses (Oxford Instruments) for sphericity counts. Control iMGLs were infected with lentivirus containing an empty mCherry backbone.

### Gene Ontology enrichment analysis

We used Enrichr in R to perform enrichment analysis for Gene Ontology biological process (adjusted p value <0.05 as a cutoff).<sup>76,77</sup> We selected the representative terms for visualization using heatmap manually based on the diverse functional categories and the number of genes involved in each term.

### Gene-level enrichment in GWAS signal by MAGMA

We applied MAGMA.Celltype, an R package, to test which microglial states can explain the heritability signal from GWAS summary statistics. We tested 14 traits<sup>78</sup>: AD,<sup>44</sup> lupus,<sup>79</sup> ulcerative colitis,<sup>80</sup> Crohn’s disease,<sup>80</sup> BMI,<sup>81</sup> triglycerides,<sup>82</sup> rheumatoid arthritis,<sup>83</sup> depressive symptoms,<sup>84</sup> ever smoked,<sup>85</sup> schizophrenia,<sup>86</sup> multiple sclerosis,<sup>87</sup> type 2 diabetes,<sup>88</sup> neuroticism,<sup>84</sup> years of education.<sup>84</sup> We used p value <0.05 or FDR <0.05 as cutoffs to define the weak or strong significant microglial states associated with GWAS signal.

### Expression and changes of AD-risk genes

We downloaded GWAS associated genes based on GWAS catalog annotation<sup>48</sup> for AD. We defined the GWAS associated genes in AD as AD-risk genes. The p value <10e-8 and <10e-5 were used as thresholds to select AD-risk genes for analysis.

### Microglia sc-eQTLs analysis

For microglia sc-eQTLs analysis, we firstly estimated the average expression for each gene using a poisson-gamma model with a cell-level sequencing depth parameter and an individual-level mean parameter for each gene within each individual. The mean parameter was estimated by an integrative variational inference algorithm.<sup>89</sup> We then estimated the confounding factors on the individual-level gene expression matrix in an adaptive way. For each gene, we defined control genes by taking the top most correlated genes located in different chromosomes. We performed principal component analysis (PCA) and used the top 50 PCs as covariates.

We next built knock-off filters<sup>90</sup> for a genotype dosage matrix (0, 1, 2 effect allele count) sampled from a *cis*-window (1Mb around the gene body) for each gene. We estimated PCs of the sampled genotype matrix by conducting singular value decomposition. Using the first factors that account for the >80% of total genetic variation, we estimated structured confounding factors that capture the dependency structures across individuals and genetic variants. We estimated the knock-off design matrix following scalable approaches that have been previously reported.<sup>91–93</sup>

We then performed multivariate analysis for each gene by regressing the pseudobulk profiles on the observed and knock-off genotype matrix, respectively. We performed a Bayesian spike-and-slab regression prior to measure the posterior inclusion probability (PIP) of each variant. The difference between PIP values on the observed variable and the knockoff counterpart were used to construct knock-off statistics. We determined the threshold for a desired false discovery rate level using the R knockoff package.<sup>94</sup>

### TWAS analysis

We performed transcriptome-wide association studies (TWAS)<sup>95,96</sup> within each LD block independently, and included all the genes whose *cis*-eQTL variants are located in that block. We used LD blocks previously defined based on the 1000 genomes project.<sup>97</sup> For each LD block, we first estimated AD-risk variation by projecting AD GWAS summary statistics onto the in-sample genotype matrix.<sup>98,99</sup> We also predicted the expression value of each gene directly regulated by *cis*-regulatory variants based on the results of our eQTL analysis. Since 10–100 genes are located within each LD block, we conducted a multivariate regression analysis to identify the most relevant genes and cell types associated with the predicted AD effects. We also calculated gene-by-gene statistics. If the same gene appears multiple times across different LD blocks, we assign genes to the block showing the strongest effect.

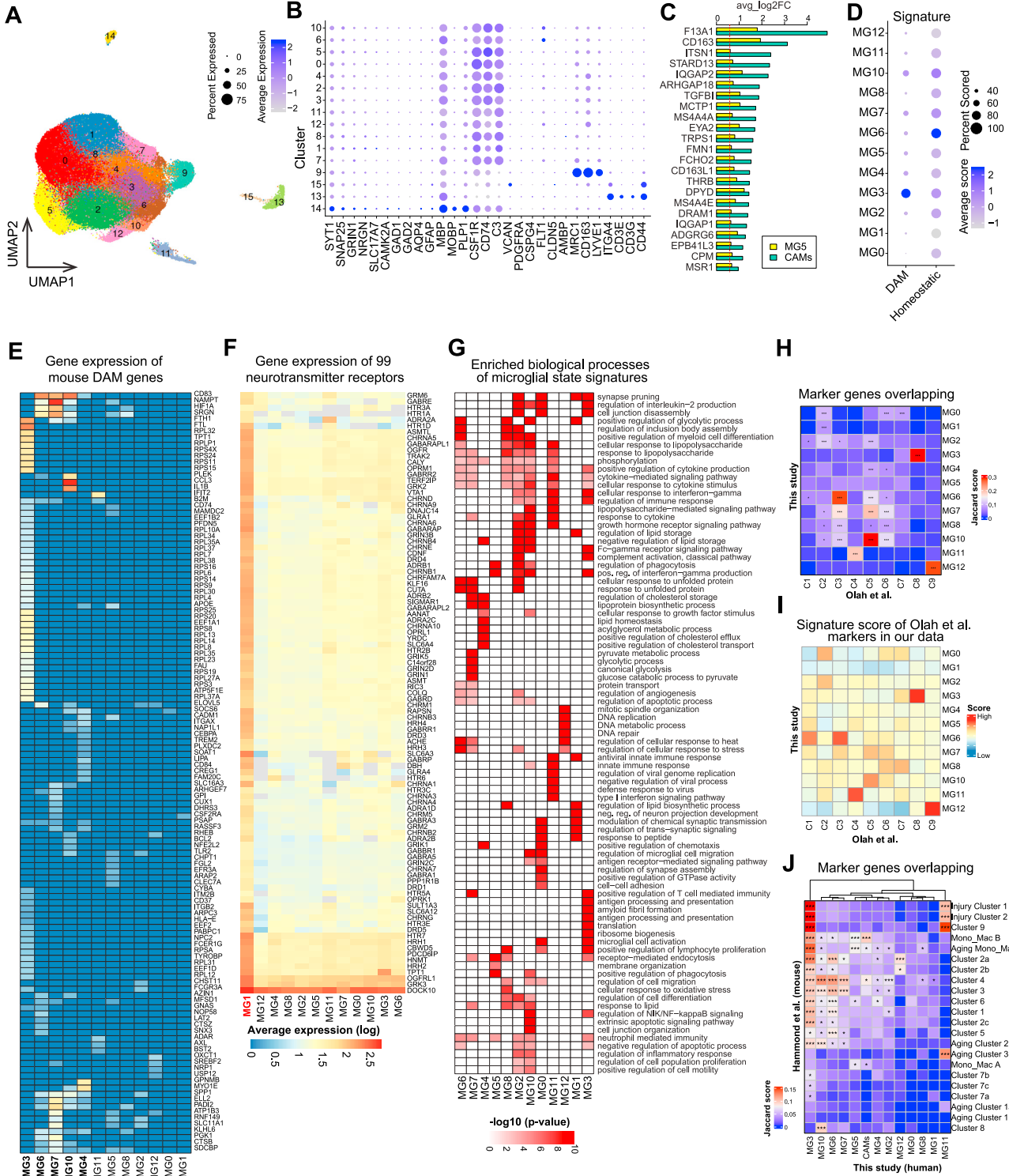
### Co-expression network analysis

We calculated the Pearson correlation coefficient between each pair of genes (including AD-risk genes, TWAS genes, and upstream TFs) across the individuals (early response: individuals with no or low AD pathology, late response: individuals with low or high AD pathology) at the individual level to measure the co-expression (p value <0.01 in *cor.test* in R). We aggregated the correlated gene pairs if they appeared in multiple microglia states and comparisons (early/late) and used the occurrence times as weight of the edge shown in the network. We used Cytoscape (v3.9.1) to visualize the co-expression network.<sup>100</sup>

## QUANTIFICATION AND STATISTICAL ANALYSIS

Statistical analyses for experimental validation were performed in GraphPad Prism using a two-tailed Student's *t* test or a one-way ANOVA followed by a post hoc Tukey's test with \**p* < 0.05 considered significant. Multiple comparisons were corrected with the Dunnett method as described in the figure legends. Studies were performed blindly and automated whenever possible with IMARIS or ImageJ cell, and multiple investigators confirmed quantification results. Data in graphs are expressed as mean, and error bars represent the standard error of the mean (SEM). For computational data analysis, Wilcoxon rank-sum test was used for calling differentially expressed genes and differentially accessible peaks. Pearson correlation was used for peak-to-gene links and co-expression network analysis. MAST and edgeR were used for identifying differentially expressed genes between phenotypic groups. Fisher's exact test was used to evaluate the significance of overlapping genes between two gene sets. Multiple comparisons were corrected by *fdr*.

# Supplemental figures

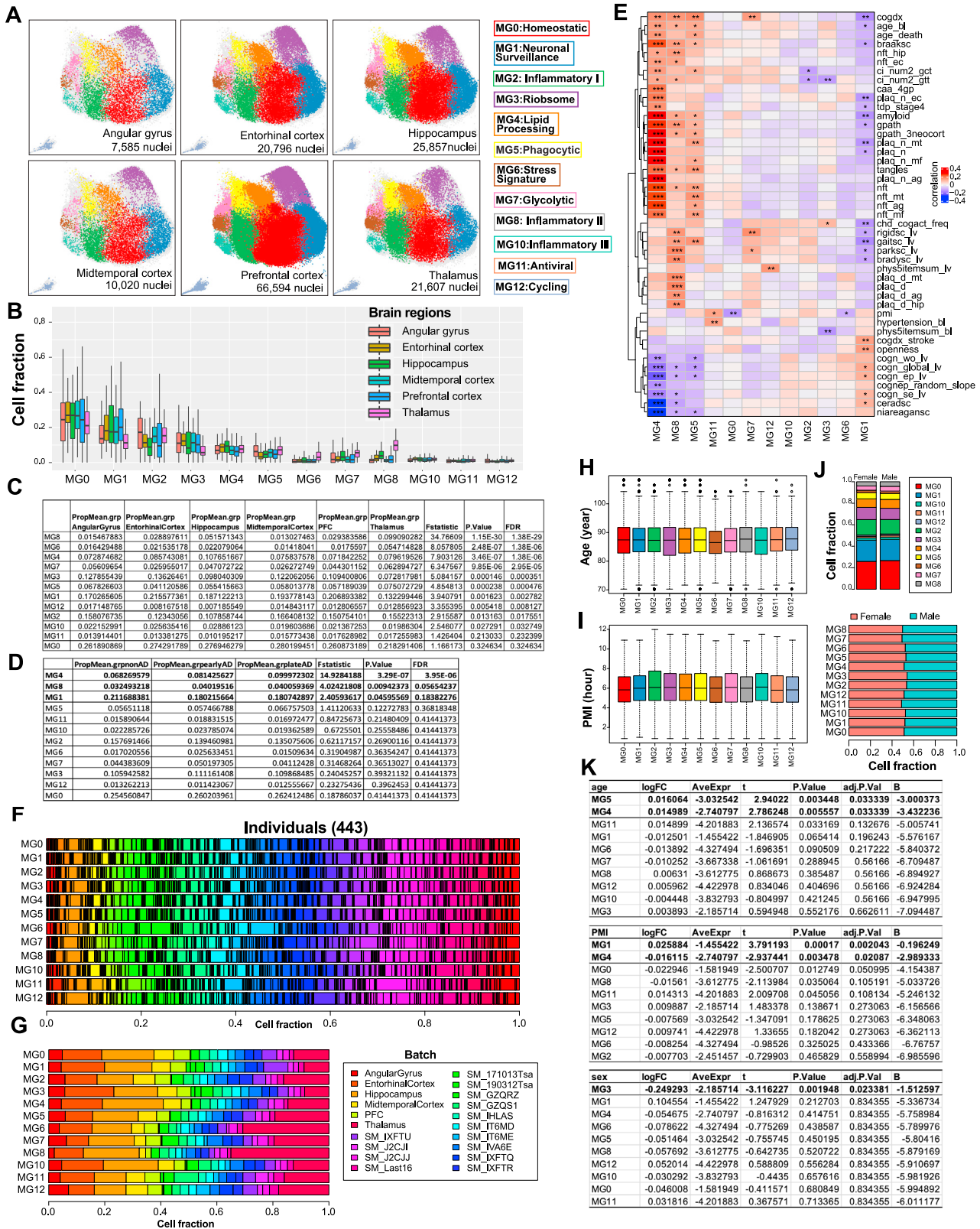


(legend on next page)

---

**Figure S1. Microglial transcriptional states in aged human brains, related to Figure 1**

- (A) UMAP of 174,420 *in silico* sorted immune nuclei from human postmortem brain tissues labeled 16 clusters in snRNA-seq data.
- (B) Expression patterns of canonical markers of brain cell types and immune cell types. The size of dots represents the percentage of cells with expression. The color of dots represents the scaled average expression level.
- (C) Average of log<sub>2</sub>foldchange of 23 MG5 and C9 shared marker genes. The red dashed line shows the threshold (fold change > 1.5).
- (D) Dot plot to show the signature score of DAM and homeostatic genes in each microglial transcriptional state shown in Figure 1A.
- (E) Heatmap to show the expression of DAM genes in each microglial state. The average expression in each state after log transformation is shown in the heatmap.
- (F) Expression levels of neurotransmitter receptors in 12 microglial states. The average expression in each state after log transformation is shown in the heatmap.
- (G) Representative enriched Gene Ontology biological processes in each microglial transcriptional state. Enrichr in R was used to perform GO enrichment (adjusted p value < 0.05 as cutoff).
- (H) Heatmap to show the significant overlap of marker genes between Olah et al. and this study. Jaccard score represents the percentage of pairwise overlapping genes. Fisher's exact test is used to evaluate the significance of overlapping (adjusted p value < 0.05 as a cutoff).
- (I) Heatmap to show the signature score of marker genes identified in Olah et al. in each microglial state of this study. The signature score is estimated by the average expression level of marker genes.
- (J) Heatmap to show the significant overlap of marker genes between Hammond et al. (mouse) and this study (human). Jaccard score represents the percentage of pairwise overlapping genes. Fisher's exact test is used to evaluate the significance of overlapping (adjusted p value < 0.05 as a cutoff).





---

**Figure S2. Cell abundance across multiple variables, related to Figure 1**

- (A) UMAP of microglia nuclei for each brain region. The number of cells in each cell type is shown.
- (B) Distribution of cell fraction across six brain regions in major cell types.
- (C) Statistical testing summary for comparison between regions by propeller in R.
- (D) Statistical testing summary for comparison between non-AD, early AD, and late AD by propeller in R.
- (E) Heatmap to show the correlation between cell fraction and quantitative pathological variable in each microglial transcriptional state. The Pearson correlation coefficient (PCC) is calculated and tested by `cor.test` in R to measure significance. The PCC values are shown in the heatmap. The significant levels are represented by stars (\*p value < 0.05, \*\*p value < 0.01, and \*\*\*p value < 0.001).
- (F) Distribution of cell fraction across all individuals in each microglial state.
- (G) Distribution of cell fraction across sequencing batches in each microglial state.
- (H–I) Distribution of ages/PMIs of the individuals across 12 microglial states.
- (J) Cell fraction across sex for each microglial state (bottom) and across cell types for male and female individuals (top).
- (K) Statistical testing summary for comparison in age, PMI, and sex by propeller in R.

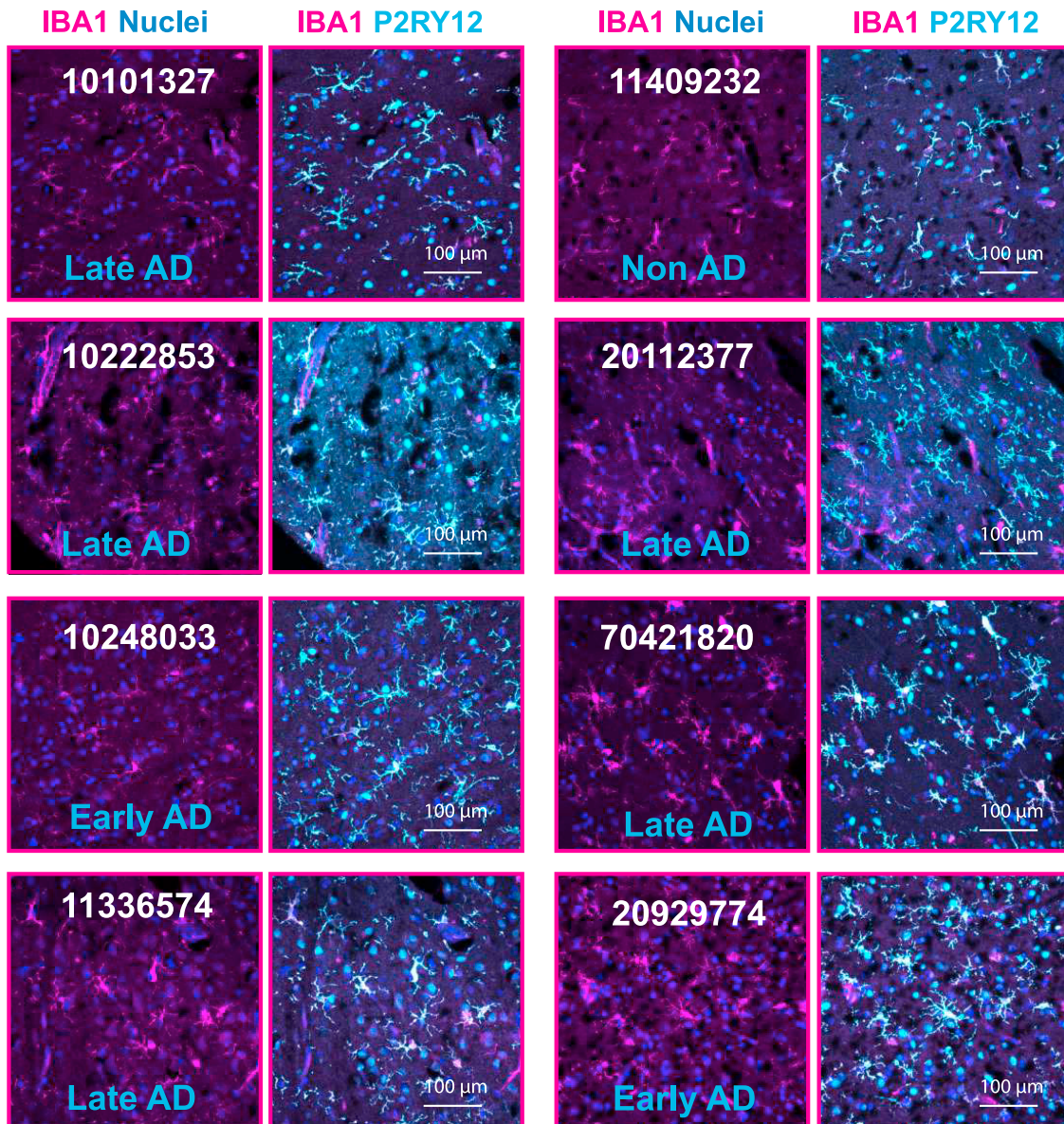


**Figure S3.** Immunohistochemistry on a subset of postmortem human brain samples from ROSMAP cohort, related to [Figures 1, 2, and 4](#). Immunostaining for IBA1 and P2RY12 across 8 subjects spanning non-AD to early AD and late AD status. ROSMAP subject IDs are displayed in each corresponding image.

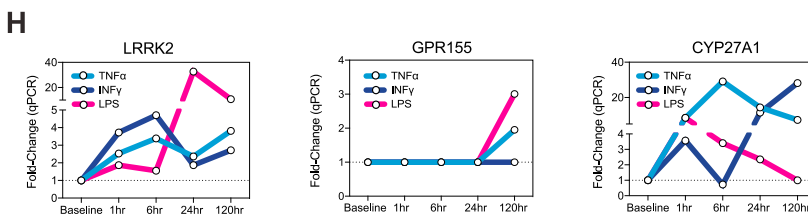
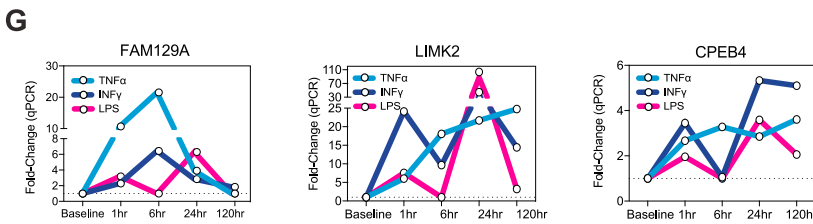
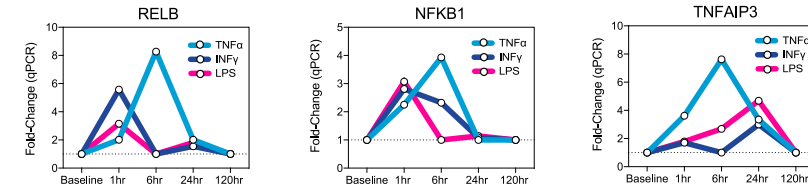
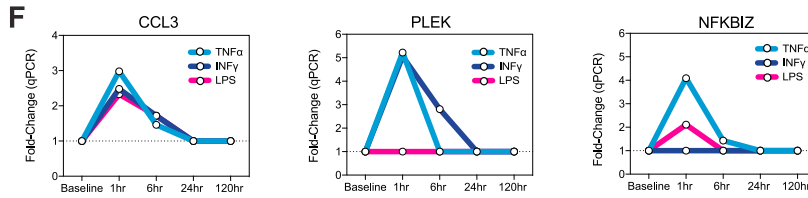
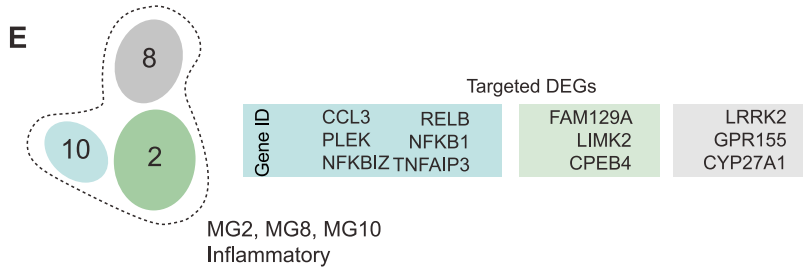
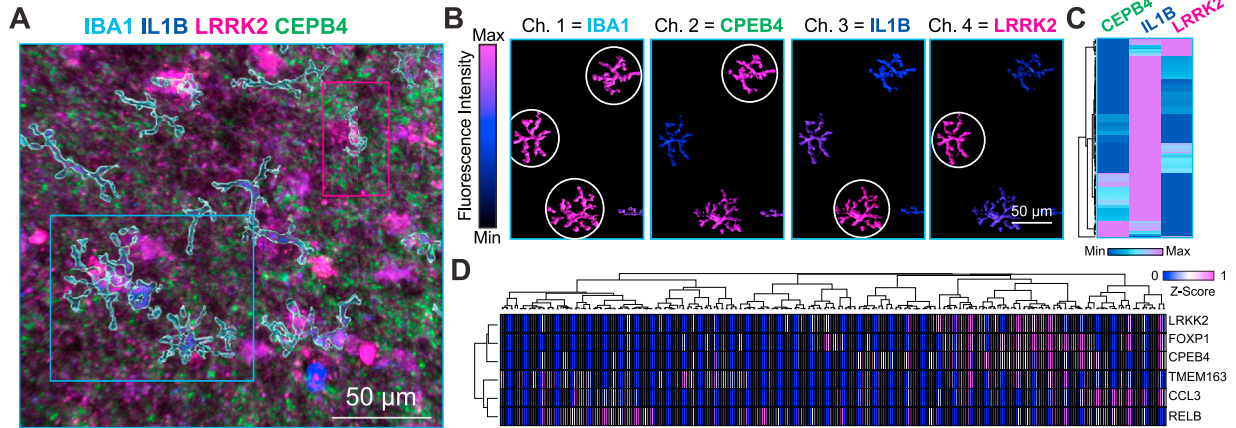


**Figure S4. Validation of marker genes associated with inflammatory states and transcriptional response across MG10, MG8, and MG2 markers in iMGLs exposed to pro-inflammatory stimulus, related to Figure 2**

(A) Multiplexed immunostaining to spatially resolve inflammatory states across the human brain. IBA1 was used to label all CNS resident macrophages, ILB1 to label MG10, LRRK2 to label MG8, and CPEB4 to label MG2 microglia (see list of antibodies used in immunohistochemistry in Table S1, page 4). ROSMAP subject ID, 10248033.

(B) Fluorescent intensity projection onto 3D renderings of IBA1 signal for each channel of multiplex immunostaining shows distinct microglial populations.

(C) Heatmap for immunostaining quantification showing relative maximum intensity fluorescence for CPEB4, IL1B, and LRRK2.

(D) Quantification of microglia (P2RY12<sup>+</sup>IBA<sup>+</sup>CX3CR1<sup>+</sup>) from RNAscope HiPlex for inflammatory state markers: LRRK2, FOXP1 (MG8 marker), CPEB4, TMEM163 (MG2 marker), CCL3, and RELB (MG10 marker). Number of dots normalized across cells for each marker and plotted as Z scores and shown from blue (low) to magenta (high). n = 291 microglia from 4 AD subjects were quantified.

(E–H) qPCR analysis for pulse-and-chase experiment after iMGLs exposure to pro-inflammatory stimuli (TNF $\alpha$ , INF $\gamma$ , and LPS).

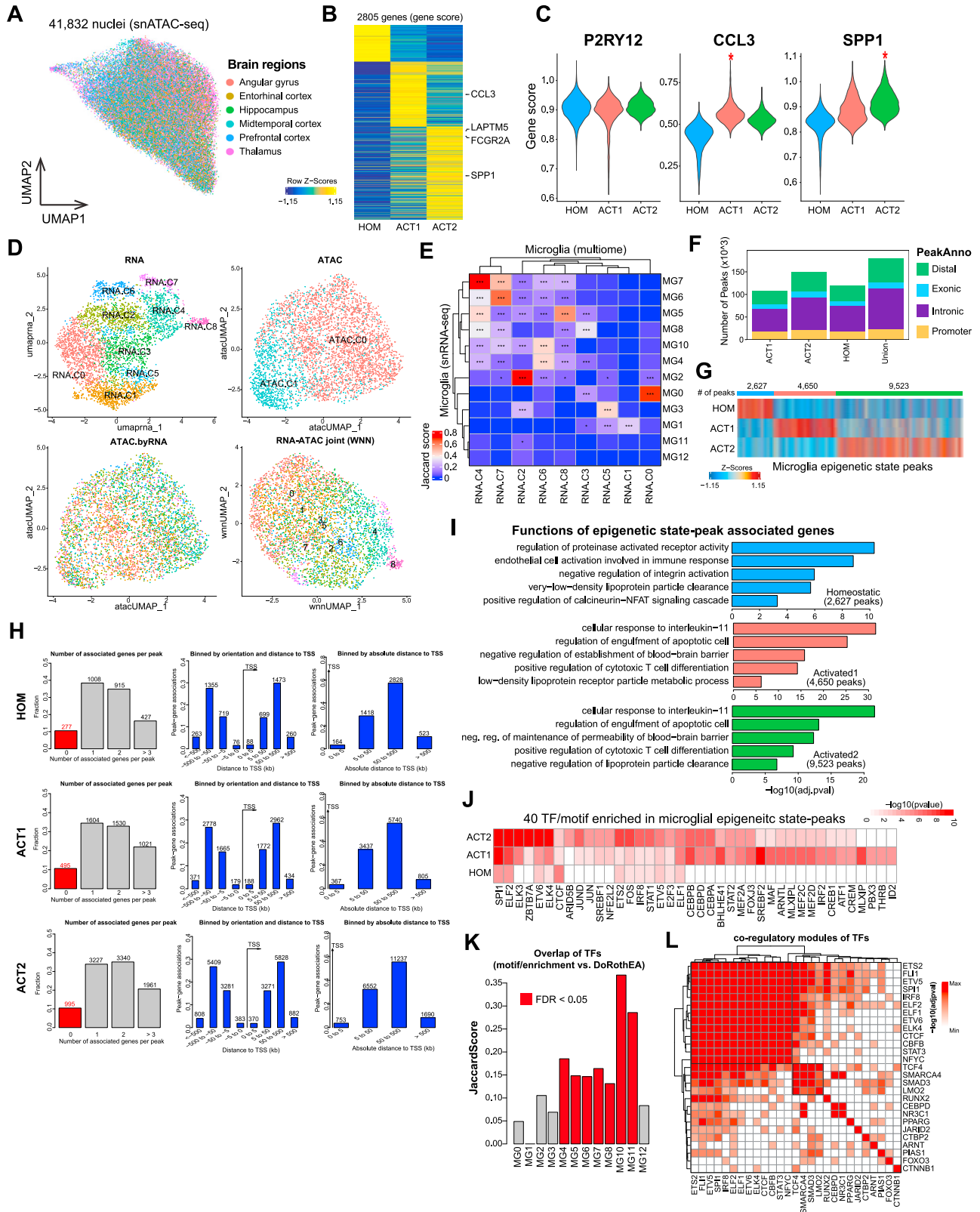
(E) List of marker genes and their corresponding MG cluster origin.

(F) MG cluster 10 genes.

(G) MG cluster 2 genes.

(H) MG cluster 8 genes.

Note that while IL1B is not shown in this supplemental figure, CPEB4 and LRRK2 are duplicated here from Figure 2G n = mean of biological triplicate are shown for each timepoint and treatment. Error bars were removed for ease of interpretation.



(legend on next page)

---

**Figure S5. Microglial epigenetic states defined by snATAC-seq data, related to Figure 3**

- (A) UMAP of 41,832 microglia nuclei in snATAC-seq labeled by the six brain regions.
- (B) Heatmap to show the gene score patterns of 2,805 marker genes across three epigenomic states in microglia. The known marker genes for microglia are listed on the right. The Z scores are shown in the heatmap.
- (C) Gene score distributions of P2RY12, CCL3, and SPP1 in three microglial epigenomic states. CCL3 shows the significantly high score in ACT1 state and SPP1 shows the significantly high score in ACT2 state, highlighted with star labels. The p value < 0.01 as cutoff in the Wilcoxon rank test.
- (D) UMAPs to show the microglia clusters for RNA, ATAC, ATAC colored by RNA, and RNA-ATAC joint analysis in multiome data from 19 ROSMAP individuals.
- (E) Heatmap to show the significant enrichment of marker genes of multiomic transcriptional clusters of microglia in 12 microglial states. Jaccard score represents the percentage of pairwise overlapping genes. Fisher's exact test was used to evaluate the significance of overlapping (adjusted p value < 0.05 as a cutoff).
- (F) The annotation of accessible peaks in microglia. Colors represent the distinct genomic locations including distal, exonic, intronic, and promoter.
- (G) Heatmap to show 16,800 marker peaks in three epigenomic states. Z score values across microglia states are shown in the heatmap.
- (H) GREAT analysis to annotate the epigenomic-specific peaks. The panels from left to right include the distribution of peaks based on the number of associated genes per peak, the distribution of peaks based on the distance to TSS, and the distribution of peaks based on the absolute distance to TSS.
- (I) Representative enriched Gene Ontology biological processes of epigenomic state-peak-associated genes. GREAT was used to perform the annotation and GO enrichment (adjusted p value < 0.05 as cutoff).
- (J) Heatmap to show the TF/motif enrichment of peaks in each epigenomic state. The  $-\log_{10}$  of p value represents the enrichment. Homer was used for motif analysis with the peaks (expanded to 2 kb) as input. Only the TFs with expression in microglia (average expression > 1 after log transformation) are shown.
- (K) Bar plot to show the percentage of overlapping TFs identified using motif-/enrichment-based methods and using DoRothEA, a TF-activity-based method at single-cell level. The red bars show the significance (FDR < 0.05).
- (L) The co-regulatory modules of 27 TFs in MG0. Fisher's exact test is used to evaluate the significance of overlap of targets between each pair of TFs. Adjusted p value < 0.05 is used as a cutoff and 89 MG0 marker genes as background. The  $-\log_{10}$  of p value is shown in heatmap.

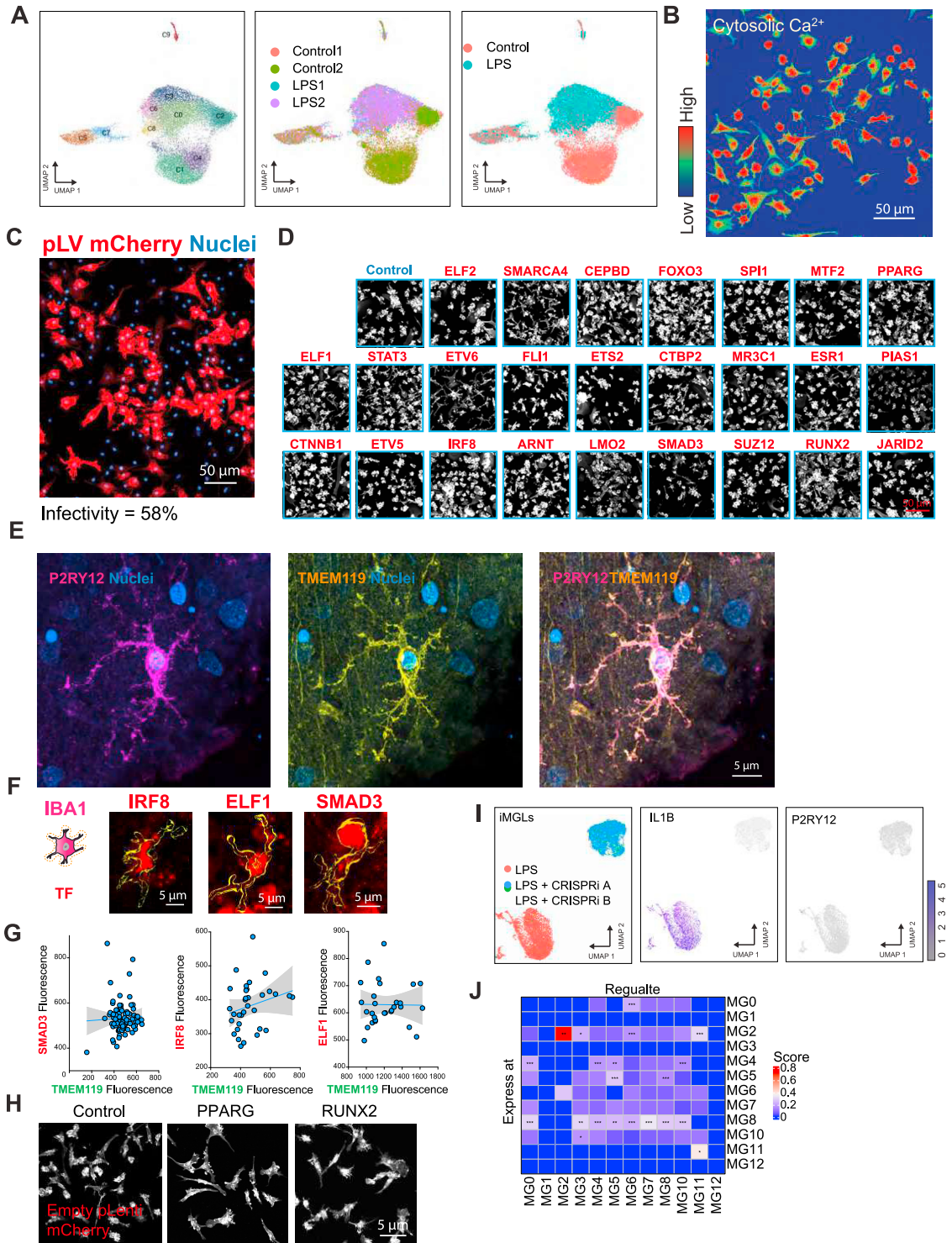


**Figure S6. Modulating microglial states in iMGLs by forced expression of master TFs, related to Figure 4**

- (A) UMAP for iMGL single-nuclei sequencing showing all identified clusters (C1–C9).  
 (B) Maximum projection of a live imaging time series in iMGLs labeled with the calcium reporter dye Fluo-4 AM.  
 (C) iMGLs 8 days post-infection with lentiviral vector carrying the red fluorescent protein mCherry.  
 (D) Actin staining is shown for a random field of view for each of the TF overexpression conditions to highlight morphological changes.  
 (E) Immunostaining of human brain tissue showing colocalization of P2RY12 in magenta with TMEM119 in yellow. ROSMAP subject ID, 11409232.  
 (F) Immunostaining for homeostatic TFs in IBA1 positive cells across the human brain.

(legend continued on next page)

---

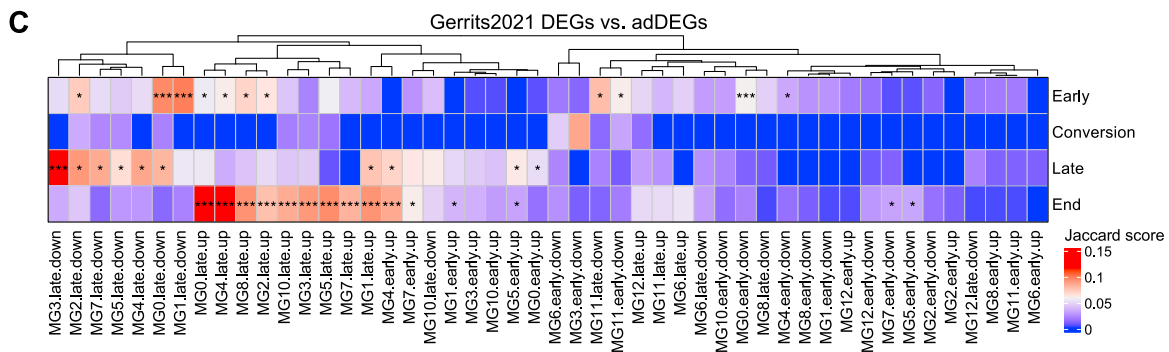
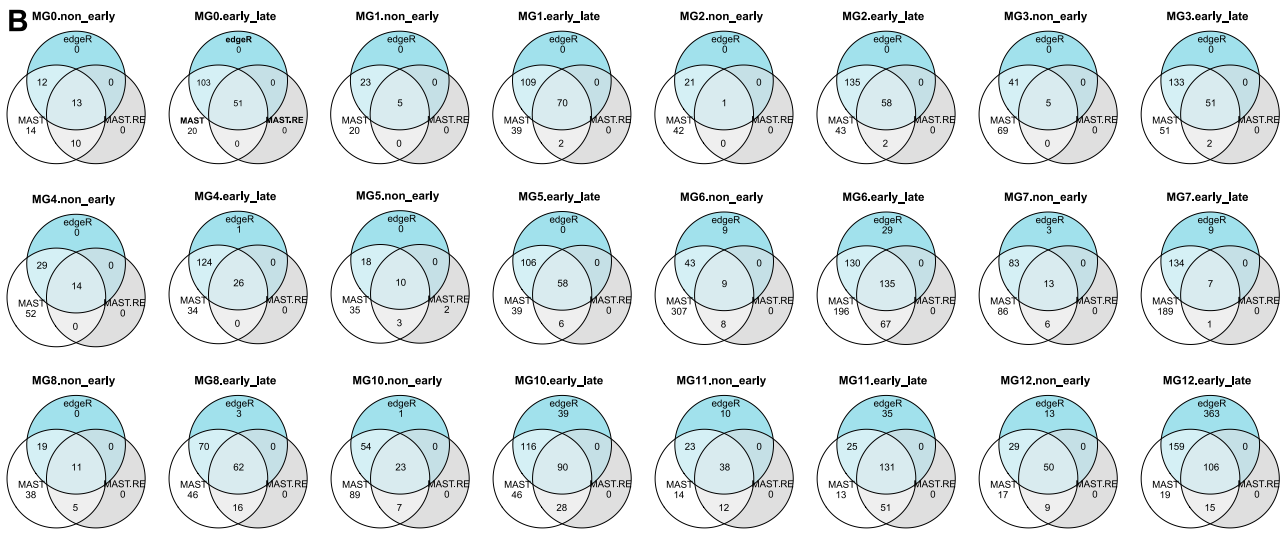
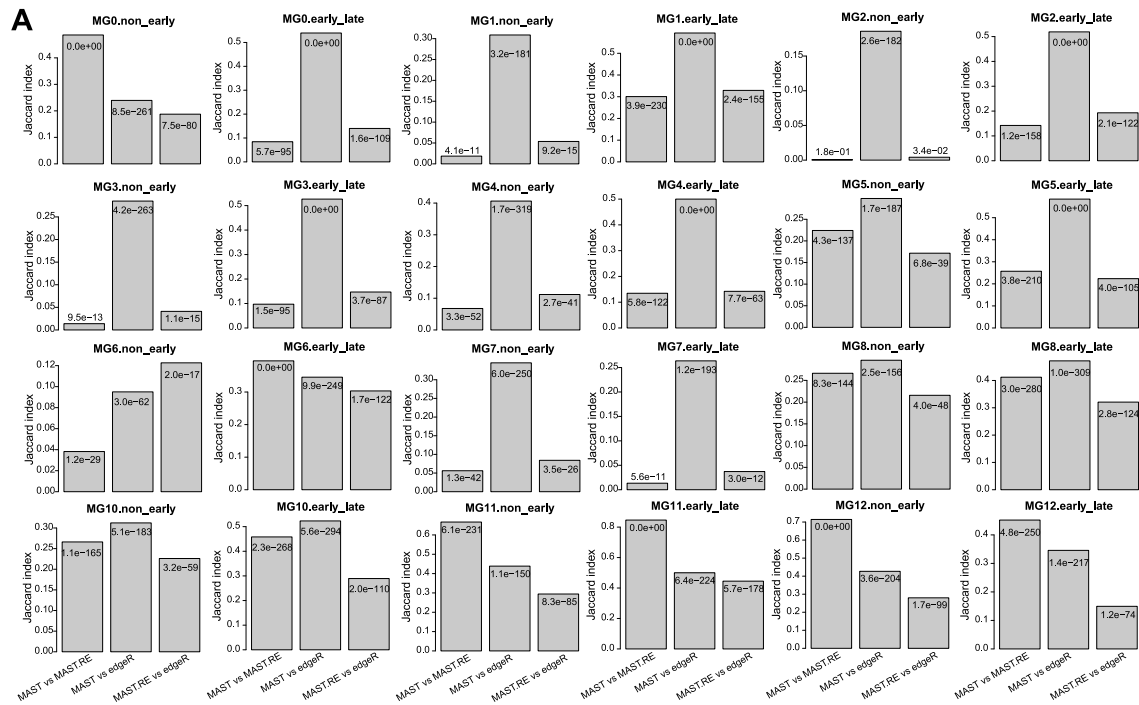
(G) Correlation analysis for SMAD3, IRF8, and ELF1 with TMEM119. No significant effect was detected.

(H) Actin staining is shown for iMGLs infected with an empty mCherry control lentivirus, and TF overexpression of PPARG and RUNX2. Note that images of PPARG and RUNX2 are duplicated here from those shown in main [Figure 4G](#) to ease comparison with control.

(I) UMAPs for snRNA-seq experiment with CRISPRi iMGLs. Repression of FOXO3, HIF1A, and FOXP2 in LPS-treated iMGLs can block the induction of IL1B but no gain in homeostatic marker P2RY12.

(J) The score shown in the heatmap represents the enrichment of upstream regulators' expression in each microglial state. The significance (star in the heatmap) is evaluated by the p value of a permutation test (permutation times: 1,000). See details in [STAR Methods](#).





(legend on next page)

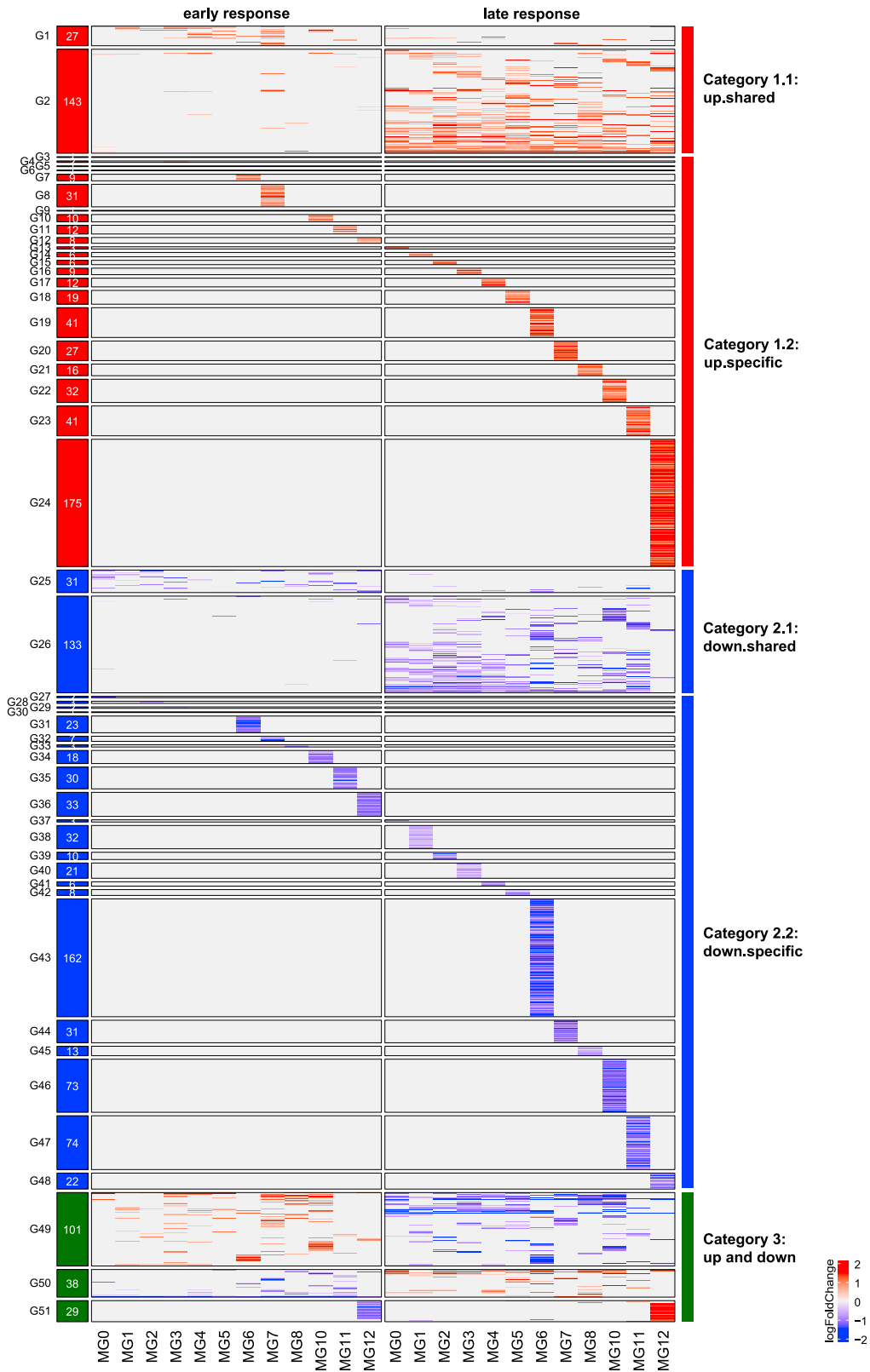
---

**Figure S7. Comparisons of DEGs between methods and datasets, related to Figure 5**

(A) The pairwise comparison of DEGs between MAST, MAST with random effect (MAST.RE), and edgeR. The bar plot shows the Jaccard index to represent the percentage of overlapping genes. The values inside of the bar are FDR after log<sub>10</sub> transformation to represent the significance of overlapping. Each panel represents each comparison (non-AD vs. early AD, or early AD vs. late AD, per state).

(B) Venn diagram to show the number of genes shared or specific in each method.

(C) Heatmap to show the significant enrichment of DEGs identified in this study with DEGs identified in Gerrits et al. Jaccard score represents the percentage of pairwise overlapping genes. Fisher's exact test is used to evaluate the significance of overlapping (adjusted p value < 0.05 as a cutoff).

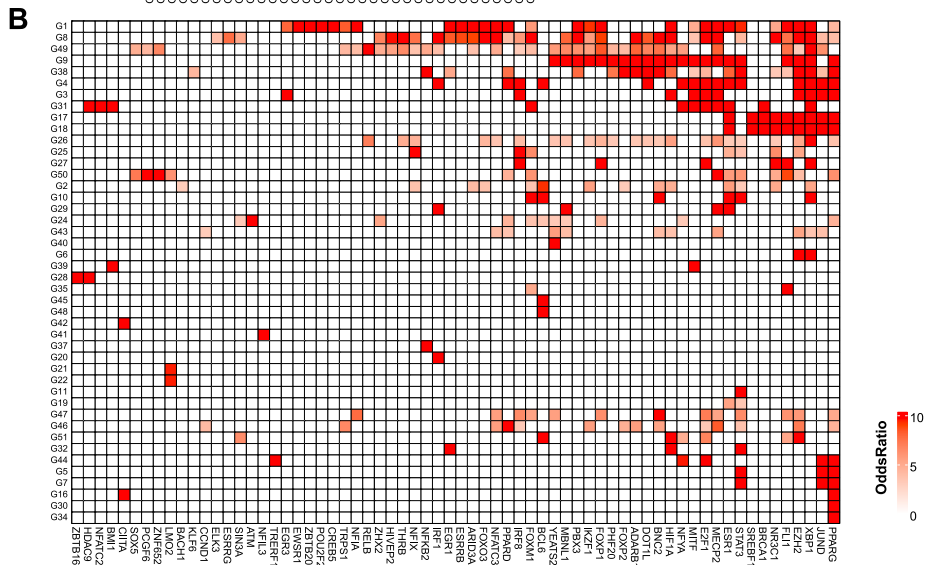
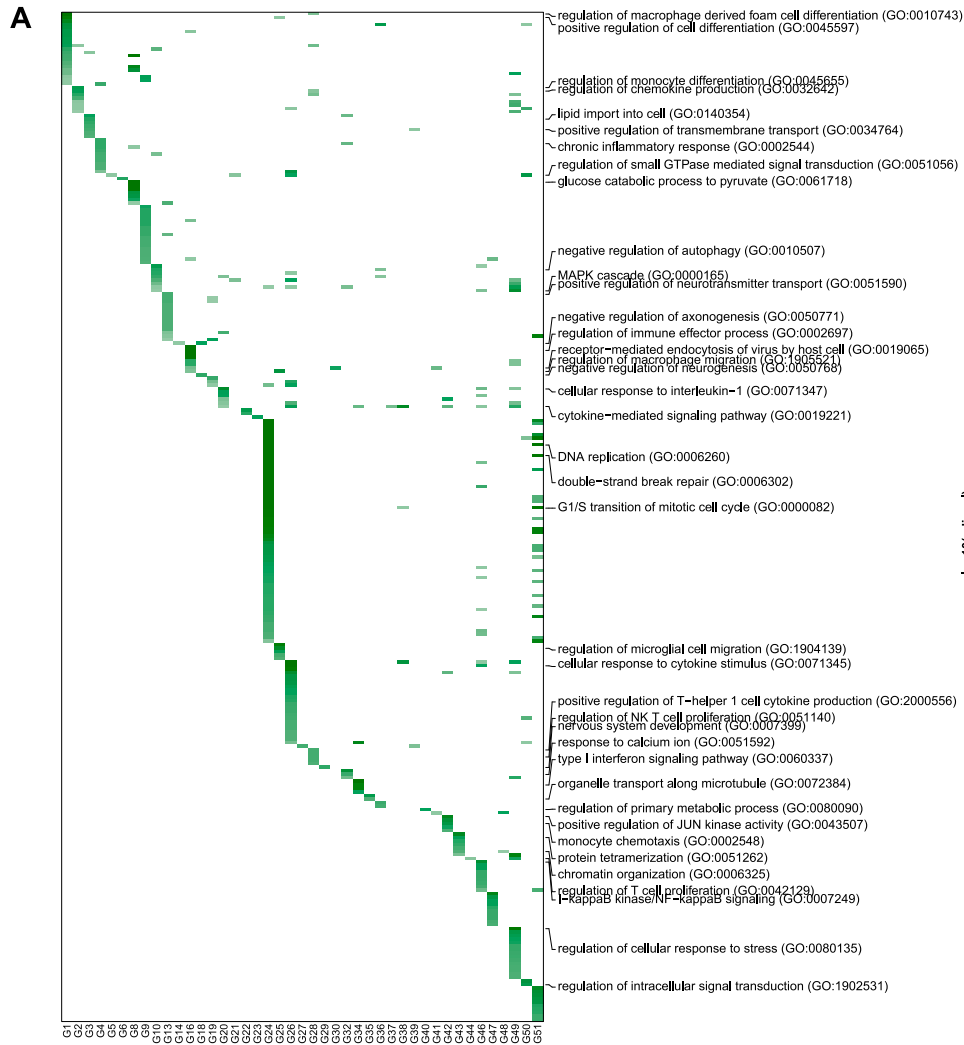


(legend on next page)

---

**Figure S8. Transcriptional changes of microglial transcriptional states in AD, related to Figure 5**

Transcriptional changes of 1,542 DEGs in three major categories with 51 gene groups in AD progression. Heatmap shows the change directions. Red represents up regulated in AD progression, i.e., up regulated in low AD pathology when compared with no AD pathology and up regulated in high AD pathology when compared with low AD pathology, and blue represents down regulation in AD progression. The numbers in the block on the left of heatmap show the number of DEGs included in each gene group.



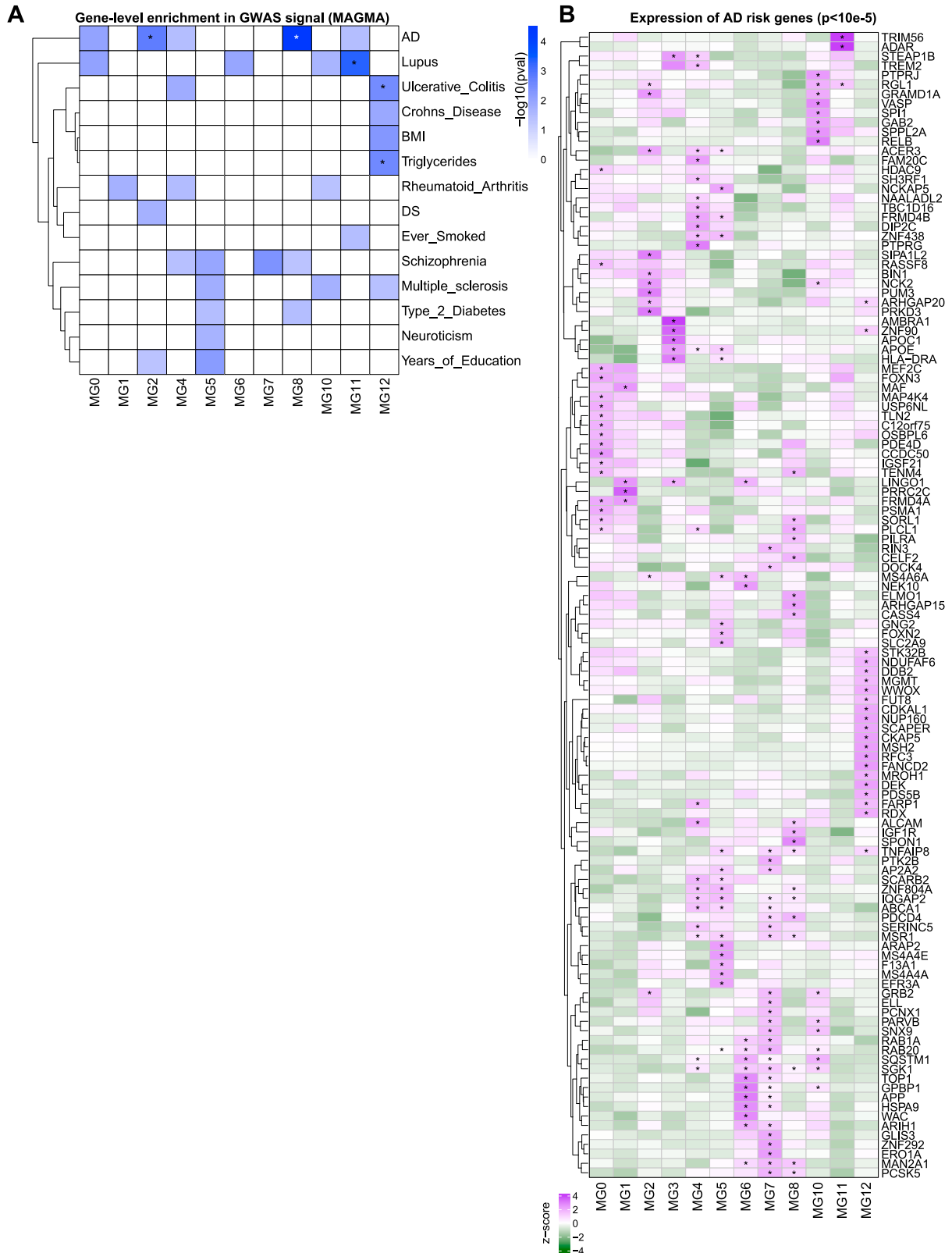
(legend on next page)

---

**Figure S9. Biological processes and TF enrichment in DEGs during AD progression, related to Figure 5**

(A) Heatmap to show the enriched Gene Ontology biological processes in DEGs of 51 gene groups shown in Figure S8. Enrichr in R was used to perform GO enrichment (adjusted p value < 0.05 as cutoff).

(B) Heatmap to show the TF enrichment of DEGs in each group shown in Figure S8. Odds ratio represents the enrichment. Enrichr package in R based on three libraries including TRANSFAC and JASPAR, ChEA, and ENCODE TF chromatin immunoprecipitation sequencing (ChIP-seq) data was used to predict upstream TFs (adjusted p value < 0.05 as a cutoff). Only the TFs with expression in microglia (average expression > 1 after log transformation) are shown.



(legend on next page)

---

**Figure S10. Expression patterns of AD-risk genes in 12 microglial transcriptional states, related to Figure 6**

(A) Heatmap to show gene-level enrichment in GWAS signals to associate microglial states with multiple traits. MAGMA is used to evaluate the significance of enrichment. The  $-\log_{10}$  of p value is shown in the heatmap. The blue blocks show the p value  $< 0.05$  as a cutoff. The stars show FDR  $< 0.05$  as a cutoff.

(B) AD-risk genes were obtained from GWAS catalog (GWAS variant p value  $< 10e-5$ ). The stars highlight the genes with especially high expression in the corresponding state.